UNIVERSITY OF CALIFORNIA

Santa Barbara

Methods for improved mapping of brain lesion connectivity

A dissertation submitted in partial satisfaction of the

requirements for the degree Doctor of Philosophy

in Electrical and Computer Engineering

by

Clint Greene

Committee in charge:

Professor Ken Rose, Chair

Professor Scott T. Grafton

Professor B.S. Manjunath

Professor Michael Liebling

December 2019

The dissertation of Clint Greene is approved.

_____

Scott T. Grafton

_____

Michael Liebling

_____

B.S. Manjunath

_____

Ken Rose, Committee Chair

August 2019

Methods for improved mapping of brain lesion connectivity

by

Clint Greene

ACKNOWLEDGEMENTS

I am deeply indebted to my research advisor Professor Scott Grafton for his constant guidance, financial support, and encouragement throughout my graduate research and studies. I would like to especially thank him for giving me the opportunity to work in the Brain Imaging Center and collaborate with his students. Working and interacting with him over the years has been a truly rewarding experience.

My sincere thanks to my committee chair Professor Ken Rose for also giving me the opportunity to study and work in the Signal Compression Lab. I have always been inspired by your sharp insights into problems spanning multiple disciplines as well as your ability to help me formulate my ideas so that can be solved using methods in Electrical Engineering.

When I first started this journey, I knew little about Electrical Engineering. There are numerous people that helped me transform along the way from a neuroscientist into an electrical engineer. I would like to thank Professor B.S. Manjunath for making this opportunity possible and for serving on my committee. I would also like to give thanks to Professor Michael Liebling for serving on my committee.

During my graduate studies, I have benefited immensely from collaborative research projects with Matt Cieslak as well as engaging technical discussions with Weiting Lin and Ahmed Elshafiy.

Finally, sincere thanks to all of my friends and family for their constant encouragement and support throughout my graduate studies.

VITA

EDUCATION

Bachelor of Science in Neurobiology University of Texas, Austin, May 2009 (summa cum laude)
Master of Science in Electrical and Computer Engineering, University of California, Santa Barbara, June 2016
Doctor of Philosophy in Electrical and Computer Engineering, University of California, Santa Barbara, August 2019

PROFESSIONAL EMPLOYMENT

Summer 2016: Research Intern, IBM Almaden
2013—2019: Graduate Student Researcher, Department of Electrical and Computer Engineering & Psychology, University of California, Santa Barbara

PUBLICATIONS

1. Greene, C., Rose, K., & Grafton, S. T. (2019). Optimal Fiber Diffusion Model Restoration. In Preparation.
2. Greene, C., Cieslak, M., Volz, L. J., Hensel, L., Grefkes, C., Rose, K., & Grafton, S. T. (2019). Finding maximally disconnected subnetworks with shortest path tractography. NeuroImage: Clinical, 101903.
3. Greene, C., Cieslak, M., & Grafton, S. T. (2018). Effect of different spatial normalization approaches on tractography and structural brain networks. Network Neuroscience, 2(3), 362-380.
4. Cieslak, M., Brennan, T., Meiring, W., Volz, L. J., Greene, C., Asturias, A., ... & Grafton, S. T. (2018). Analytic tractography: A closed-form solution for estimating local white matter connectivity with diffusion MRI. NeuroImage, 169, 473-484.
5. Cieslak, M., Meiring, W., Brennan, T., Greene, C., Volz, L. J., Vettel, J. M., ... & Grafton, S. T. (2018, April). Compositional measures of diffusion anisotropy and asymmetry. In 2018 IEEE 15th International Symposium on Biomedical Imaging (ISBI 2018) (pp. 123-126). IEEE.
6. Wei, K., Cieslak, M., Greene, C., Grafton, S. T., & Carlson, J. M. (2017). Sensitivity analysis of human brain structural network construction. Network Neuroscience, 1(4), 446-467.

AWARDS

Graduate Opportunity Fellowship (University of California, 2018—2019)
Doctoral Scholar Fellowship (University of California, 2013—2017)
Graduate Scholar Award (Jack Kent Cooke Foundation, 2013—2017)

FIELDS OF STUDY

Major Field: Medical Imaging and Neuroscience

Studies in Optimal Estimation and Computer Vision with Professor Rose

Studies in Neuroscience and Network Science with Professor Grafton

Abstract

Methods for improved mapping of brain lesion connectivity

by

Clint Greene

Recent advances over the past two decades in neuroimaging methods have enabled us to map the connectivity of the brain. In parallel, pathophysiological models of brain disease have shifted from an emphasis on understanding pathology in specific brain regions to characterizing disruptions to interconnected neural networks. Nevertheless, these recent methods for mapping brain connectivity are still under development. Every step of the mapping process becomes a potential source for additional error due to noise or artifacts that could impact final analyses. Segmentation, parcellation, registration, and tractography are some of the steps where this occurs. Moreover, mapping the connectivity in a brain lesion is even more susceptible to errors in these steps.

In this body of work, I describe multiple new methods for improving the accuracy of mapping lesion connectivity by reducing errors at the tractography stage which is the most error prone stage. First, we develop an approach for directly normalizing streamlines into a template space that avoids performing tractography in the normalized template space, reducing the error of connectomes constructed in the template space with respect to the ground truth native space connectome. Second, we develop a rapid approach for performing

shortest path tractography and constructing shortest path probability weighted connectomes which increases the connection specificity relative to local streamline tracking approaches. We then demonstrate how our shortest path tractography approach can be used construct a disconnectome, a connectivity map of the proportion of connections lost due to intersecting a lesion. We then develop a fast, greedy graph-theoretic algorithm that extracts the maximally disconnected subgraph containing brain regions with the greatest shared loss of connectivity. Finally, we demonstrate how combining methods from diffusion based image inpainting and optimal estimation can be used to restore or inpaint corrupted fiber diffusion models in lesioned white matter tissue, enabling tractography and the study of lesion connectivity and modeling of microstructural measures in the patient's native space.

Table of Contents

List of Acronyms

AD	axial diffusivity
CLSM	connectome-based lesion symptom mapping
CST	corticospinal tract
CSD	constrained spherical deconvolution
CT	computed tomography
dMRI	diffusion magnetic resonance imaging
DSI	diffusion spectrum imaging
DSN	direct streamline normalization
DT	diffusion tensor
DTI	diffusion tensor imaging
DW-MRI	diffusion-weighted magnetic resonance imaging
DWI	diffusion weighted image
FA	fractional anisotropy
fMRI	functional magnetic resonance imaging
FODR	fiber orientation distribution reorientation
FODs	fiber orientation distributions
GQI	generalized q-sampling imaging
GFA	generalized fractional anisotropy
HARDI	high angular resolution diffusion imaging
HCP	human connectome project
MD	mean diffusivity

MS	multiple sclerosis
MSE	mean squared error
MMSE	minimum mean squared error
MRI	magnetic resonance imaging
ODFs	orientation distribution functions
PEV	primary eigenvector
PSFs	point spread functions
QA	quantitative anisotropy
QSDR	q-space diffeomorphic reconstruction
RD	radial diffusivity
SyGN	symmetric group wise normalization
VLSM	voxel-based lesion symptom mapping

List of Figures

List of Tables

Chapter 1

Connectomics

The brain is composed of two main tissue types: gray matter and white matter. Gray matter is the collection of neuronal cell bodies that integrate signals at their synapses. White matter is composed of myelinated axons that connect various regions of gray matter, allowing distant brain regions to send signals to each other. The formation of these axons is guided during development by genetic and environmental factors (Dubois et al., 2014). Collections of axons form white matter pathways. Depending on what cortical regions a white matter pathway connects can determine both the function of the pathway and the regions it connects (Passingham et al., 2002). The term connectome was proposed over a decade ago (Sporns et al., 2005). The connectome model of the brain is a network representation, where nodes represent brain regions and edges represent white matter pathways. Mapping the human connectome has become a major goal in neuroscience because of its potential to reveal new insights into how cortical regions are arranged and influence each other and how these processes are disrupted under pathological conditions (Fornito & Bullmore, 2015).

Connectomes can be constructed at different levels of scale. At the micro and meso scales invasive techniques such as histological staining, serial electron microscopy, 3D fluorescence imaging, and chemical tracing are used for mapping the connectome

(Sotiropoulos & Zalesky, 2019). At the macro scale, non-invasive imaging techniques such as functional MRI (fMRI) and diffusion MRI (dMRI) are used to construct the connectome. Compared to invasive approaches, non-invasive approaches do not explicitly trace out connections. Instead they rely on models and inference to estimate connectivity. Consequently, non-invasive approaches are error prone and the results can be difficult to quantify. Moreover, non-invasively constructed connectomes are at a much lower spatial resolution and cannot estimate the directionality of the connection compared to invasive ones. Despite these shortcomings, non-invasive connectomes offer multiple advantages: they can be studied in-vivo across many populations, can be mapped along with function, behavior and genetics, and how connections change with development, aging, and pathology (Behrens & Sporns, 2012). Inferring a macro connectome from fMRI or dMRI data is a challenging task and an active field of research. Constructing such a connectome can be divided into two tasks: node delineation, and edge mapping.

1.1 Node delineation

Node delineation is a deceptively challenging task because there are no overt boundaries visible with MRI that allow precise delineation of functionally meaningful node borders. The most commonly used approach is to take an architectonic atlas such as the Talairach or an anatomical atlas such as the AAL or Lausanne that's defined in a template space and map it to an individual's brain. The Talaraich nodes are delineated by architectonic features from post-mortem brains (Lancaster et al., 2000). The Laussane nodes are delineated based upon anatomical landmarks (Daducci et al., 2012). Typically, an individual's T1 weighted (T1w) volume is non-linearly registered to a template T1w volume where the atlas is defined.

Analyses can be performed in the template space or in the subject's brain space by inverting the transformation. This ensures that nodes between subjects are matched with respect to average size, geometry, and location. Subject specific parcellations can also be generated from task-based or resting-state fMRI data to delineate regions based on functional properties (Yeo et al., 2011). Currently, there is not a gold standard atlas and each approach has strengths and weaknesses. Researchers tend to use a parcellation atlas that fits their need and problem at hand. In this body of work, we choose the Lausanne atlas because of the interpretability it confers between anatomy and function.

1.2 Edge mapping

Connectivity can be measured between the nodes once they have been delineated. Within MRI, there are two broad classes of brain connectivity: functional and structural. For each class, connectivity is always measured pairwise between two regions and the full connectome is constructed by measuring the pairwise connectivity for every region pair to every other region pair. We will briefly cover functional connectivity for completeness and then focus on structural connectivity because it's the measure of connectivity used throughout this body of work.

1.2.1 Functional connectivity

Functional connectivity refers to the statistical dependence between blood oxygenation level dependent (BOLD) signals measured between a pair of nodes. Typically, it's quantified by the taking the average of the BOLD time series in each voxel making up a

region and then simply taking the pair-wise Pearson correlation between the signals. Other measures such as mutual information and coherence have also been used (Smith et al., 2011). The more strongly connected two regions are the more their BOLD signals fluctuate together. Functional connectomes are dynamic, capturing the spontaneous fluctuations between brain regions. Over long time scales (minutes) functional connectomes have showed strong resemblance to structural connectomes (Honey et. al, 2007). Moreover, other researchers have shown that the functional connectome can be predicted from the structural connectome (Honey et al., 2009).

1.2.2 Structural connectivity

Structural connectivity estimates the amount of physical wiring between brain regions. It is mapped using dMRI based tractography that infers the location of white matter bundles using streamlines. White matter fiber bundles are coherently organized such that diffusion of water molecules occurs preferentially along the long axis of the bundles i.e. parallel to the them. The preferred diffusion orientations (PDO) can be indirectly mapped to fiber orientations at the voxel level using multiple reconstruction methods. Tractography methods then integrate the orientation information to infer the putative white matter bundles. Typically, the connectivity is quantified by counting the number of streamlines that exist between a pair of regions.

A. Reconstruction methods

Fiber orientations are typically mapped using a couple of different approaches depending on how the diffusion weighted images (DWIs) were collected. The oldest, simplest, and most common approach for mapping fiber orientations is the diffusion tensor model which only provides an estimate of a single orientation from the diffusion tensor (Alexander et al., 2007). Because voxels can contain multiple fiber populations at different orientations, more complex models such as spherical deconvolution are used to reconstruct the fiber orientation distribution (FOD) that characterizes the multiple fiber orientations (Tournier et al., 2007). However, diffusion tensor based reconstructions remain the dominant method in clinical research. In Chapter 4, we discuss both of these models in greater detail.

B. Tractography

Tractography methods can be grouped into two categories: local and global approaches. Local streamline methods propagate streamlines that are tangent to vector orientation fields extracted from the FODs. They are subdivided into two categories depending on whether they perform a deterministic or probabilistic estimation of the direction to propagate the growing streamline. In deterministic tractography, streamlines are propagated according to a fixed direction in each voxel (Yeh, 2013). Typically, this direction is the direction of the peak of the FOD. Criticisms leveled against deterministic approaches is their inability to account for uncertainty in the estimated path, sensitivity to the estimated peak direction, and susceptibility to noise (Jones, 2010). Slight perturbations in peak estimation due to noise can accumulate into large errors as the streamline grows. In contrast, probabilistic tractography estimates a distribution of fiber orientations at each voxel from the FOD. A random sample

is drawn from the distribution to determine the direction to propagate the streamline (Descoteaux et al., 2008). Consequently, probabilistic tractography yields greater spatial dispersion in streamline trajectories compared to deterministic tractography which leads to more spurious connections. Thresholding can prune out spurious connections increasing specificity at the cost to sensitivity (Thomas et al., 2015). Moreover, probabilistic methods are also more computationally intensive. Estimates derived from probabilistic tractography show greater connectome reproducibility, while connectomes constructed from deterministic methods have lower connection density with increased accuracy (Buchanan et al., 2014). In a recent study that compared a plethora of tractography algorithms, deterministic methods were found to sometimes outperform probabilistic methods (Maier-Hein et al., 2017). However, both of these local approaches suffer from significant biases that lead to poor sensitivity in estimating known anatomical connections between regions in a connectome. The most prominent bias seen in local tracking methods is a distance bias where streamline counts between distant regions are either smaller or non-existent compared to counts between nearby neighboring regions (Schober, 2014). The distance bias is driven by the greedy nature of growing a streamline unsupervised without a particular target. The more the streamline grows, the more likely it enters a region that triggers the stopping criterion of the algorithm. Consequently, voxels near the seeding region where streamlines start growing are explored more thoroughly than voxels far away which leads many distant region pairs that should be connected to become disconnected in the connectome.

Global approaches estimate streamlines according to some optimal global criterion and are less susceptible to distance biases and local termination errors (Girard, 2014). Shortest path tractography is a global approach that is able to overcome distance biases because the

globally optimal path can be found irrespective of distance when the start and end points are specified. However, this property of shortest paths introduces a new problem where a connection will always be found, even if it doesn't truly exist. This can be circumvented by filtering out low weight connections using methods such as LiFE and COMMIT while still maintaining a high degree of specificity and sensitivity relative to local tracking approaches (Pestilli et al., 2014 & Daducci et al., 2014). Although shortest path tractography approaches are a promising alternative, they have not been widely used because they are computationally demanding. In Chapter 3, we describe a new approach to using shortest path tractography for constructing connectomes that is two orders of magnitude faster than previous approaches.

1.3 Lesion symptom mapping

Clinical neurology began from the analysis of intriguing single cases where associations between neurological symptoms and deficits and the location and extent of a lesion were determined typically post mortem. These early lesion symptom analyses provided important insights into the functional organization of the human brain. Significant historical examples include H.M. whose hippocampal lesions gave us insight into this region's essential role in memory and Phineas Gage whose frontal lobe damage gave us insight into the role the frontal lobe plays in regulating social behaviors (Scoville & Milner, 1957; Damasio et al., 1994). However, these early lesion studies were more correlative than causal.

.

1.3.1 Overlap mapping

Destructive tissue lesions from traumatic brain injuries, tumors, multiple sclerosis, or strokes can be imaged using various MRI contrasts because they affect the T1 and T2 weighted contrasts. With the ability to easily image lesions, the field shifted from single case studies to group studies because patients could now be grouped based on similarities in deficits and lesion overlap. When lesions that cause the same symptoms and overlap in the same brain region in many different patients, the causal link between those symptoms and the region are strengthened (Fox, 2018). However, over time it became apparent that lesion overlap methods were sometimes flawed because similar symptoms can result from lesions in different locations. For example, most lesions that disrupt memory are located outside of the hippocampus (Lim, 2009). Furthermore, lesions that cause disruption to a cognitivie function might occur in a location that is not known for that function. The relationship between symptoms and lesion location is not straightforward because it is rare that a brain injury results in a single cognitive deficit because many cognitive functions are not localized into a discrete area and instead arise from emergent activity across distributed neural networks via interconnected cortical regions (Geschwind, 1962 & Baldassarre et al., 2016). A given cognitive deficit could result from disruption to a functional network rather than from injury to a single area. If a complex behavior requires integration from multiple brain areas in a network, a lesion to any of the areas could result in a deficit in that behavior. Consequently, a lesion overlap analysis could miss that the deficits are due to network disruption and instead find that the deficits are due to lesions in multiple single brain areas.

These limitations of single lesion analysis has led to the rise in use of network based approaches for improved understanding of the relationship between brain injury and symptoms.

1.3.2 Connectome Lesion Symptom Mapping

The merging of connectomics with single lesion symptom mapping has given rise to a new field called connectome lesion symptom mapping (CLSM). CLSM can determine whether lesions that are in different areas but cause the same symptoms are part of the same functional network. Traditional lesion analysis would find that the same symptom is caused by lesions in different areas, missing that these areas make up nodes in an interconnected network. One of the most quintessential examples that illustrates the use of the connectome in lesion analysis is the problem of paralysis (Fox, 2018). Lesions in the brainstem, thalamus, pons, or motor cortex can all lead to paralysis. These lesions fail to overlap in a single area but make up the motor network. They are all connected to the corticospinal tract (CST) which is the motor tract running from the cerebral cortex to the spinal cord, controlling the movements of our limbs and trunk. Paralysis can also result from damage to the CST even if the motor areas themselves are not damaged due to the cortical areas becoming disconnected. Moreover, lesions that cause the largest number of symptoms occur at the intersection of large white matter pathways and at cortical hubs that are connected to large numbers of brain regions (Warren et al., 2014).

In the example of paralysis, the nodes and edges making up the motor network are well known. However, in most cases it is unknown what set of disrupted nodes and edges in a cortical network leads to some set of neurological symptoms. To map a patient's

neurological symptoms to a brain network, the lesion area must first be segmented from the clinical brain volume (MRI or CT). The patients' brain volume is then registered into a template space along with the segmentation label. Connectome data from healthy subjects is then used to determine the set of disrupted nodes and edges at the lesion location. Depending on whether the lesion is located primarily in gray matter or white matter, different types of connectomes are used to identify disrupted nodes and edges. If the lesion is in gray matter, functional connectomes constructed from functional connectivity are used. In the other case, where the lesion is in white matter, a structural connectome is used. The reason that two different types of connectomes are used is because functional connectomes provide no connectivity information on lesions in white matter. The fMRI BOLD signal that is used for measuring functional connectivity is not considered detectable in white matter (Logothetis & Wandell, 2004). Structural connectomes on the other hand are able to provide disrupted node and edge information based upon what streamlines the lesion intersects whether it is in gray matter or white matter. However, if the lesion is in gray matter functional connectomes are typically preferred because they provide a richer measure of the underlying polysynaptic connection network (Logothetis et al., 2001). Once the network maps are constructed for a patient, they can be overlapped with network maps from other patients with similar symptoms to identify the connections most common to the symptoms.

Current CLSM approaches are in their infancy and suffer from multiple shortcomings. Typically, a patient's lesion connectivity is estimated by registering the patients T1-weighted volume into a template space containing a database of streamlines from a population of healthy subjects. Once the transformation has been estimated, the patient's lesion is normalized into the template space and intersected with the streamlines in the

database to produce a map of the lesion connectivity. However, this procedure only provides a generic estimate of a patient's lost connectivity, without any characterization of the patient's specific disrupted connectivity (Greene et al., 2019). Moreover, if the streamline database was constructed by performing tractography in the template space it produces even less accurate connectome mapping estimates (Greene et al., 2018). In Chapter 2, this issue is thoroughly explored and circumvented by developing a method that directly applies the transformation to streamlines to move them into the template space. These issues are further compounded by the database streamlines typically being biased against detecting long range connections because they were constructed using local-tracking approaches. In Chapter 3, a global shortest path approach is developed that overcomes these distance biases and that can be integrated into producing a streamline database. Alternatively, clinical researchers can perform tractography in the lesion area of the patient space but this is known to introduce spurious connections and less accurate connectome mapping because the lesions introduce significantly altered orientations of the fiber populations normal orientation (Greene et al., 2019). In Chapter 4, a new method is developed that not only restores the fiber diffusion models in lesion areas but also the orientations enabling both local and global tracking approaches and circumventing the need for mapping lesion connectivity with someone else's brain.

Chapter 2

Effect of spatial normalization approaches on tractography and networks

To facilitate the comparison of white matter morphologic connectivity across target populations, it is invaluable to map the data to a standardized neuroanatomical space. Here, we evaluate direct streamline normalization (DSN), where the warping is applied directly to the streamlines, with two publicly available approaches that spatially normalize the diffusion data then reconstruct the streamlines. Prior work has shown that streamlines generated after normalization from reoriented diffusion data do not reliably match the streamlines generated in native space. To test the impact of these different normalization methods on quantitative tractography measures, we compared the reproducibility of the resulting normalized connectivity matrices and network metrics with those originally obtained in native space. The two methods that reconstruct streamlines after normalization led to significant differences in network metrics with large to huge standardized effect sizes, reflecting a dramatic alteration of the same subject's native connectivity. In contrast, after normalizing with DSN we found no significant difference in network metrics compared to native space with only very small to small standardized effect sizes. DSN readily outperforms the other methods at preserving native space connectivity and introduces novel opportunities to define connectome networks without relying on gray matter parcellations.

2.1 Introduction

Over the past two decades, diffusion-weighted magnetic resonance imaging (DW-MRI) techniques have been used to non-invasively explore fiber bundle architectures in the brain by leveraging local estimates of anisotropy to reconstruct streamlines (virtual proxies of sets of collinear fibers tracts). These techniques have become an essential toolset for the diagnosis of developmental brain disorders (Chang & Zhu, 2013), pre-operative planning in neurosurgery (Golby et al, 2011; Jenabi et al, 2014), and the study of brain connectivity in healthy individuals (Van Essen et al., 2012). To enhance population based analysis of white matter morphology it is desirable to spatially normalize the reconstructed "fiber tracts" (herein called streamlines) into a standardized neuroanatomical space. Spatial normalization is routinely used in voxel based morphometry, structural MRI, and resting state fMRI. Embedding streamline connections into these morphologic and functional databases would be invaluable for furthering our understanding of structure-function relationships of the brain (Thiebaut de Schotten et al., 2016). Spatially normalized tractography is important because it enables the characterization of differences in white matter morphology due to developmental, genetic, disease, or injury across populations. For example, a method known as local termination pattern analysis (LTPA) leverages normalized tractography datasets to compare white matter morphology across populations by itemizing the pairwise cortical region termination connectivity for the subset of streamlines passing through a small cluster of voxels (Cieslak & Grafton, 2013; Cieslak et al., 2015). The termination patterns can be used to distinguish among groups. Spatially normalized tractography has also been used to construct structural connectivity networks in a standardized way (Jarbo & Verstynen, 2015;

Gu et al., 2015; Molesworth et al., 2015; Muraskin et al., 2016; Donos et al., 2016). Such methods also necessitate accurately normalized streamlines. Once normalized, there is opportunity to cluster fascicles across populations and to generate new types of cortical parcellations driven by white matter trajectories.

Spatial normalization of diffusion data typically begins by registering the set of DWIs to a higher resolution T1 weighted anatomic scan with a rigid body transformation. The latter is then registered to a template atlas, such as the Montreal Neurological Institute (MNI) atlas using one of a variety of algorithms that typically utilize both linear and higher order non-linear transformations with many degrees of freedom. Extensive prior work has compared the accuracy of different non-linear deformation algorithms (Klein et al., 2009) for mapping T1 weighted images, with leading performers including SyN, ART, IRTK, and DARTEL. These are notably superior to the dated non-linear deformation algorithms used in SPM and FSL. These algorithms are typically optimized over a similarity metric such as mean squared difference, cross-correlation, or mutual information. Here, we employ SyN. Once the mapping between the diffusion scans and template space has been determined, there are two basic approaches to create spatially normalized streamlines. The first is to transform the underlying diffusion information into the atlas and then perform streamline reconstruction. The second is to create the streamlines with respect to the original diffusion scans and then warp these streamlines to the atlas space. We first review the advantages and disadvantages of the former approaches (warping then streamline construction) and then propose the second approach (streamline construction followed by streamline warping) as a major improvement.

One approach for generating streamlines after normalization of diffusion information into template space involves reorientation of either diffusion tensors from DTI scans or fiber orientation distributions (FOD) derived from HARDI scans. The tensors or FODs rather than diffusion scans are subsequently reoriented (Alexander et al., 2001; Zhang et al., 2006; Hong et al., 2009; Raffelt et al., 2011, 2012). Irrespective of which of these sampling schemes are used, spatial reorientation at this step has undesirable effects. For example, prior work investigated the adverse effects of non-linearly warping DTI data by evaluating the consistency of the geometric shape of specific white matter pathways such as the corpus callosum and cingulum bundle (Alduru et al., 2016). Whole brain tractography in both the subject's native space and after tensor reorientation in the template space were performed and ROIs were used to extract known pathways. To measure the impact of spatial normalization on the shape of the tracts, the authors compared the overlap of the rasterized masks of the pathways. Unsurprisingly, they found the least amount of overlap between native and normalized pathways near the gray-white boundary, where white matter pathways begin to branch.

For FOD reorientation, another undesirable effect is that the maxima in the native FODs no longer corresponds to the maxima in the reoriented FODs (Christiaens et al., 2012). This is because the reorientation introduces dimple artifacts hypothesized to be from the negative lobes in the Gibbs ringing. This directly affects subsequent deterministic and probabilistic fiber tractography performed in the template space, producing streamlines that do not match the original streamlines from native space. Moreover, streamline distributions generated from probabilistic tractography performed on reoriented FODs are deflected with respect to the native tract distribution (Christiaens et al., 2012). Although the latest work in FOD

reorientation (FODR) using apodized point spread functions (PSFs) overcomes the dimple artifacts, slight distortions are still introduced into the spread of the fiber populations (Raffelt et al., 2012). On average the angular error between peak orientations is ~8° (Raffelt et al., 2012). The error in peak orientation accumulates into large errors when performing tractography after normalization (Colon-Perez et al., 2015). Moreover, an obvious drawback of these types of solutions is that they depend specifically on the diffusion sampling and reconstruction method used and do not generalize easily to other diffusion methods. Although FODR software was recently made public, it has not been applied to the study of population based tractography or structural network analysis.

Another approach for generating streamlines after normalization is to apply the non-linear spatial transformations to each of the DWIs and locally reorient the b-vector using the Jacobian of the deformation field to reconstruct the orientation distribution function (ODF). This approach has the merit of being generally applicable to any type of diffusion weighted scan, irrespective of the sampling scheme. DSI Studio (http://dsi-studio.labsolver.org) has a publicly available implementation of this approach known as q-space diffeomorphic reconstruction (QSDR) that works with HARDI and DSI sampling schemes (Yeh & Tseng, 2011). A multitude of work has used QSDR for comparing per-subject tractography and for constructing normalized structural networks (Cieslak & Grafton, 2013; Cieslak et al., 2015; Jarbo & Verstynen, 2015; Gu et al., 2015; Molesworth et al., 2015; Muraskin et al., 2016; Donos et al., 2016). However, the QSDR algorithm suffers from some limitations. First, it relies on the dated SPM2 spatial normalization algorithm that has been shown to have inferior registration performance compared to newer methods (Klein et al., 2009). Secondly, it relies on a single contrast modality, the quantitative anisotropy (QA) volume estimated

from generalized q-sampling imaging (GQI) reconstructed native space diffusion data (Yeh & Tseng, 2011), to register the native diffusion data to a QA template derived from diffusion scans with similarly low contrast and significant spatial inhomogeneity in the occipital lobe. Third, the mean angular error on simulated vertical fibers is 2.27° and likely higher with subject data. Critically, the nonlinear transformations required to transform brains of various shapes and sizes into a standardized space invariably introduces noise into the QSDR ODFs (Powell et al., 2017). Consequently, the resulting tractograms suffer from similar types of distortions that occur when tracking through reoriented tensors or FODs.

Given the problems that arise from spatially normalizing diffusion information prior to streamline construction, we sought to determine if direct streamline normalization (DSN), where the streamlines are created first, in the same space as the diffusion scans, followed by the warping of these streamlines into the template space would yield more precise results. In this case, the deformation fields from the normalization of each subject to the template are used for warping the streamlines (Hua et al., 2008; Thottakara et al., 2006). DSN confers multiple potential advantages. DWIs can be acquired with any desired sampling scheme. Diffusion tensors, FODs, or ODFs can also be reconstructed using any desired method and streamlines generated using any algorithm. Most importantly, it avoids the problem of generating streamlines from reoriented diffusion tensors, FODs, or ODFs that are distorted relative to their native counterparts which substantially reduces errors in tract morphology relative to the subject's native structure.

In this chapter, we assess the precision of the two publicly available DWI spatial normalization techniques (FODR and QSDR) and direct streamline normalization for warping tractography data to a standardized atlas. We investigate the impact of the different

normalization schemes on structural brain networks and topologic properties from a subject pool of 417 Human Connectome Project (HCP) subjects. For DSN, we utilize a publicly available symmetric diffeomorphic algorithm SyGN using ANTs, known for its registration accuracy and performance (Klein et al., 2009), to construct custom high-resolution multimodal templates and to directly normalize the streamlines (Avants et al., 2010). In our approach, we use T1w, T2w, and generalized fractional anisotropy (GFA) images to enhance the fidelity and contrast for the template generation and normalization for improved cortical and white matter alignment. Our comparison is distinct from prior efforts in this area (Alduru et al., 2016) because we use HARDI data that can resolve multiple fiber crossings, we analyze at a finer level than pathways and take into account how branching impacts structural networks.

We rely on several figures of merit to compare precision of the streamline normalization methods. First, we visually compare the quality of known white matter tracts such as the corticospinal tract before and after normalization. Second, we apply a set of gray matter regions of interest from native anatomic space to each subject's streamline data, also in native space. From this, native space connectivity matrices are extracted and used to estimate native space network properties. If the same gray matter regions are normalized and re-applied to the normalized streamlines, then all of the network properties measured in native space should be preserved in the atlas space. Similarly, the connectivity matrices themselves should be similar. In addition to quantifying dissimilarity statistically, we also report standardized effects sizes to capture the magnitude of error induced by each normalization method. We find large to very large effect sizes in the same subject’s network metrics after normalization with QSDR and FODR. In contrast, DSN has only very small to

small effects on the network metrics. Thirdly, we capitalize on the availability of twin data within the HCP database to further assess the precision of the different methods. We use pairs of identical twins, fraternal twins, non-twin siblings, and non-related subjects to characterize the inherent variability in structural brain networks. Identical twins have connectivity matrices that are significantly more similar to each other than strangers are to each other. This pattern of similarity should also be observed after successful spatial normalization. Here too, we show that preserving genetic influences on network metrics can be heavily influenced by the spatial normalization approach. The effects can be dramatic, with some methods changing the same subject's connectivity and network metrics after normalization to a relative distance that is comparable to a non-twin family member rather than to themselves. These comparisons demonstrate the significant gains that directly normalizing the streamlines achieves compared to the other methods at preserving the native tract structure and properties of structural brain networks.

2.2 Methods

2.2.1 Preprocessing

A. Imaging data

The dataset was collected as part of the Washington University-Minnesota Consortium Human Connectome Project (Van Essen et al., 2013). The data used was from the S500 release, consisting of structural and diffusion data from 489 participants. Data from 49 subjects were not used because the number of diffusion volumes was incomplete or suffered from artifacts. The structural and diffusion data were collected on 3T Connectome Skyra

system (Siemens, Erlangen, Germany) over a specified set of spatial and angular resolutions. The diffusion volumes were collected with a spatial resolution 1.25×1.25×1.25 mm, using three shells at b = 1000, 2000, and 3000 s/mm2 with 90 diffusion directions per shell and 10 additional b0s per shell. The diffusion data was corrected for geometric and eddy current distortions, using information from acquisitions in opposite phase-encoding directions, as well as head motion (Glasser et al., 2013). The high-resolution structural T1w and T2w volumes were acquired on the same scanner at 0.7mm isotropic resolution (Glasser et al., 2013).

B. Multimodal template construction

GFA volumes for each subject were extracted from their GQI reconstructed HARDI data in DSI Studio. Previously skull stripped, aligned, and distortion corrected T1w and T2w volumes were obtained for each subject (Glasser et al., 2013) and then rigidly registered to the subject's GFA volume. ANTs symmetric group wise normalization (SyGN) method was used to construct a custom multimodal population specific brain template from 40 HCP subjects using 5 iterations (Avants et al., 2010). The subjects were chosen through stratified random sampling to give each racial, gender, and handedness group a representation in the template. It has been previously shown that normalization to a custom template improves localization accuracy, reduces bias in statistical testing, and ultimately yields more biologically plausible results during analysis as opposed to using a standardized MNI template that wasn't constructed from the subject pool (Kim et al., 2008). Each subject's image set input into SyGN consisted of GFA, T1w, and T2w volumes weighted 0.5×1×1 respectively. SyGN combines information from different modalities to improve the quality of gray and white matter mappings because where information may be locally homogeneous

in one modality it's heterogeneous in another modality. The resulting high-resolution (1.25 mm^3 isotropic) multimodal templates are viewable in Figure 1.

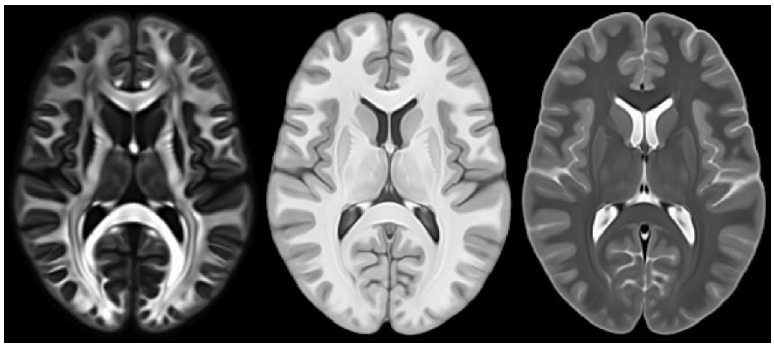

Figure 1: High-resolution multimodal templates generated using SyGN from 40 HCP subjects. From left to right: GFA, T1w, and T2w. SyGN leverages information from the multiple modalities to create the most optimal and unbiased template with respect to shape and appearance. Notice that SyGN preserves the shared sharp features across the subjects that are visible in the caudate, putamen, thalamic, and frontal regions while optimally representing the finest shape differences in the occipital area.

C. Reconstruction

417 HARDI HCP datasets were reconstructed using generalized q-sampling imaging (GQI) with a mean diffusion distance of 1.25mm using five fiber orientations per voxel (Yeh et al., 2010). They were also reconstructed using constrained spherical deconvolution (CSD) with a maximum harmonic order of 8 (Tournier et al., 2004). The largest b-value shell was used during reconstruction.

2.2.2 Spatial normalization of diffusion data

A. Direct streamline normalization (DSN)

The remaining 400 HCP subjects T1w, T2w, and GFA volumes were spatially normalized to our template using the same registration parameters that were used in the template creation process. The chosen SyGN parameters for both template creation and registration are a 0.1 gradient step size, cross-correlation as the similarity metric, time based SyN with symmetric gradient estimation (t = SY), with a maximum number of iterations of 100×100×50 from the coarsest to the finest level of the pyramid. Each streamline consists of a set of (x, y, z) coordinates in tract space. The streamline coordinates are then converted into the subject's native voxel coordinates, allowing the application of the warps from the registration. The subject's streamlines were estimated using ODF maxima from GQI reconstructed data. They were directly warped into the multimodal template space, with a single interpolation by applying the affine and deformation field simultaneously to each (x, y, z) point coordinate of each streamline, preserving the native tract structure. Normalization steps were performed using Advanced Normalization Tools (ANTS). Our software (http://github.com/clintg6/DSN) interfaces with the warp fields generated by ANTs and can be applied to streamlines generated by any diffusion imaging technique.

B. Q-space diffeomorphic reconstruction (QSDR)

QSDR is the generalized form of GQI that enables the reconstruction of ODFs in any template space. Its aim is to preserve fiber orientations and the number of diffusion spins under transformation. It is universal and works with DTI, single and multi-shell HARDI, and DSI (Yeh & Tseng, 2011). QSDR first reconstructs the raw diffusion data using GQI and extracts the primary QA volume, which is then registered to the MNI QA template. The raw DWIs are then normalized into the MNI space using the same transformation. The Jacobians outputted from the deformation are then used to properly reorient the b-vectors locally as each voxel's ODF is reconstructed in the template space. The 417 HARDI HCP datasets were separately normalized into 1mm MNI space using QSDR with a mean diffusion distance of 1.25mm and five fiber orientations per voxel. Attempts were made to reconstruct into our custom $1.25mm^3$ template space but the SPM normalization algorithms in QSDR failed to converge to our template even with heavy regularization. Resorting to the built in method, the R^2 value from the subject's QA to the MNI template QA was on average 81, suggesting the SPM normalization performed well with the built in MNI QA template.

C. Fiber orientation distribution reorientation (FODR)

FODs generated from CSD in mrTrix were reoriented using apodized PSFs (Tournier et al., 2012). Specifically, each FOD is decomposed into a series of weighted spherical harmonic PSFs. The amplitude of the negative lobes of the PSFs are reduced, then each PSF is reoriented using the local affine transformation estimated from the Jacobian of the total deformation field, and finally recombined into the full reoriented FOD (Raffelt et. al, 2012). The warps used for reorientation were the ANTs outputs from each subject's symmetric diffeomorphic registration to our custom multi-modal template.

D. Tractography

Fiber tracking was performed in DSI Studio with an angular cutoff of 60°, step size of ½ the voxel length, minimum length of 10mm, smoothing of 0.0, maximum length of 420mm. FODs/reoriented FODs were converted into DSI Studio format by identifying the 3 largest peaks, with 60 directions for peak finding. An improved and top performing (ISMRM 2015 Tractometer Challenge) deterministic fiber tracking algorithm was used until 100,000 streamlines were reconstructed for each subject (Yeh et al., 2013).

2.2.3 Network construction

Although there are many methods for spatially normalizing data, none to our knowledge has measured the impact on a diffusion based structural brain network. To investigate the impact on structural networks, we constructed connectivity matrices in native space using GQI, native space using CSD, template space via DSN, template space via FOD reorientation, and MNI space via QSDR. A schematic of the workflow can be found in Figure 2.

A. Parcellation

T1 anatomical scans were segmented using FreeSurfer (Dale et al., 1999) and parcellated according to the Lausanne 2008 atlas (Daducci et al., 2011; Hagmann et al., 2008) included in the connectome mapping toolkit. We rigidly registered the scale 60 (129 regions) parcellation to the b0 volume from each subject's HARDI data for network construction.

We directly transform the parcellation ROIs into the template space using the same approach as for streamlines. For every native space voxel containing a label, $v_n = [x_n,y_n,z_{n]}$, it's coordinates are transformed directly into the template space using the subject's ANTs transformations as $v_t = [x_t, y_t, z_{t]}$ and the native space label is carried over to the new coordinate, v_t. For QSDR, we used the output voxel mapping from DSI Studio to directly transform the parcellation ROIs into MNI QA template space.

B. Connectivity matrix

In order to attain regional based connectivity, a set of N = 129 brain region masks from the Lausanne scale 60 atlas were applied to the reconstructed fiber tracts. We determined the number of tracts that originate in one mask, i, and terminate in another mask, j, for all possible pairs of N masks, creating an N×N inter-regional anatomical connectivity matrix, M_{ij}, where the value of any element of the matrix M_{ij} is equal to the count of tracts originating in mask i and terminating in mask j. These matrices were constructed for each of the 417 subjects native space GQI, native space CSD, QSDR, and FOD reoriented, and DSN streamline sets using streamline count between region pairs. The parcellations and tracking parameters were the same for all datasets and methods.

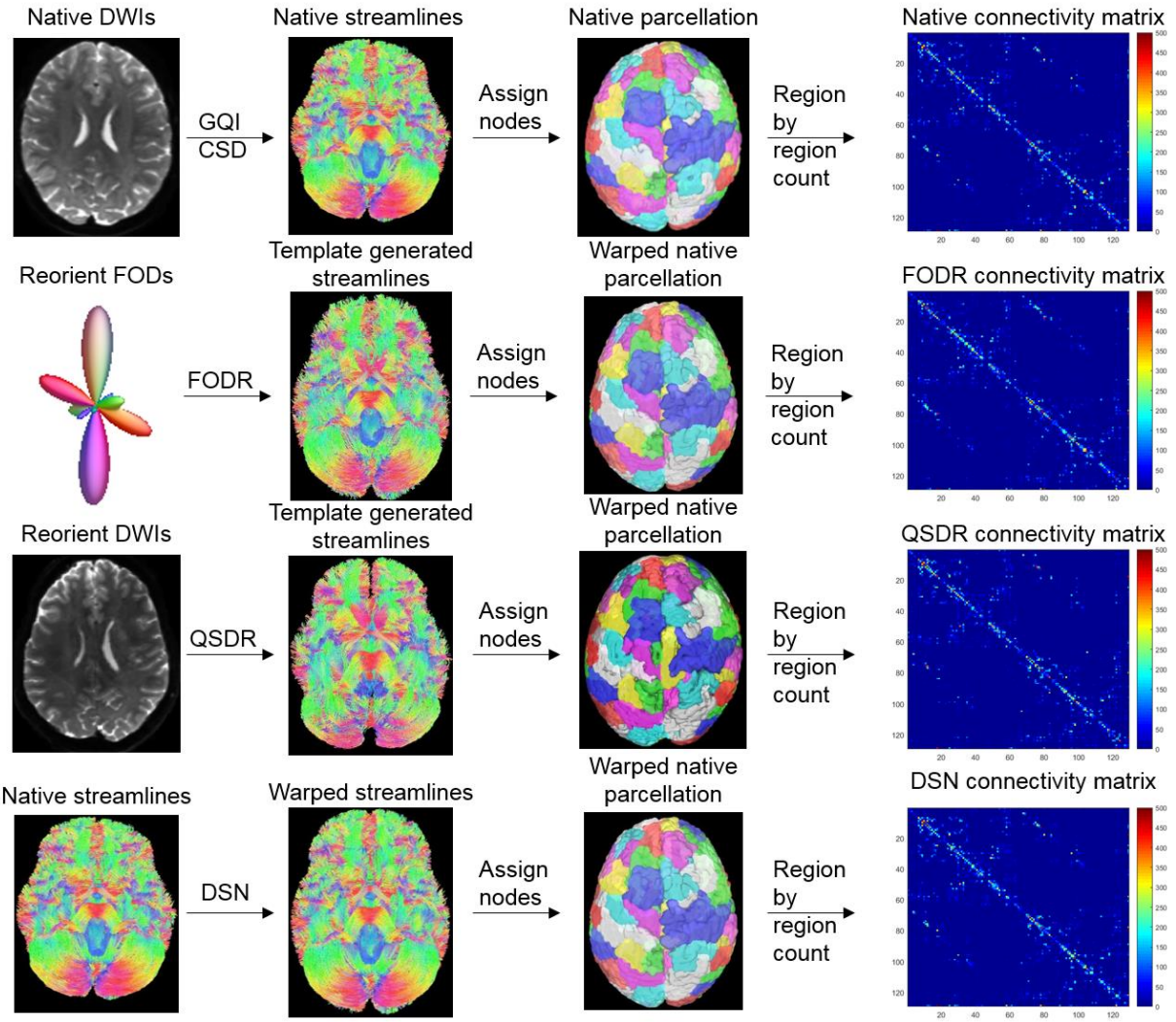

Figure 2: Schematic of network construction in native and template space for a single subject. Native space HCP HARDI data was reconstructed using GQI and CSD for each subject. Deterministic tractography was performed separately for the GQI and CSD reconstructed native space data. The native space data was reconstructed using CSD to fairly compare the impact of FODR. The scale 60 Lausanne parcellation was applied to assign nodes to the streamlines. The structural connectivity matrix was weighted using streamline count. For FODR, the native space FODs reconstructed using CSD were reoriented according to the deformation field output by ANTs. The subject's native space parcellation was warped into the template space using the same deformation field output by ANTs. The raw HARDI data was reoriented as well as the b-vectors to reconstruct ODFs in template space for QSDR. The subject's native space parcellation was warped into the template space using QSDR's internal mapping. Deterministic tractography was performed for FODR and QSDR after normalization. The native space streamlines generated from ODFs reconstructed using GQI were directly warped into template space using the deformation field output by ANTs. Node assignment and network construction for FODR, QSDR, and DSN follow the same workflow as in native space. After the connectivity matrices are constructed, the impact of different spatial normalization approaches can be measured by comparing the similarity of the connectivity matrices and network metrics derived from them for the same subject before and after normalization.

2.2.4 Similarity measures

To test the disagreement between connectivity matrices constructed in native space vs. template space for the various methods, we chose the Generalized Jaccard Distance. This distance is a natural generalization of the Jaccard distance over sets with weighted elements. It is defined as $D_j = 1 - \frac{\sum_{i=1}^{n} min(N_i,T_i)}{\sum_{i=1}^{n} max(N_i,T_i)}$, where N,T are flattened native space and template space connectivity matrices and varies between [0,1]. A value of 0 for Jaccard distance indicates complete similarity between native space and template space connectivity, whereas a value of 1 means complete dissimilarity. Prior work has shown this distance to satisfy the triangle inequality (Charikar, 2002).

2.2.5 Network analysis

Weighted network properties such as density and assortativity were estimated using the Brain Connectivity Toolbox (Rubinov and Sporns, 2009). These network measures were used to further characterize the impact spatial normalization has on structural brain networks.

A. Average degree

The average degree of a network, $\langle k \rangle = \frac{2E}{N}$, is the mean of the degree distribution and is closely related to network density. To capture the intersubject variability in degree distribution before and after normalization, we compute the difference in mean degree distribution between native and template $\langle k_N \rangle - \langle k_T \rangle$ for each subject.

B. Density

The network density, D, is defined as the number of non-zero edges in the network, E, divided by the total number of possible edges in the network $D = \frac{2E}{N(N-1)}$, where N is the number of nodes in the network, or in this case the number of or brain regions. The density is therefore proportional to the total number of connected pairs of brain regions, irrespective of the number of tracts passing between those pairs.

C. Assortativity

The assortativity measures the preference of a brain region to connect to other brain regions of similar degree (leading to an assortative network, A > 0) or to other brain regions of very different degree (leading to a disassortative network, A < 0). The assortativity of a network is defined as,

$$A = \frac{E^{-1}\sum_{i=1}^{n} j_i k_i - [E^{-1}\sum_{i=1}^{n}\frac{1}{2}(j_i+k_i)]^2}{E^{-1}\sum_{i=1}^{n}\frac{1}{2}(j_i^2+k_i^2) - [E^{-1}\sum_{i=1}^{n}\frac{1}{2}(j_i+k_i)]^2}$$

where j_i,k_i are the degrees of the nodes at either end of the ith edge, with i = 1…E.

Social networks are commonly found to be assortative while networks such as the internet, World-Wide Web, protein interaction networks, food webs, and the neural network of C. elegans are disassortative (Bassett et al., 2011).

2.2.6 Effect size

We estimate effect size using Glass' delta estimator that uses only the standard deviation from native space, $\Delta = \frac{\mu_N - \mu_T}{s_N}$, where μ_N is the native space mean, μ_T is the template space mean, s_N is the standard deviation of the native space group.

2.2.7 Structural network variability

We estimate structural network variability across 84 identical twins, 70 fraternal twins, 54 non-twin siblings, and 84 non-related subjects (randomly sampled from exhaustive pairing, ${}_{229}C_2$) by measuring the Generalized Jaccard Distance of the respective pairs connectivity matrices and the R^2 of metrics derived from them to provide a frame of reference for the variability introduced by different spatial normalization approaches into structural networks after normalization.

2.3 Results

2.3.1 Qualitative comparison

Whole brain tractograms generated using the same streamline construction parameters for a single HCP subject are visible in Fig. 3 for: (A) Native space, (B) DSN, (C) FOD reorientation, and (D) QSDR. From visual comparison of local or global features, it is apparent that the DSN tract set most closely resembles the Native set. The QSDR set least

resembles the Native set, followed by FOD reorientation. We can see this by closely examining the region near the optic chiasm where a large discrepancy is apparent for FOD reorientation and QSDR with respect to Native space. Comparison of endpoints, where streamlines terminate at the gray-white boundary also demonstrate that DSN markedly preserves the Native branching structure compared to the other normalization methods.

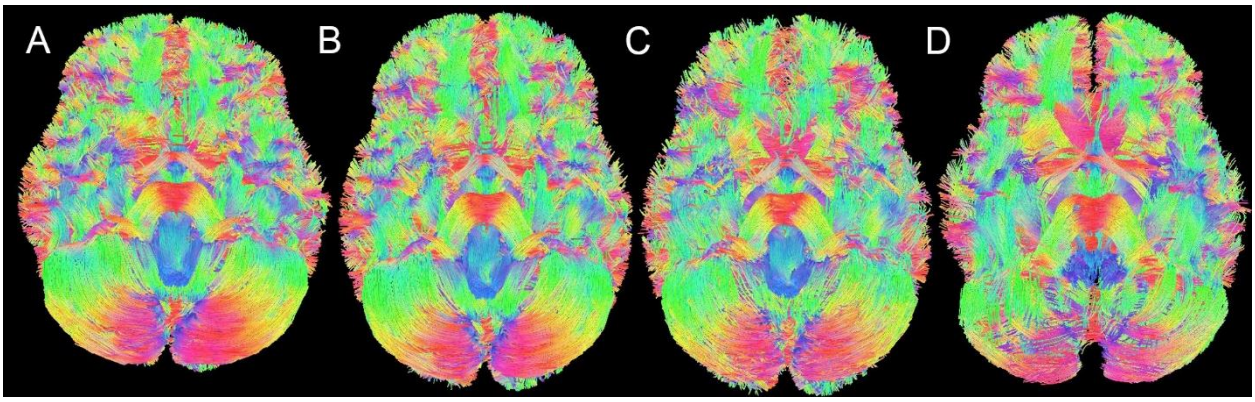

Figure 3: Full brain tractography from left to right for a single subject: (A) Native space, (B) DSN, (C) FOD reorientation, and (D) QSDR. Our DSN tract set most closely resembles the Native set. QSDR shows the least resemblance, followed by FOD reorientation to the native set. There is a large discrepancy in the optic chiasm region for FOD reorientation and QSDR compared to native space. DSN most closely preserves the native tract structure.

In addition to this global inspection, we also considered the impact of the normalization scheme on a predefined tract. We used a single region of interest, first applied in native space, to define the corticospinal tract (CST) in a single subject, as shown in Fig. 4. The same ROI defined in Native space was warped into each respective template space using the deformation field from the normalization and the CST for each method was identified. DSN again excellently preserves the native tract structure in template space, visually outperforming the other normalization methods. QSDR and FODR introduce significantly more variation in the tract structure relative to native space. Notice that the branching seen in Native space is most closely matched for DSN compared to QSDR or FODR. The Native

CSD set uses a different reconstruction technique compared to the Native GQI, resulting in a fundamentally different representation of the CST.

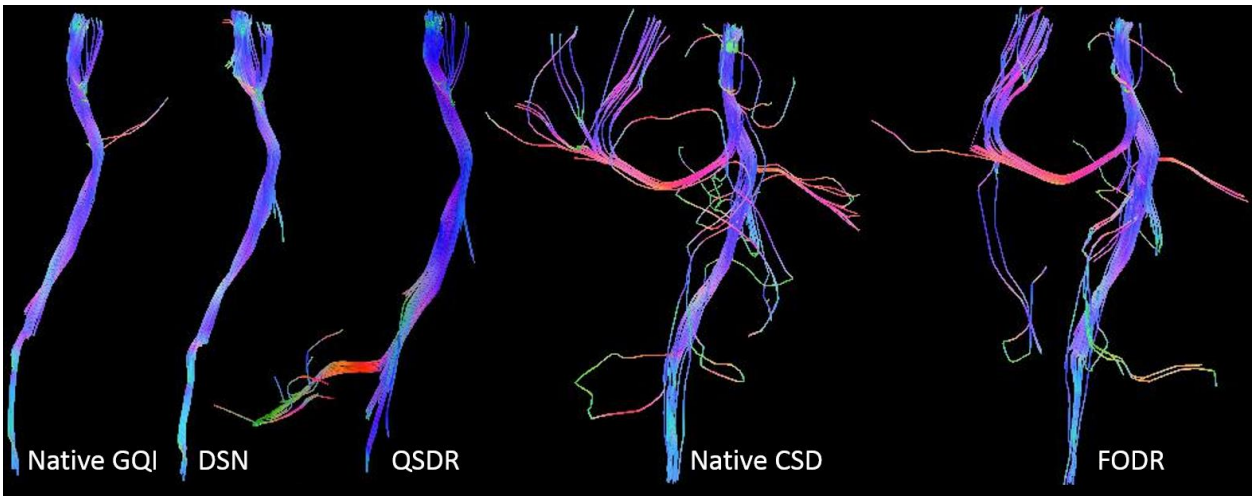

Figure 4: Effect of spatial normalization on the structure of the corticospinal tract (CST). Streamlines were selected using the same Native space ROI warped according to deformation field from the normalization for each method. It is obvious from visual comparison that DSN strongly preserves the native structure compared to QSDR and FODR which introduce variation that is not seen in their Native space counterparts. DSN most closely matches the branching in Native space compared to QSDR and FODR.

2.3.2 Quantitative Comparison

To quantify the degree of variation that the different normalization methods introduce, we measured the Generalized Jaccard distance between 417 subject's native space connectivity matrices before and after normalization. This distance measures the normalized similarity between native space connectivity and template space connectivity, such that a distance of 0 is complete similarity and 1 is complete dissimilarity.

Histograms of the distance for each method are plotted in Fig. 5. DSN significantly outperforms QSDR and FOD reorientation in preserving connectivity (1-way repeated measures ANOVA, $p < 2^{-16}$). Summary statistics are available in Table 1. The mean distance for DSN is much smaller at 0.09 compared to QSDR and FODR 0.37 and 0.40 respectively.

There is no overlap between the DSN distance distribution and the other method's distributions. Moreover, the spread of the DSN distribution is also much tighter compared to QSDR or FODR, with a standard deviation of 0.005 versus 0.016 and 0.034. Mean + SD error bars are plotted above each distribution in Fig. 5.

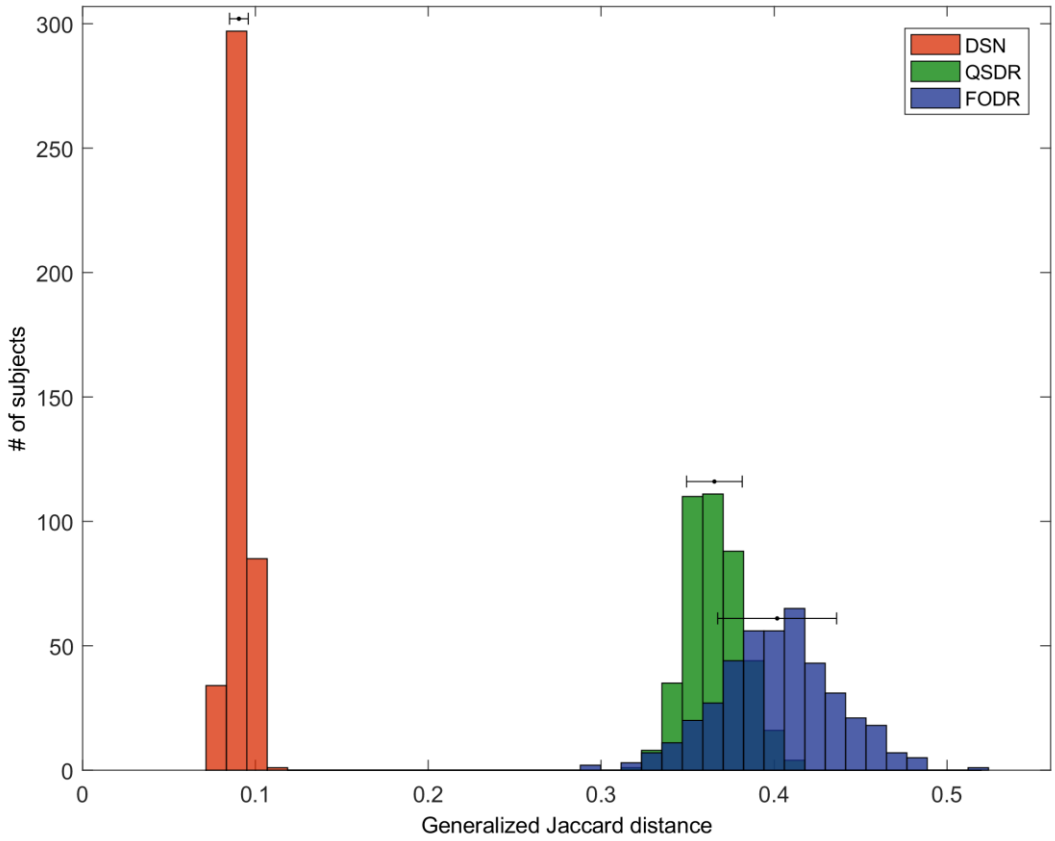

Figure 5: Histograms for all HCP subjects for Generalized Jaccard Distance between a subject's native space connectivity matrices and template space connectivity matrices for the different spatial normalization methods. DSN (red) significantly outperforms QSDR (green) and FODR (blue). Mean + SD error bars are plotted above each distribution (black). There is no overlap between the DSN distance distribution and the QSDR and FODR distributions. The mean DSN distance is much smaller at 0.09 compared with 0.37 and 0.40 for QSDR and FODR. DSN distribution also has a narrower spread with a standard deviation of 0.005 compared with QSDR and FODR whose standard deviations are 0.018 and 0.034 respectively. Under one-way ANOVA, DSN distances test significantly smaller than QSDR and FODR with a p-value $< 2^{-16}$.

We also measured and plotted the effect of normalization on typical structural brain network measures such average network degree and network density and assortativity in Figure 6 for each subject and method: DSN (red), QSDR (green), FODR (blue) and summarized in Table 1. DSN preserves the average network degree with a mean of -0.27 compared to QSDR's 4.54 and FODR's 14.43 difference in edges before and after normalization (Table 1). Moreover, the standard deviation in the average difference in network degree is also much smaller for DSN, 0.17, compared to QSDR and FODR, 0.95 and 3.18 respectively. The native space network density for each subject was plotted against the network density in template space. DSN preserves network density with an R^2 of 0.99 versus 0.66 and 0.82 for QSDR and FODR respectively (Table 1). Mean network density in native space is 0.29 for GQI reconstruction and 0.62 for CSD reconstruction, showing that QSDR and FODR decrease the number of edges after normalization, while DSN on average doesn't change the number of edges. This change is also reflected in the difference in average network degree scatter plot where the QSDR and FODR plots illustrate that after normalization the number of edges decreases and remains nearly unchanged for DSN. Because average network degree and network density are linearly rescaled versions of each other (see Methods) the R^2, p-value, effect size of average network degree are the same as for network density and are not included in Table 1 to reduce redundancy. DSN also dramatically outperforms the other methods at preserving network assortativity. Under Welch's paired t-test with $\alpha = 0.0001$, FODR and QSDR significantly alter network metrics with changes characterized by large to very large effect sizes (Δ), while DSN only has very small to small effects and doesn't significantly alter them. For network assortativity the mean in native space for GQI and CSD are respectively, -0.015 and -0.022. DSN and FODR

preserve the known disassortativity of structural brain networks while QSDR tends to make a subject's network after normalization more assortative. The network statistics from the 417 subjects' data demonstrate DSN's improvement over QSDR and FODR at preserving networks properties after normalization.

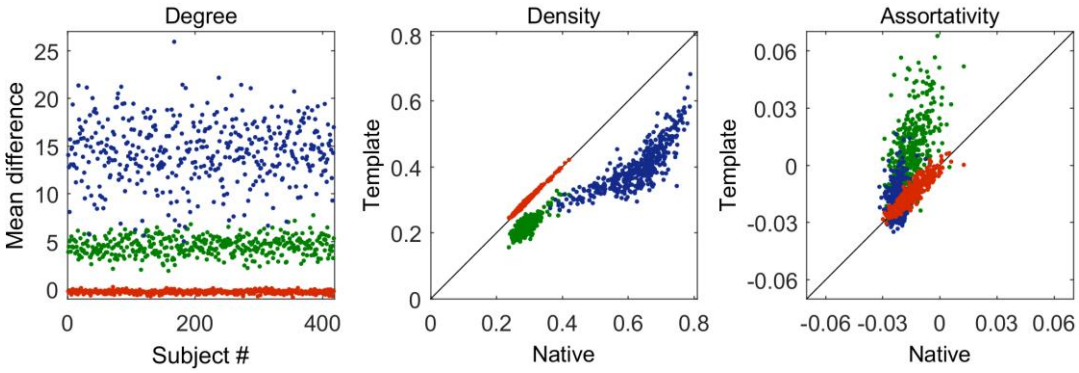

Figure 6: Scatter plots from left to right: difference in average network degree between native space and template space and network density and network assortativity for native space vs template space for DSN (red), QSDR (green), and FODR (blue). Unity slope line (black). There is excellent agreement between native space networks and template space networks normalized using DSN compared to QSDR and FODR. Statistics for the metrics are summarized in Table 1.

	Measurement									
	$\langle k_N \rangle - \langle k_T \rangle$		Density				Assortativity			
Method	μ	$\sqrt{\sigma}$	μ	R^2	p	Δ	μ	R^2	p	Δ
DSN	-0.27	0.17	0.29	0.99	0.0006	0.24	-0.015	0.90	0.99	6.4e-5
QSDR	4.54	0.95	0.39	0.66	5.1^{-289}	4.04	0.0064	0.50	2.2^{-86}	3.17
FODR	14.43	3.18	0.21	0.82	1.3^{-202}	2.59	-0.019	0.11	6.4^{-14}	1.07

Table 1: Difference in average network degree and network metric statistics summarized for the three methods. Each measure compares the same subject's network before and after normalization. Changes to network metrics are described by effect sizes (Δ).

To characterize the inherent variability in structural brain networks between different subjects, we computed the mean generalized Jaccard distance for native space and each normalization method for pairs of identical twins, fraternal twins, non-twin siblings, and unrelated subjects summarized in Table 2. As expected, in native space the mean pairwise distance between identical twins is smaller (.41-.42) compared to the other groups (.46-.50).

Identical twin pairs network Jaccard distance is significantly smaller than fraternal twins, non-twin siblings, and unrelated subject's pairs distance for all methods (1-way repeated measures ANOVA, $p < 0.0007$). No significant difference was found among distances from fraternal twin, non-twin sibling, and unrelated subject pairs. For the three normalization methods, the mean and standard deviation of the pairwise Jaccard distances for each group are nearly identical Table 2.

Method	**Familial Generalized Jaccard Distance**							
	Identical twins		Fraternal twins		Non-twin siblings		Not related	
	μ	$\sqrt{\sigma}$	μ	$\sqrt{\sigma}$	μ	$\sqrt{\sigma}$	μ	$\sqrt{\sigma}$
Native	0.42	0.020	0.47	0.067	0.47	0.061	0.49	0.057
DSN	0.42	0.020	0.47	0.065	0.47	0.060	0.49	0.056
QSDR	0.42	0.021	0.47	0.071	0.48	0.061	0.50	0.057
FODR	0.41	0.021	0.46	0.063	0.47	0.062	0.49	0.058

Table 2: Familial generalized Jaccard distance for connectivity matrices for native space and each normalization method for pairs of identical twins, fraternal twins, non-twin siblings, and exhaustively for each subject to every unrelated subject.

To further investigate the impact of normalization method on preserving heritable features of brain connectivity, we computed the correlation of network density and assortativity between pairs of identical twins, fraternal twins, non-twin siblings, and non-related subjects for native space and each normalization method. The R^2 between non-related subjects for network density and assortativity was ~0. For the other pair types, network density shows stronger correlations than network assortativity. Network density is significantly more similar for identical twin pairs relative to unrelated subjects but not to other pair types in native space and for DSN (1-way repeated measures ANOVA, $p < 0.002$). With QSDR no significant difference was found for any pair type. However, for FODR significant differences were found for identical twins relative to non-twin siblings

and unrelated subjects, $p < 0.002$. For network assortativity, no significant difference was found across the pair types using 1-way repeated measures ANOVA for native, DSN, and FODR. A significant difference was found for QSDR between non-twin siblings and unrelated subjects, $p < 0.02$. The results, summarized in Table 3, suggest that network density is more heritable than assortativity suggesting that genetic similarity only predicts network metric similarity up to a point. Comparing the three normalization methods, each network measure obtained with DSN most closely matches the correlations seen before normalization in native space agreeing with the significant findings in Table 1.

Method	**Familial Similarity of Network Metrics**							
	Identical twins		Fraternal twins		Non-twin siblings		Not related	
	R^2							
	Assortativity	Density	Assortativity	Density	Assortativity	Density	Assortativity	Density
Native	0.52	0.75	0.46	0.29	-0.04	0.28	~0	~0
DSN	0.49	0.76	0.53	0.31	0.07	0.33	~0	~0
QSDR	0.58	0.69	0.28	0.27	0.31	0.31	~0	~0
FODR	0.53	0.85	0.36	0.61	0.64	0.33	~0	~0

Table 3: Familial similarity of network metrics for identical twins, fraternal twins, and non-twin siblings.

The results summarized in these tables show that spatial normalization affects the structural connectivity and depending on the chosen method the impact can be significant. DSN does not significantly alter the two tested structural brain networks properties: network density and assortativity. QSDR and FODR significantly impact a given subject's brain network such that the distance between that same subject's connectivity and network metrics after normalization are more comparable to a non-twin family member rather than to themselves.

2.4 Discussion

We compared three methods for spatially normalizing streamlines reconstructed from diffusion imaging data into a standardized atlas. Two of these publicly available methods rely on warping of diffusion information followed by streamline reconstruction (QSDR and FODR) and the third method, DSN, directly warps the streamlines into the template space with a single interpolation. We showed that DSN readily outperforms them at preserving key native tract structure and anatomic properties of structural brain networks after spatial normalization using 417 HCP subjects. It also has additional advantages of being generalizable to any diffusion tractography imaging method.

Current approaches for generating streamlines after spatially normalizing DWIs for population based analyses suffer from two significant limitations. First, most of these methods depend specifically on the diffusion sampling and reconstruction method used and do not generalize easily to other methods (Alexander et al., 2001; Zhang et al., 2006; Hong et al., 2009; Raffelt et al., 2011, 2012). QSDR overcomes these limitations by using GQI to reconstruct q-space datasets acquired through either grid or shell sampling schemes in MNI space (Yeh & Tseng, 2011). But QSDR also suffers from the second and most significant limitation that also plagues FODR and tensor reorientation approaches, distortions to the maxima of the ODF. With reorientation approaches, the maxima in the native FODs no longer correspond to the maxima in the reoriented FODs (Christiaens et al., 2012). Mean angular error (MAE) for FODR between peak orientations is ~8° (Raffelt et al., 2012). With QSDR, it is known that the maxima before and after normalization do not perfectly correspond—MAE is 2.27° on simulated vertical fibers and likely higher on subject data.

The distortions to the normalized QSDR ODFs are responsible for the distance between native space and template space connectivity matrices because they produce small errors in the maxima of the ODFs that accumulate into large errors in the tractogram when performing deterministic tractography i.e. producing streamlines in template space that do not match the original streamlines from native space (Lazar, 2010). How much less distortion to QSDR ODFs could be gained by using an updated multi-modal registration algorithm remains an open question. Our results show significant dissimilarity with large to huge effect sizes in the same subject's network distance and metrics after normalization with QSDR and FODR. In fact, QSDR and FODR introduce so much distortion into any given subject's streamlines that a subject's network after normalization would more closely resemble a non-twin family member's brain network rather than their own.

Another significant advantage of the DSN approach over QSDR is that the overall accuracy of spatial normalization can be improved by incorporating a multimodal symmetric diffeomorphic normalization framework. To do this we first created a custom high-resolution multimodal template from 40 HCP subjects chosen through stratified random sampling to give each racial, gender, and handedness group a representation using ANTs (Avants et al., 2010). T1w, T2w, and generalized fractional anisotropy (GFA) images enhanced the fidelity and contrast of the template generation and normalization, maximizing both cortical and white matter alignment. The resulting affine and deformation field outputs from the SyN registration are applied to each (x, y, z) coordinate of each streamline. This reliably projects the native streamline structure into the custom template space. Moreover, because DSN accurately preserves tract structure and connectivity, it introduces important opportunities for developing a host of clinical and neuroscientific applications. Clinically,

there is potential to use DSN to develop a database of anatomically consistent connectivity independent of any cortical parcellation from healthy subjects. With this, estimates of disconnected cortical regions in individual brain injured patients can be derived as in Figure 7. Current approaches that identify network structure based solely on native space parcellations lack this ability to probe the relationship between subcortical damage and cortical disconnection at a population level. DSN enables the construction of edge density images (EDI) in Figure 7 that can be used to map network edge properties across target populations. Moreover, it also provides a reliable way to generate new types of cortical parcellations driven by clustering of white matter connectivity, since the tracts themselves can be spatially normalized across large populations. With this it can be used to investigate how the connectome varies across target populations, extending from the voxel scale of analysis all the way up to entire white matter pathways.

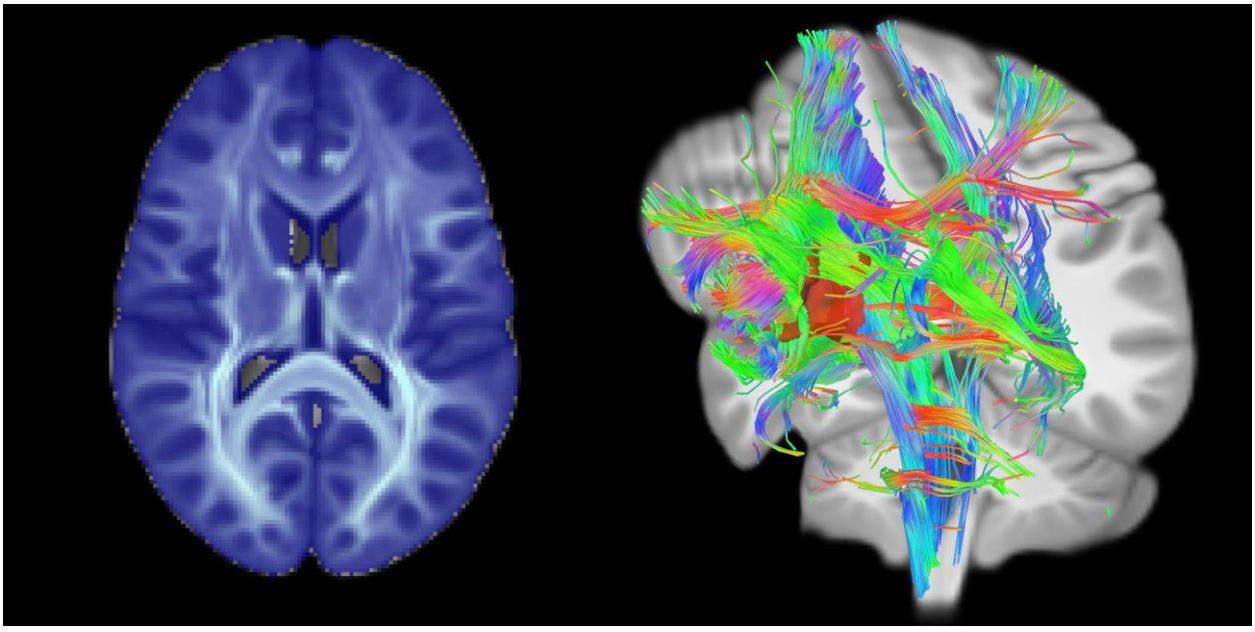

Figure 7: DSN supports many applications: Average edge density image (EDI) constructed from edge trajectories of 417 HCP subjects (left). Cortical disconnection maps can be constructed by querying streamlines that pass through a brain injured subjects warped lesion ROI (right).

Prior work evaluating streamline normalization has highlighted the potential for adverse effects that occur with non-linearly warping of DTI data followed by tractography (Alduru et al., 2016). Alduru and colleagues found that the least amount of overlap between native and normalized pathways occurs near the outskirts of streamlines, where the pathways begin to branch. The disparity we see in our results between structural network topology and metrics derived in native space and template space is due in part to the mismatch between branching patterns of the streamlines. The branching pattern mismatch is smallest when normalizing with DSN compared to FODR and QSDR because DSN doesn't rely on tracking through distorted maxima. The errors from tracking through reoriented data accumulate into the mismatch between branching patterns, which are visually obvious for CST in Fig. 4. Despite their findings, Alduru et al., concluded that tracking after normalization preserves shape and produces anatomically consistent structures compared to tracking in unwarped native DTI (Alduru et al., 2016). Our results show that tracking after normalization doesn't reliably preserve shape, especially where streamlines begin to branch and terminate because if it did preserve them there would be little impact to the subject's network and its properties. It is critical that a subject's network topology and streamline structure in native space is preserved in the template space because it is this structure that might uniquely vary across different populations and enable the characterization of differences in white matter morphology due to developmental, genetic, disease, or injury across populations using tools such as LTPA (Cieslak & Grafton, 2013; Cieslak et al., 2015). While we relied on deterministic tractography from multi-shell HCP HARDI data for analyzing the impact of spatial normalization on structural brain connectivity, the disruption to subject's brain networks and streamline reconstructions are guaranteed to also apply to

any sampling scheme like DTI or DSI. We chose deterministic tractography because it was applicable to all three methods and generates the same tractogram each time it's calculated, unlike probabilistic approaches, allowing us to tease apart how much of the distortion is driven by the normalization. Past work suggests that probabilistic tractography is affected less by reorientation than deterministic tractography so if tractography is performed after normalization probabilistic methods should be employed. Nevertheless, they are also affected due to aliasing artifacts and changes to the seeding distribution which distort the spread of the fiber population (Christiaens et. al, 2012). We recommend performing tractography in native space and then normalizing with DSN to make population based comparisons of white matter connectivity in a standardized template space.

None of the methods for spatially normalizing streamlines reconstructed from diffusion data perfectly preserve the structural brain network. The discrepancy between streamlines and networks before and after spatial normalization for FODR and QSDR are due to tracking through distorted maxima. For FODR the mismatch is due to reorientation introducing distortions to FOD maxima via lobe reshaping and interference (Christiaens et al., 2012). For QSDR, the maxima mismatch is also likely due to ODF lobe reshaping and interference. Despite DSN avoiding the issue of tracking through distorted ODFs, it isn't perfect and introduces slight perturbations into subject's networks after normalization. These perturbations are a result of a small subset of each subjects's native space voxels (μ = 1.03%) containing different parcellation labels being transformed to the same voxel coordinate in the standardized space. This is an unavoidable consequence of resampling a parcellation into a new volume because certain locations in a subject's brain that undergo compression and expansion during the normalization can result in a subset of voxels being

mapped to the same voxel coordinate in the template space. If this occurs near the interface between different parcellation labels then a voxel in the template space that has multiple voxels mapped to it can be assigned multiple labels, where the final label at that voxel is the last label it was assigned. When the connectivity matrix is constructed in the standardized space, a small subset of the streamlines passing through these voxels can be assigned a new label that doesn't match the original native space label. Since the Jaccard distance and network metrics depend on the preservation of streamline count, a slight discrepancy results between native and template space DSN networks. These relabeling issues do not affect FODR and QSDR connectivity matrices because the streamlines constructed in the template space and consequently the connectivity matrices are unique relative to the native space ones.

Changes induced by QSDR and FODR to network density are also due to a subset of the streamlines not connecting pairs of nodes. Even streamlines in native space can be unassigned but the proportion increases when tracking after normalization, reducing the number of edges in the structural network. The increase in sparsity is also evident in the difference in average node degree in Figure 6, where the node degree on average is 5 edges less for QSDR and 14 edges less for FODR in the standardized space. It is unclear why QSDR and FODR reduce the density after normalization and why QSDR increases the assortativity relative to native space.

Using different relatively coarse measures of white matter connectivity, we showed that structural brain network similarity and density are strongly heritable across monozygotic twin pairs. Similarity of white matter morphology, such as obvious similarity in the shape of the corpus callosum has been described previously (Gazzaniga, M. S., 1989). Our results

extend this morphologic observation by demonstrating that estimates of inter-regional connectivity are also driven by heritability. However, the lack of statistical significance for similarity and metrics for identical twins to other family pair types is likely due to the small sample sizes and the metrics not being heritable or too crude. Further analysis of the heritability metrics is beyond the scope of our current investigation. Future studies will be needed to determine if this heritability is a global feature or a property of specific circuits.

DSN overcomes both of the limitations of QSDR and FOD reorientation. DWI's can be acquired with any desired sampling scheme. Diffusion tensors, FODs, or ODFs can also be reconstructed using any desired method and streamlines generated using any algorithm. Most importantly, it avoids the problem of generating tracts from reoriented diffusion tensors, FODs, or ODFs that are distorted relative to their native counterparts because the spatial warping is applied directly to the streamlines. Our results show that DSN has minimal influence on basic tractography measures such as tract count and structure and doesn’t significantly alter network metrics or topologic organization with only very small to small effect sizes. We have developed a universal framework in Python that works with most diffusion software platforms, algorithms, and ANTs for spatial normalization. It is publicly available at http://github.com/clintg6/DSN.

Chapter 3

Finding maximally disconnected subnetworks using shortest path tractography

Connectome-based lesion symptom mapping (CLSM) can be used to relate disruptions of brain network connectivity with clinical measures. We present a novel method that extends current CLSM approaches by introducing a fast reliable and accurate way for computing disconnectomes, i.e. identifying damaged or lesioned connections. We introduce a new algorithm that finds the maximally disconnected subgraph containing regions and region pairs with the greatest shared connectivity loss. After normalizing a stroke patient's segmented MRI lesion into template space, probability weighted structural connectivity matrices are constructed from shortest paths found in white matter voxel graphs of 210 subjects from the Human Connectome Project. Percent connectivity loss matrices are constructed by measuring the proportion of shortest-path probability weighted connections that are lost because of an intersection with the patient's lesion. Maximally disconnected subgraphs of the overall connectivity loss matrix are then derived using a computationally fast greedy algorithm that closely approximates the exact solution. We illustrate the approach in eleven stroke patients with hemiparesis by identifying expected disconnections of the corticospinal tract (CST) with cortical sensorimotor regions. Major disconnections are found in the thalamus, basal ganglia, and inferior parietal cortex. Moreover, the size of the

maximally disconnected subgraph quantifies the extent of cortical disconnection and strongly correlates with multiple clinical measures. The methods provide a fast, reliable approach for both visualizing and quantifying the disconnected portion of a patient's structural connectome based on their routine clinical MRI, without reliance on concomitant diffusion weighted imaging. The method can be extended to large databases of stroke patients, multiple sclerosis or other diseases causing focal white matter injuries helping to better characterize clinically relevant white matter lesions and to identify biomarkers for the recovery potential of individual patients.

3.1 Introduction

For over a century the relationship between lesion location and clinical deficits has been used to further our understanding of regional brain function and to predict neurological outcome, particularly after stroke (Damasio and Damasio, 1989 & Binkofski et al., 2001). Traditional voxel-based lesion symptom mapping (VLSM) has proved particularly useful in characterizing the functional specialization of discrete cortical regions (Fox, 2018). However, VLSM methods can be uninformative when symptoms are not clearly linked to the damage of a specific brain region or when the lesion extends into white matter, causing a concomitant disconnection of different cortical regions (Lim and Dong-wha, 2015). Since human cognition and behavior typically does not arise from a single brain region but rather results from emergent activity across neural networks via interconnected cortical regions (Geschwind, 1962 & Baldassarre et al., 2016), the potential of VLSM to accurately explain structure-function relationships remains limited. VLSM is not suitable to characterize white matter lesions in large part because it relies on T1 weighted images which biases it towards

detecting necrosis and gliosis in cortical tissue. This has led to methods that can take a network perspective that include white matter lesions (Carter et al., 2012). In particular, connectome-based lesion symptom mapping (CLSM) approaches are now integrating connectivity information based on functional or diffusion weighted imaging to improve the mapping between patient's lesions and symptoms (Yourganov et al., 2016 & Gleichgerrch et al., 2017). Although functional connectivity based CLSM approaches have proven their clinical utility for gray matter lesions, they are unable to provide connectivity information when a lesion is restricted to white matter because of a lack of meaningful BOLD signal in white matter. Several different strategies have been developed to perform CLSM based on structural data to investigate the clinical impact of disconnections of white matter pathways. Typically, the strategy is to project the patient's lesion into a normal database of streamlines to assess how approximated normative connectivity is disrupted by a lesion (Kuceyeski et al., 2013 & Thiebaut de Schotten et al., 2011). Similarly, predefined sets of white matter tracts in the normalized space can be used to compute their intersection with individual lesions. Disconnections are typically quantified by the proportional volume of white matter tract affected by the lesion, referred to as "lesion load" (Zhu et al., 2010). Instead of calculating the volume of the lesion within a given tract one can compute the proportion of streamlines that are severed by the lesion (Hope et al., 2016). There are a number of challenges with both strategies. Streamlines are a computational construct that is extremely sensitive to arbitrary parameter choices such as angle cutoff, step length and total number of streamlines generated, making it difficult to compare results (Wei et al., 2018). Furthermore, they are known to suffer from a hard tradeoff between the detection of true connections and the generation of excessive false connections, particularly for crossing fibers (Maier-Hein,

2017). Compounding the limits of this method, volumetric measures such as lesion load can be misleading because a major tract such as the corticospinal tract can be severed by a very small lesion in the posterior limb of the internal capsule resulting in a severe hemiparesis, yet a majority of its volume remains intact. Moreover, studies incorporating the alternative method: percent of tract loss, either quantify the lesion impact at the level of individual regions or simply provide a binary measure of whether the tract was severed (Kuceyeski et al., 2013 & Thiebaut de Schotten et al., 2011). Only recently, researchers have begun to quantify the relative amount of damage to a given fiber tract connecting region pairs. Using such an approach on DTI data in a large sample of patients, Langen and colleagues found that cognitive impairment was associated with disconnectivity, i.e., patients with higher percentages of damaged streamlines also suffered from pronounced cognitive impairment (Langen et al., 2018). While such quantitative analyses of streamline damage represent a promising approach, disconnectomes are typically constructed in the patients' native DTI space which can produce distorted disconnectomes because the diffusion information is corrupted in lesioned white matter tissue (Maillard et al., 2011; de Groot et al., 2013; Theaud et al., 2017). Tracking through regions where orientation maxima are distorted produces distorted connectomes and consequently distorted disconnectomes (Greene et al., 2018). To overcome this limitation, we here present a fast and accurate approach for estimating connectomes and disconnectomes that does not rely on streamline tractography and avoids tracking through lesioned white matter tissue. The approach embeds a patient's lesion, segmented from their standard clinical MRI data into a normative fiber orientation diffusion database. As such, the method allows one to assess disconnection without the need for adjunct diffusion imaging and therefore can be used in a standard clinical setting.

Accurately measuring disconnectomes at the region to region level with streamline based tractography is difficult if not impossible for many region pairs due to systematic biases in estimating long-range connections (Li et al., 2012; Sinke et al., 2018). As an alternative we construct connectivity matrices using whole brain shortest path tractography where region to region connectivity is weighted by shortest path probabilities. Specifically, we use data from the Human Connectome Project (HCP) to reconstruct each subject's fiber orientation distributions (FODs) using constrained spherical deconvolution and normalized them using FOD reorientation to a custom high-resolution template (Raffelt et al., 2012). For each HCP subject a white matter voxel graph is constructed in the template space using analytic tractography, which obviates the need for lengthy probabilistic tractography simulations (Cieslak et al., 2017). The output of analytic tractography at each white matter voxel is a 26-element vector containing the negative log of the probabilities that a white matter structure transitions into each of its neighboring voxels. White matter voxels located at the gray-white boundary are defined as interface nodes. These are partitioned into cortical regions using the Lausanne atlas. The shortest paths and their probabilities can be calculated for all pairs of interface nodes in different regions to capture region to region probability weighted structural connectivity. However, constructing shortest-path weighted structural networks from all pairings of the interface nodes is computationally costly because there are nearly 2,000,000,000 possible shortest paths per brain. To expedite these computations, we show that structural networks constructed from all possible pairs can be rapidly and almost perfectly estimated by uniformly sampling subsets of the interface nodes for a given region pair. After the anatomical scans from stroke patients are normalized into our template (along with their segmented lesion), the percent loss connectivity matrix or disconnectome can be

obtained by querying all shortest paths that intersect the lesion and by computing the proportion of shortest path probabilities that intersect with the lesion and hence can be assumed to be lost.

Given a particular patient's lesion size and location, the full disconnectome can be quite extensive, making visualization and clinical correlation challenging. With that in mind, we describe a new graph theoretic algorithm that quantifies the extent of cortical disconnection and reduces the dimensionality by extracting the maximally disconnected subgraph containing the regions with the greatest shared disconnectivity due to the lesion from the disconnectome or percent connectivity loss matrix. Although thresholding can be used to reduce the size of the disconnectome, it is an arbitrary edge based approach that produces subgraphs with no guarantee of shared disconnectivity due to a lesion. Our algorithm produces a clinically relevant disconnection subgraph that makes visualization tenable and produces a remarkably reliable estimate of the number of cortical regions ($k_{optimal}$) making up the disconnection subgraph.

3.2 Methods

3.2.1 Normal database

The S500 dataset was collected from the Washington University-Minnesota Consortium Human Connectome Project (Glasser et al., 2013). Further analysis was restricted to 210 subjects without familial relation. The data consisted of structural and diffusion scans corrected for geometric, eddy current, and motion distortions. The diffusion volumes were

collected with a spatial resolution 1.25×1.25×1.25 mm, using three shells at b = 1000, 2000, and 3000 s/mm2 with 90 diffusion directions per shell and 10 additional b0s per shell. High-resolution structural T1w and T2w volumes for each subject were acquired on the same scanner at 0.7mm isotropic resolution. Generalized fractional anisotropy (GFA) volumes for each subject were extracted from their generalized q-sampling imaging reconstructed HARDI data in DSI Studio (Yeh et al., 2010) for subsequent multimodal image registration.

3.2.2 Stroke database

Eleven stroke patients (mean age: 62.0 years ± 9.3 standard deviation; 9 male; 9 right-handed) suffering from a first-ever ischemic stroke causing a unilateral hand motor deficit were recruited from the University Hospital of Cologne, Department of Neurology. Inclusion criteria were: 1) age 40–90 years; 2) ischemic stroke as verified by diffusion-weighted magnetic resonance imaging (DWI); 3) unilateral hand motor deficit; 4) no other neurological disease.

Exclusion criteria were: 1) any contraindication to MRI (e.g., cardiac pacemaker); 2) infarcts in multiple territories; and 3) hemorrhagic stroke. This study was approved by the local ethics committee and all subjects provided informed written consent.

3.2.3 Multimodal template construction

Previously skull stripped, aligned, and distortion corrected T1w and T2w volumes were obtained for each subject and then rigidly registered to the subject's GFA volume. ANTs symmetric group wise normalization (SyGN) method was used to construct a custom multimodal population specific brain template from 40 HCP subjects chosen at random from

the larger dataset, using 5 iterations (Avants et al., 2010). All subjects were spatially normalized to this custom template using multimodal registration in ANTs. Freesurfer was used to segment grey matter from white matter and CSF and to build surfaces of the template brain (Dale et al., 1999). The Connectome mapper toolkit was used to parcellate the cortical regions based on the Lausanne 60 atlas (Daducci et al., 2012).

3.2.4 Diffusion reconstruction

The HARDI HCP datasets were reconstructed using constrained spherical deconvolution (CSD) with a maximum harmonic order of 8 (Tournier et al., 2007). The largest b-value shell was used during reconstruction. Using the software MRtrix, fiber orientation distributions (FODs) for each HCP subject were generated using CSD from their diffusion data (Tournier et al., 2012). The FODs were reoriented/warped to the multimodal template using apodized point spread functions based on the ANTs output from each subject's symmetric T1/T2/GFA diffeomorphic registration to the custom multi-modal template. Specifically, each FOD is decomposed into a series of weighted spherical harmonic PSFs. The amplitude of the negative lobes of the PSFs are reduced, then each PSF is reoriented using the local affine transformation estimated from the Jacobian of the total deformation field, and finally recombined into the full reoriented FOD (Raffelt et al., 2012).

3.2.5 Voxel graphs and shortest paths

White matter voxel graphs were constructed for each HCP subject using the double-ODF method in MITTENS (Cieslak et al., 2017). To do this, transition probabilities between each pair of adjacent voxels (whether a face, edge or corner) are calculated with a closed form analytic solution. Each voxel where the FOD is nonzero is treated as a node in a graph.

Edges are formed to each voxel's 26 spatial neighbors, weighted by the transition probabilities calculated by MITTENS i.e. the probability that a white matter structure from the source voxel continues into its neighbor. The voxel graph was restricted to only white matter voxels using a white matter mask from the multimodal template to restrict shortest paths from entering gray matter. The shortest path between any two voxels can be efficiently found using Dijkstra's algorithm. It corresponds to the path that maximizes the product of all the probabilities at each edge making up the path. The shortest path is assigned a weight by taking the geometric mean of the product of the probabilities for each edge making up the path.

$w_{path} = (\prod_{i=1}^{n} p_i)^{\frac{1}{n}}$, where n is the number of edges in the path (1)

3.2.6 Subsampling

The complete gray-white interface consists of 64,109 white matter voxels. To find a shortest path between every possible pair of these white matter voxels requires nearly 2,000,000,000 calls to the Dijkstra algorithm per subject. On a 120 compute node cluster, it takes ~24 hours to calculate all possible pairs of shortest paths, making this computation prohibitive for the full HCP dataset. To speed up the calculation of shortest path probabilities by orders of magnitude, we uniformly sample subsets of the interface voxel pairs.

Given cortical region A with m interface voxels and cortical region B with n interface voxels, there would be m×n shortest paths if each one was found for every possible pair which would be a lengthy computation typically involving tens of thousands of shortest paths. The computation can be significantly accelerated by employing a subsampling

approach where the larger region is uniformly sampled to obtain a subset of voxels such that the number of voxels in the subset matches the number of voxels in the smaller region. Each voxel in the larger region is paired uniquely to a voxel in the smaller region producing a total of min(m,n) source-target pairings and hence shortest paths. This is performed for each normal HCP subject for each cortical region pair to generate unique sets of shortest paths. The subsampling approach is illustrated in Figure 1. In the Appendix, we validate this approach by measuring the similarity between structural networks constructed from all possible pairs of shortest paths and the subsampled shortest paths. Our results in the Appendix show that subsampling is a fast and accurate approach for studying brain connectivity.

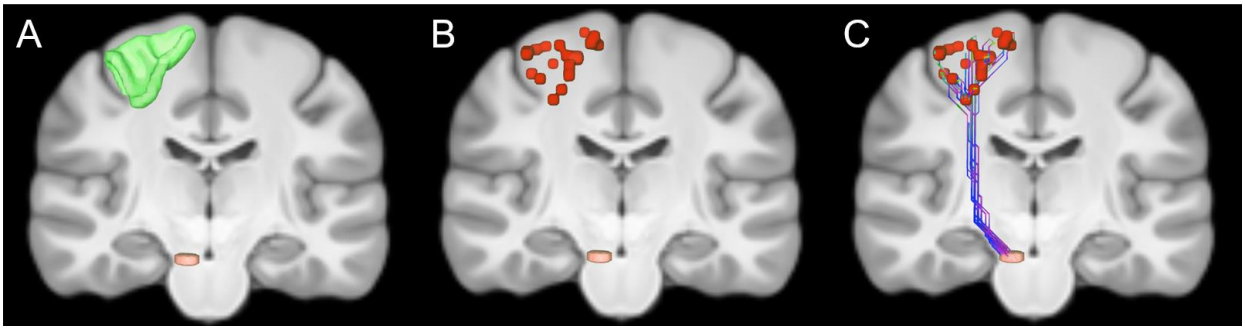

Figure 1: Illustration of subsampling. (A) The white matter surface of a portion of the left precentral region (green) containing 844 voxels is plotted with a portion of the brainstem (orange) containing 30 voxels. If all possible pairs of shortest paths were found between the regions there would be (844 × 30) = 25,320 shortest paths which would be a lengthy computation. The computation can be significantly sped up by employing a subsampling approach where the larger region is uniformly sampled to obtain a subset of voxels such that the number of voxels in the subset matches the number of voxels in the smaller region. (B) 30 voxels subsampled from the larger precentral region are plotted in red. Every voxel in the subset is uniquely paired to a voxel in the smaller region, producing here 30 unique source-target pairings for shortest paths queries. (C) The 30 shortest paths found between voxels in the brainstem and precentral area trace out the CST. This procedure is performed for each normal HCP subject to generate unique sets of pairings and shortest paths for any given cortical region pair.

3.2.7 Connectome and connectivity loss

The Lausanne60 cortical parcellation was projected onto white matter voxels lying at the gray white interface. Note the method is flexible and any cortical parcellation could be projected. A shortest path probability weighted structural connectome is then constructed by computing the shortest path from every uniformly sampled subset of interface voxel pairs in different cortical regions for each HCP subject. To compute the percent loss of connectivity, L, for a cortical region pair, the cumulative weight of the shortest paths that intersect the lesion, W_{in}, is divided by W_{total}, the cumulative weight of all shortest paths between the two regions to obtain the weighted fraction of potentially damaged shortest path connections. All weights are estimated using (1).

$$L = \frac{W_{in}}{W_{total}} \tag{2}$$

The connectivity loss matrix L_{stroke} for a given stroke patient is taken as the average of all the loss matrices L calculated using each HCP subject's shortest paths (as defined by that stroke patient's lesion). The procedure for calculating the connectivity loss matrix L_{stroke} is summarized in Figure 2.

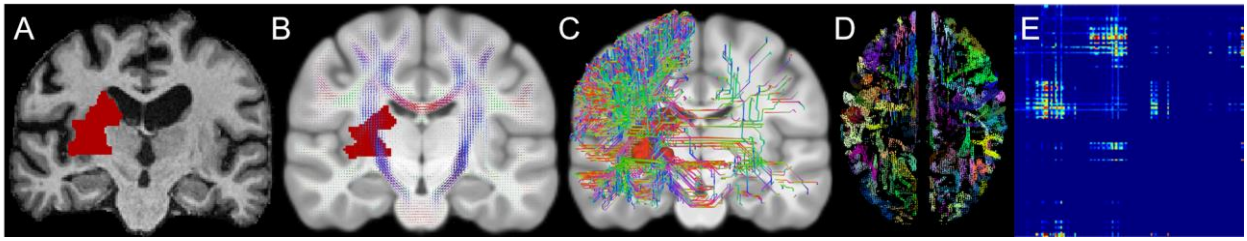

Figure 2: Schematic of patient disconnectome construction. (A) Lesioned tissue (red) is segmented on the patients' T1 weighted volume and (B) normalized into our high resolution T1 weighted template. (C) Shortest paths that intersect the patients' normalized lesion are found. (D) Region labels are then assigned to the end points of each of the shortest paths. For each shortest path making up a region pair, the probability of that shortest path is calculated and added to the running total of connective probability lost due to the lesion for that region pair. (E) The disconnectome is then computed as the fraction of connective probability loss relative to the total connectivity probability shared for any given region pair. (C)—(E) are performed 210 times for each set of shortest paths from each of the normal HCP subjects. The final connectivity loss matrix, L_{stroke}, is taken as the average of the 210 disconnectomes.

3.2.8 Maximally disconnected subgraphs

In graph theory, this problem is most similar to the heaviest k-subgraph problem where an undirected weighted graph is given, and the goal is to find a subgraph with k nodes with maximum total edge weight. This problem is NP-hard but can be well approximated using a greedy approach (Ravi et al., 1994). Given a disconnectome, such an algorithm would extract a subgraph of k nodes whose edges have the greatest disconnection. In our algorithm, we use a greedy approach similar to (Ravi et al., 1994) and extend it by automatically finding an optimal number of nodes, $k_{optimal}$, to grow the heaviest subgraph. The growth profile of the magnitude of the change in the weight of the subgraph for each kth node added has concave shape with a clearly defined maximum. The magnitude at the maximum and the numbers nodes k it occurs at we define as $\Delta W_{optimal}$ and $k_{optimal}$.

To find the maximally disconnected subgraph D_{max}, the following approach is used. The disconnected subgraph D is initialized with the nodes from the heaviest edge e_{max}, from the connectivity loss matrix L. In the case of a tie, the nodes in the edge containing the greatest cumulative sum of weighted node degree are added. Each iteration k subsequently chooses a new node, $n_{max} \in L - D_{k-1}$, to add to the subgraph such that the sum of the edge weights to the nodes currently in D_{k-1} is maximized. The change in the weight ΔW_k (from D_{k-1} to D_k) is stored in P, the disconnection profile, and D_k is stored in S for each iteration. D is grown until all nodes and edges from L have been added. After D is finished growing, a cubic spline is fit to the disconnection profile in P to find $k_{optimal}$ and D_{max} is returned from the $k_{optimal}$ element in S. The procedure is summarized in Algorithm 1, where W_{pre} is the weight of the subgraph at D_{k-1} at the k−1 iteration and W_{post} is the weight of the subgraph at D_k at the kth iteration,

$w\left(n_{i_{L-D}}, n_{j_D}\right)$ is the weight of the edge between node i and node j, and e_i is edge i in the subgraph D.

***Algorithm* 1**. *Maximally disconnected subgraph*

1: $Input: loss\ matrix$ L

2: $Output: maximally\ disconnected\ subgraph\ D$

3: $D \leftarrow \emptyset$

4: $P \leftarrow \emptyset$

5: $S \leftarrow \emptyset$

6: $Let\ e_{max}\ \{n_i, n_j\}\ be\ a\ max\ weight\ edge\ in\ L$

7: $D \leftarrow\ e_{max}$

8: $while(|D| < |L|)$:

9: $\underset{n_{max} \in L-D}{argmax}\ \sum_{i=1}^{|L-D|} \sum_{j=1}^{|D|} w\left(n_{i_{L-D}}, n_{j_D}\right)$

10: $W_{pre} = \sum_{i=1}^{N_{edges}} w(e_i),\ e_i \in D_{k-1}$

11: $for\ i = 1, \ldots, |D_{k-1}|$:

12: $D_k \leftarrow\ D_{k-1} \cup e_j\ =\ \{n_j, n_{max}\}$

13: $W_{post} = \sum_{i=1}^{N_{edges}} w(e_i),\ e_i \in D_k$

14: $\Delta W = W_{post} - W_{pre}$

15: $P\ \leftarrow \Delta W$

16: $S\ \leftarrow D_k$

17: $P_{spline}\ \leftarrow fit\ P\ with\ cubic\ spline$

18: $return\ D_{k^*} \exists\ k^*\ =\ \underset{k}{argmax}\ P_{spline}$

In the appendix, we demonstrate that the greedy algorithm for identifying the maximally disconnected subgraph closely approximates the exact solution. Specifically, the correlation between the change in the weight of the subgraphs for each method has an R^2 of 0.99. Although this doesn't represent the similarity of the set of nodes in the subgraphs at each iteration of k, it shows that our algorithm is accurately approximating the k-heaviest subgraph. More specifically, in the appendix we show that the dice score for each iteration of k initially shows poor agreement between the exact solution and our greedy one because there is minor disagreement initially about what node should be added to make the subgraph as heavy as possible i.e. most disconnected. As k increases the greedy solution agrees perfectly with the exact one with dice scores of 1.0. Moreover, our greedy algorithm is rapid, taking only seconds to find the maximally disconnected subgraph versus weeks to find the exact solution (combinatorial).

3.2.9 Disconnection growth profiles

To determine the optimal size of a disconnection subgraph for a given lesion, a population estimate from the HCP dataset is performed. To do this the change in the magnitude of each patient's subgraph as each node k is added from each of their connectivity loss matrix is determined first. These 210 growth profiles are then averaged and fit with a smooth cubic spline to get a robust global estimate of $k_{optimal}$ because estimates from single HCP subjects can be noisy and the average has minor perturbations near the peak. The $k_{optimal,}$ determined from the averaged disconnection growth profiles, is then applied to the mean of the 210 HCP connectivity loss matrices to extract the final maximally disconnected subgraph. This process is performed separately for each patient's lesion. In the Appendix, we demonstrate that these growth profiles and maximally disconnected subgraphs are the

same for shortest path measures across all gray-white matter interface nodes and for the computationally faster subsampled set of interface nodes.

3.2.10 Reliability

To measure the reliability of $k_{optimal}$, the mean and its uncertainty are estimated by bootstrapping. Each sampling distribution of $k_{optimal}$ is constructed by randomly sampling with replacement N disconnection profiles 10,000 times where N ranges between 2 to 209 subjects. For each bootstrap sample in each distribution, the disconnection profiles are averaged and the sample $k_{optimal}$ is recorded from the cubic spline fit. For each sample distribution, the standard deviation and mean of the sample $k_{optimal}$ are recorded.

3.3 Results

3.3.1 Connectivity loss

The S500 dataset was Our method creates a normative database of connection probabilities, based on shortest paths between all region pairs for a given atlas. In this case, there are 130 regions in the Lausanne60 atlas for 210 normal HCP subjects. Then, a spatially normalized lesion from an individual stroke patient is projected into this database and the percentage reduction, i.e. loss of connection for each region pair is calculated. Examples of the connectivity loss matrix for two stroke patients (P1, P2) are shown in the left column of Figure 3. Each of the plotted connectivity loss matrices represents a mean of the 210 individual connectivity loss matrices defined by intersecting the stroke patient's lesion with

each of the HCP subjects subsampled shortest paths. For both patients shown in Figure 3, the lesions involve the posterior limb of internal capsule and adjacent thalamus. Not surprisingly, the two loss matrices have obvious structural similarity, yet each contains additional specific disconnections unique to each patient's lesion. Note the large variability in the magnitude of disconnection of individual connections, with some region pairs having 100% disconnection (dark red) while other region-pair connections remaining untouched by the lesion (dark blue), demonstrating the sensitivity of the % loss metric.

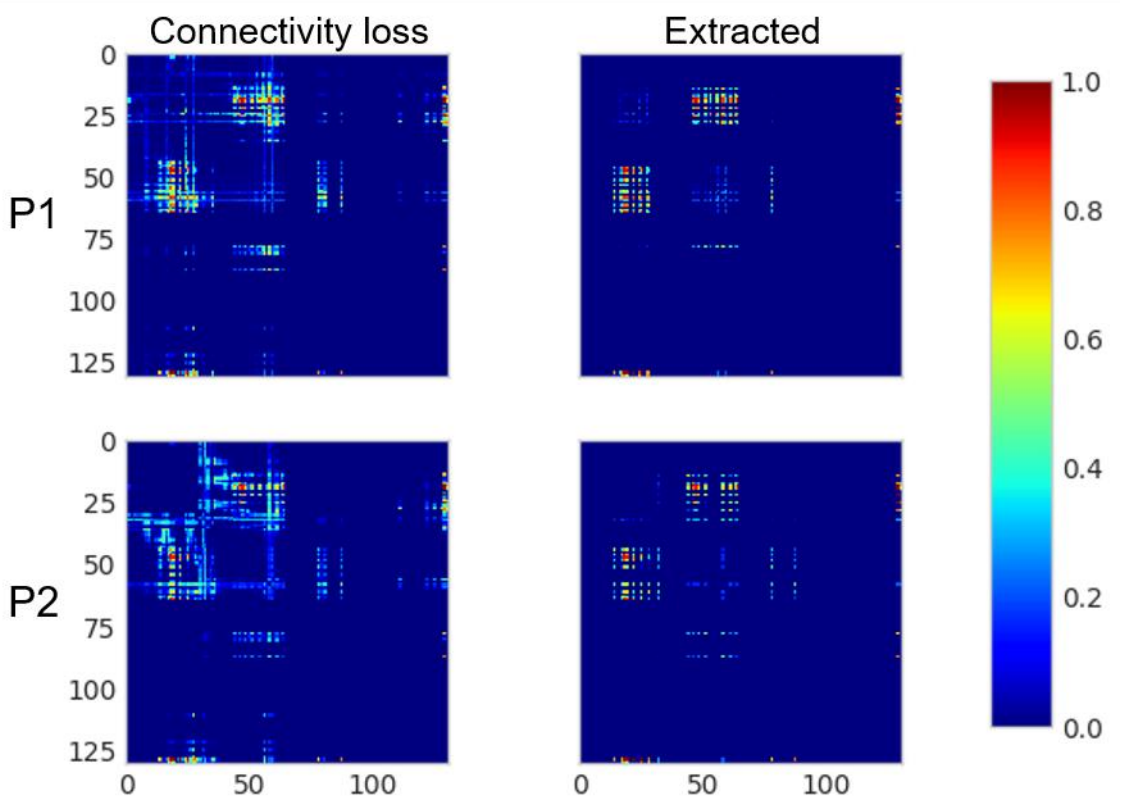

Figure 3: Quantitative metrics of structural disconnection. A disconnectome (Connectivity loss, left column) is shown for two patients (P1, P2). Connections in dark red exhibit 100% connectivity loss. Regions connections in dark blue were not impacted by the lesion. The set of connections extracted by our algorithm from the disconnectome forms the maximally disconnected subgraph (Extracted, right column). It consists of those connections between regions that exhibit a larger proportion of connectivity loss due to the lesion. Both patients have posterior limb-internal capsule lesions and remarkably similar disconnection subgraphs.

3.3.2 Optimal k and the Maximal disconnection subgraph

Connectivity loss matrices from each of the 210 HCP subjects, (whose averages for two patients are as shown in the left column of Figure 3) are entered into our greedy algorithm to extract a set of maximally disconnected subgraphs (extracted set of connections shown in the right column of Figure 3). Constructing this k-heaviest subgraph is a well-defined problem given the parameter k of how many nodes the subgraph should contain. However, it's not clear which k is optimal to stop growing the heaviest subgraph. In the left panel of Figure 4, we plot the cubic spline fit of the magnitude of the change in the total edge weight of the subgraphs for the two patients as functions of each node k that is added in solid along with the average in dots. This plot is generated from the mean of individual growth profiles obtained across all 210 HCP connectivity loss matrices. Thus, it reflects an average of the change in the total edge weight estimated for each disconnection subgraph of the 210 HCP subjects. This is done separately for each patient. As shown in Figure 4 (demarcated with a +) the magnitude of the change in the total edge weight grows with k until reaching its maximum at $k_{optimal}$ and then falls off slowly as additional nodes are added to the subgraph. This concave disconnection growth profile is present in all patients. Consequently, the peak of the disconnection growth profile lends itself as a natural stopping criterion and defines $k_{optimal}$. For the first (P1, red) it peaks later at k = 27 compared to the second (P2, blue) at k = 24. The spline fit is necessary to ensure that the global maxima are selected because there can be minor perturbations that lead to local maxima being selected. This is most visible for Patient 2's raw average plotted as the blue dotted line with minute perturbations on the left and right of the global maximum (blue cross) that are slightly higher. In the middle panel, we assess the reliability of $k_{optimal}$ by bootstrapping 10,000 randomly sampled disconnection

profiles from N subjects. As the number of subjects N used to estimate $k_{optimal}$ increases, the deviation (shaded) around the sample mean decreases exponentially until plateauing. The deviation around P1's mean drops quicker than P2's. For both patients, the error converges to a deviation of ≤ 1 of the $k_{optimal}$ estimated from the mean of 210 subjects with 100 or more subjects. Mean deviation from the sample mean for N = 105 subjects across all 11 patients in the bootstrap with is 0.66 with $\sigma = 0.38$. The two patients' normalized lesions are plotted onto our custom HCP template brain (with average FODs also shown) on the right panel of Figure 4. Both stroke patients' lesions on the right in Figure 4 were roughly the same size containing 592 and 586 voxels respectively and both were in the right hemisphere. Patient P1's lesion (red) extends beyond the posterior limb of the internal capsule, incorporating voxels with FODs describing connectivity in additional directions besides the capsule. In contrast, Patient P2's lesion is located almost entirely within the poster limb of the internal capsule. This subtle difference in lesion shape has a direct impact on the disconnectome and is captured by the larger $k_{optimal}$ for the first patient.

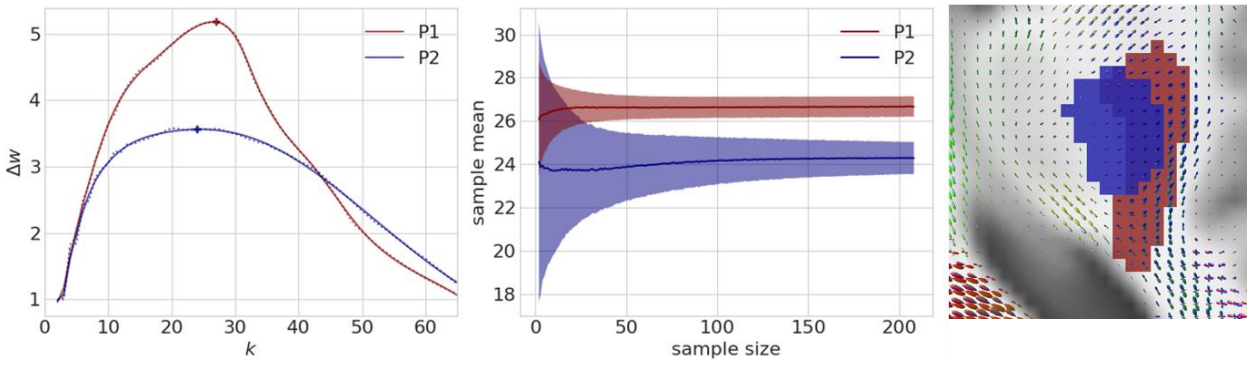

Figure 4**:** An algorithm to grow a maximal disconnection subgraph. On the left panel the average magnitude of the change in the total edge weight of the subgraph as it grows in the number of nodes k from 210 HCP subjects. In both patients a clear concave disconnection growth profile emerges, where initially the magnitude of the change grows rapidly until reaching the peak at $k_{optimal}$. Patient 1 peaks at k = 27 (red cross) and patient 2 peaks at k = 24 (blue cross). After the peak, the change in total edge weight slowly drops off as additional nodes are added to the subgraph. In the middle panel, the reliability of $k_{optimal}$ is estimated. The standard deviation (shaded) around the mean drops exponentially as the number of subjects increases. P1's deviation curve drops quicker than P2's. With 100 or more subjects the sample mean converges with a standard deviation ≤ 1 of the $k_{optimal}$ estimated from 210 subjects. On the right the two patients normalized lesions are plotted on top of the HCP template brain (with average FODs). While both patient's lesions are nearly identical

in size and in the right hemisphere, the profile for the first patient (red) peaks higher than the second blue) because their lesion extends across a more complex set of local diffusion directions.

3.3.3 Maximally disconnected subgraphs

Our algorithm automatically determines a unique $k_{optimal}$ for each patient and returns the maximally disconnected subgraph. In Figure 5, the extracted maximally disconnected subnetworks are plotted on top of the glass brain along with their corresponding maximally disconnected matrices (Abraham et al., 2014). Region ROIs are plotted as circles with the diameter reflecting the weighted degree of that region's total percent connectivity loss. Edge thickness and color represent percent connectivity loss between the connecting nodes, where the darker the color and thicker the line the more disconnected the two regions. For the first patient, major disconnections are found amongst pairs of precentral, postcentral, brainstem, pallidum, and temporal cortex. Similarly, in the second patient, precentral, postcentral, brainstem, pallidum, and thalamus comprise the most disconnected regions and region pairs. Both patients maximally disconnected subnetworks are mostly restricted to cortical regions in the right hemisphere, matching the hemisphere where the stroke occurred and demonstrating the specificity of our approach.

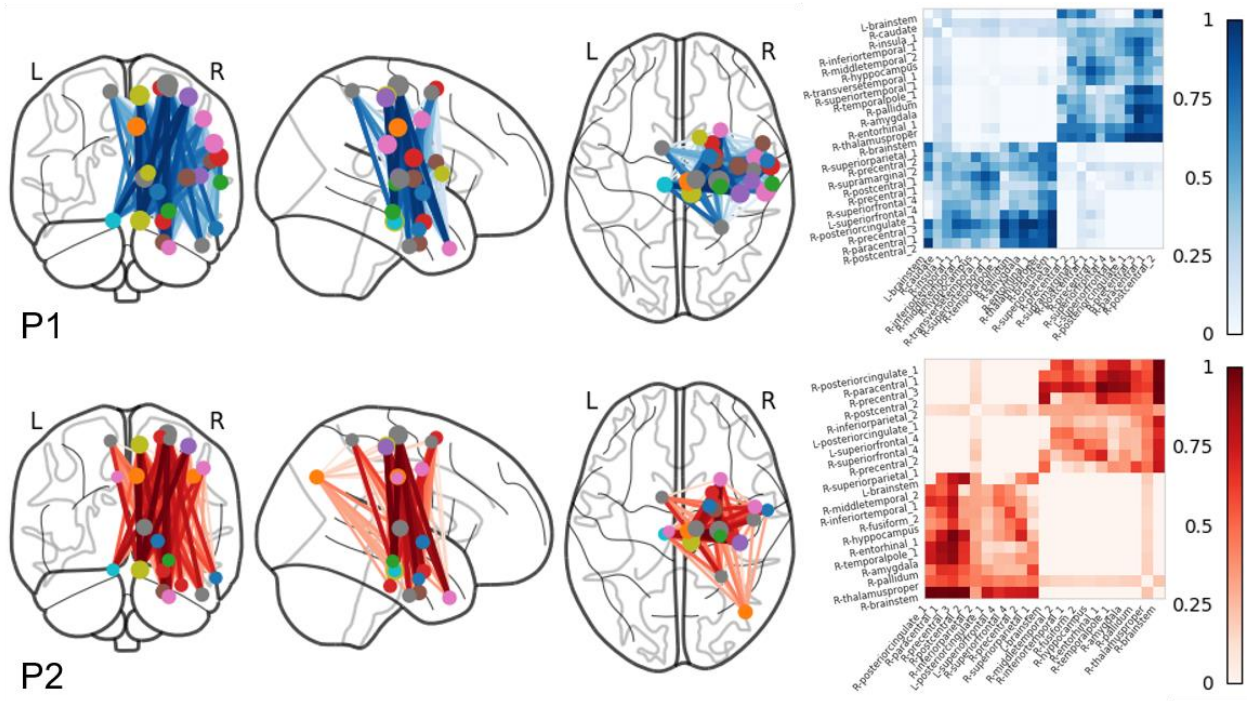

Figure 5: Maximally disconnected subnetworks plotted on top of the glass brain along with the corresponding maximal disconnection matrices. Region ROIs are plotted as circles with the diameter reflecting the weighted degree of percent connectivity loss. The thicker the edge and the darker the color the greater the percent connectivity loss between the connecting regions. Major connectivity loss was found amongst pairs of precentral, postcentral, brainstem, pallidum, and thalamus in both patients (P1, P2). Most of the patients' identified disconnected regions are in the right hemisphere where the lesion occurred.

3.3.4 Disconnected core

Just as it is possible to identify maximal lesion overlap from structural MRI scans to find regions that are most commonly impacted in a cohort of patients, it is also possible to identify a core pattern of disconnection across overlapping subgraphs. To demonstrate this, consider the disconnected networks of both stroke patients in Figure 5. It is evident that many of same regions and pairs are disconnected. By intersecting the two maximally disconnected subgraphs, we can visualize the disconnected core network from stroke lesions that result in hemiparesis. In Figure 6, the maximally disconnected core sits on top of the right motor network and is dominated by disconnections amongst motor regions: precentral,

postcentral, superiorfrontal, brainstem, thalamus, pallidum, and caudate. The weight of the edges making up the core were found by averaging the edge weights of the two patients.

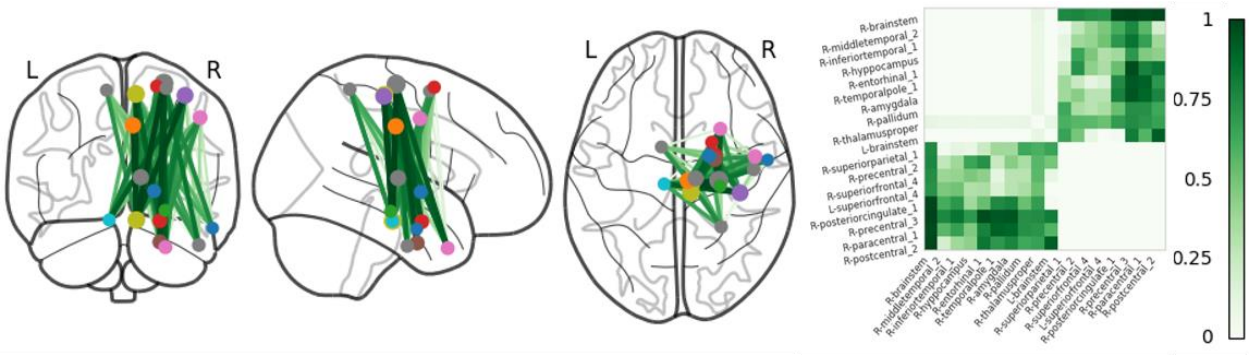

Figure 6: The disconnected core network is found by intersecting the two maximally disconnected subgraphs of the two stroke patients. The core is primarily comprised of brain regions in the right hemisphere involved in motor function with large percentages of connectivity loss amongst precentral, postcentral, superiorfrontal, brainstem, thalamus, and pallidum. Edge weights were taken as the average between the two patients for a given edge. This overlap in sensorimotor circuits is consistent with the fact that the patients were both selected because of similar clinical features of hemiparesis.

3.3.5 Dimensionality reduction

Our algorithm reduces the dimensionality of the connectivity loss matrix from N × N to $k_{optimal} \times k_{optimal}$. The size reduction is evident in comparing the top and bottom panels of Figure 7. In the top panel, patient 3's full connectivity loss matrix is plotted on top of the glass brain. Note that the full disconnectome is dominated by a majority of small percent losses (blue) of connectivity for many region pairs with a small set of connections showing large percent losses (orange—red). In the bottom panel, the set of cortical regions and connections making up the maximally disconnected subgraph are plotted on the glass brain. Our algorithm filters out most connections and cortical regions that have small losses and are not likely disconnected (blue) and preserves the cortical regions and connections that share the greatest connectivity loss due to the lesion (orange—red). Also note that patient

3's lesion is in the right hemisphere and that most of the nodes and connections filtered from the disconnectome are in the left hemisphere and that the preserved connections tend to cluster around the lesion.

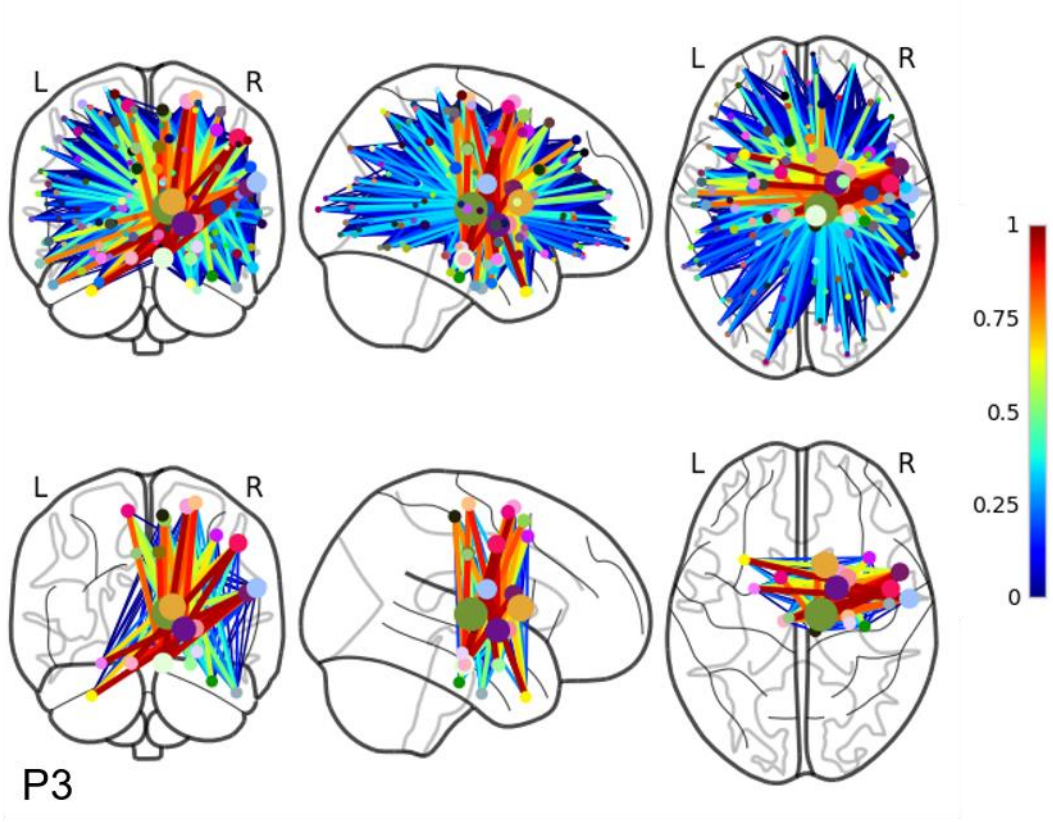

Figure 7**:** The full connectivity loss matrix plotted on the glass brain in the top panel. Many of the connections between cortical regions have a small loss in connectivity (blue) with only a small subset having a large or complete loss connectivity loss (orange—red). Our algorithm extracts the maximally disconnected subgraph filtering out connections and cortical regions with small losses of connectivity. The set of connections and cortical regions experiencing large shared connectivity losses are plotted in the bottom panel on the glass brain. Most of these remaining connections are in the right hemisphere and cluster around the lesion.

3.3.6 Location effects

To further demonstrate the interplay between lesion location, the maximum of the magnitude of the change in the total edge weight of the subgraph, and $k_{optimal}$, lesions of identical size are simulated in multiple locations for single fiber populations and a crossing fiber population in central and peripheral regions of the brain. The magnitude of the change

in total edge weight of the subgraph as it grows to k nodes is plotted on the left in Figure 8 for each lesion. The corresponding lesions are plotted on the template brain on the right. ROI 1 and ROI 3 are both comprised of single population fibers while ROI 2 contains multiple fiber populations where ROI 1 occurs centrally in the poster limb of the internal capsule and ROI 3 occurs peripherally near cortex. ROI 1 has the same profile as seen in the patients' lesions in Figure 4 while ROI 2 and ROI 3 do not rapidly rise or drop off in the magnitude of the change in total edge weight. ROI 1 has a much larger peak and $k_{optimal}$. ROI 2 and ROI 3 both have much smaller peaks and occur earlier.

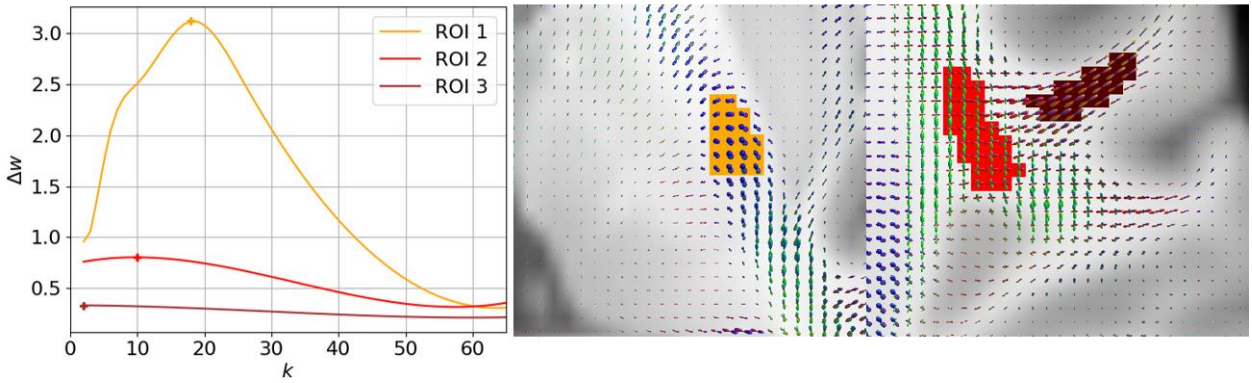

Figure 8**:** The impact of lesion location on subgraph size. On the left the magnitude of the change in the total edge weight of the subgraph as it grows in the number of nodes k is plotted for each simulated lesion. On the right, are the corresponding simulated lesion ROIs plotted on our HCP template brain. All the ROIs are 74 voxels in size. ROI 1 has an identical profile to the curves in Figure 4 from patients' lesions and peaks at k = 18 (orange cross). ROI 2 and ROI 3 do not rise rapidly but slowly drop off in total edge weight once they reach their peaks at k = 10 (red cross) and k = 2 (brown cross) respectively. ROI 1 and ROI 3 are comprised of single population fibers while ROI 2 is comprised of a crossing fiber population.

3.3.7 Relation to clinical measures

As a simple demonstration of the potential utility of $k_{optimal}$ (the size of the maximally disconnected subgraph) as a metric with clinical use, we correlated it with several standardized assessments of eleven stroke patients' clinical status on hospital admission. We tested both the NIH Stroke Score, an overall measure of functional status and a more

specific measure, the patient's relative grip strength denoted as the maximum grip strength of the paretic hand relative to the maximum grip strength of the unaffected hand. As has been shown previously, overall lesion size correlated with the patients' overall functional status as measured by the NIHSS (Table 1). Similarly, $k_{optimal}$ showed a strong and significant correlation with the overall functional status. The more specific functional measure of relative grip strength, demonstrated no correlation with lesion size, a well-known and intuitive result given that very large lesions, while causing many global deficits can spare motor function if the corticospinal tract is uninvolved whereas a very small lesion of the internal capsule can lead to major motor deficits. Our measure of maximally disconnected subgraph size captures this important distinction. We find that grip strength has a strong inverse correlation (R = -0.62) with $k_{optimal}$.

	NIHSS admission		**Relative grip strength**	
	R	*p-value*	*R*	*p-value*
Lesion size	0.63	0.038	-0.009	0.98
Subgraph size	0.63	0.039	-0.62	0.040

Table 1: Spearman correlation of disconnected subgraph size and lesion size to clinical stroke measures. Lesion size and disconnected subgraph size show an identical relation with initial NIHSS admission score. However, lesion size has no correlation with relative grip strength while disconnected subgraph size shows a strong inverse correlation of -0.62.

3.4 Discussion

We present a set of fast and accurate approaches for estimating the overall connectivity loss matrix and maximally disconnected subgraph using shortest path tractography in white matter voxel graphs. There are multiple potential benefits of using a white matter voxel

graph to construct a connectivity matrix based on shortest paths compared to streamline based measures. First, Dijkstra's shortest path algorithm is guaranteed to find a path between voxels in different regions no matter their spatial distance. Secondly, the paths connecting two regions are weighted by the geometric means of the edge probabilities instead of each being treated as equally likely as is typically done with streamline counts. Consequently, shortest path estimations have high sensitivity and can capture small reductions of connectivity between many pairs of regions which is evident in Figure 3, providing unique disconnection information even when lesions are similar in size and location. For connectivity matrices constructed with streamline tractography, many region pairs that should be connected appear disconnected due to length and crossing fiber effects that ultimately lead to premature streamline termination and attempts to overcome this by growing more streamlines leads to many false connections or by dilating gray matter region labels deeper into white matter leads to inaccurate streamline labelling. Although weights can be generated for streamlines using approaches such as SIFT2 or COMMIT for either pruning false streamlines or creating weighted connectivity loss matrices, they do not address the length and crossing fiber effects that lead to many disconnected region pairs that should be connected (Smith et al., 2015 & Daducci et al., 2015). Consequently, the accurate estimation of the true underlying disconnectome or percent connectivity loss remains difficult with streamline approaches. A disadvantage of our shortest path approach is that it also contains many false positive connections as with streamline tractography. However, it's guaranteed to contain all the true positive connections as well which streamline approaches cannot guarantee. Although not investigated here, the weights of each shortest path could be used for pruning out false positive paths and approaches such as COMMIT and LiFE could

also be integrated for pruning false positive paths (Daducci et al., 2015 & Pestilli et al., 2014). Moreover, shortest path measures are computationally costly: calculating 2-billion+ shortest path connections between all voxels at the gray-white matter interface per brain can be impractical. We therefore introduce a key strategy to overcome this computational burden: subsets of interface nodes are uniformly sampled at the gray-white interface. In the Appendix we show that the construction of shortest path probability weighted structural networks can be estimated accurately and quickly by only finding shortest paths from uniformly sampled sets of gray-white interface voxels. The subsampled structural network has a Pearson R-score of 0.99 with its full counterpart. With this, the task of computing shortest paths decreases from ~24 hours to minutes per subject.

With this accelerated estimate of shortest paths, it becomes practical to derive weighted estimates of the % loss of connectivity across all regions pairs when a patient's lesion is projected into a diffusion data set obtained from a healthy brain at high spatial and angular resolution. To make this robust at the population level, it is straightforward to take the same lesion and project it into many normal diffusion data sets. Here, we used 210 of the normal unrelated HCP adult subjects and find that our results with them provide remarkably consistent and clinically plausible maps of disconnection. A decided advantage of this approach is that a weighted matrix of lost connections over the entire brain can be readily generated for individual patients, without the need for a lengthy and clinically impractical diffusion tensor scan from the same patient. All that is needed is a reliable segmentation of the patient's lesion, obtained from routine clinical MRI. It is important to note that our approach is not suitable for patients if white matter reorganization is suspected. Likewise, our approach is not suitable in longitudinal studies.

A second major goal of our work was to develop an algorithm that could consistently reduce the size of the overall connectivity loss matrix because visualizing the full disconnectome is cumbersome and can be difficult to interpret. Rather than a simple arbitrary threshold approach, we developed an algorithm that quantifies the extent of the cortical disconnection network and extracts the most disconnected set of connections and cortical regions from the connectivity loss matrix, i.e., the disconnectome input that share disconnectivity. This is illustrated in Figure 7 where the full disconnectome in the top panel containing a majority of connections with small losses in connectivity is entered into our algorithm where primarily regions and connections experiencing a large percent connectivity loss are extracted to form the maximally disconnected subgraph in the bottom panel. To do this, we extended the k-heaviest subgraph problem by defining an optimal number of nodes, $k_{optimal}$, to grow the heaviest subgraph. As shown in the results, the growth profiles of the magnitude of the change in the weight of the subgraph for each kth node that is added have concave shapes with clearly defined maximums. We define the subgraph where the maximum occurs as the maximally disconnected subgraph. The maximally disconnected subgraph is typically not a maximally disconnected clique because our algorithm does not require every node to be adjacent. This requirement is relaxed because enforcing every node to be a neighbor inherently overrides the goal of extracting the heaviest subgraph because a clique of k nodes is not guaranteed to be the k-heaviest subgraph. $k_{optimal}$ can be robustly estimated from 100 or more subjects for patients with a standard deviation ≤ 1. Here too, there is a significant computational cost to estimating maximally disconnected subgraphs. This motivated our introduction of a greedy algorithm

to accelerate this process. In the appendix, we demonstrate that our greedy algorithm closely estimates the full approach (R = 0.99).

Neurobiologically, the set of nodes in the disconnected subgraphs up to $k_{optimal}$ share the cumulative greatest loss in connectivity due to the lesion to each other. The maximally disconnected subgraph finds the set of brain regions that are maximally disconnected from each other due to a lesion. After $k_{optimal}$, further nodes added do not share as great of a connectivity loss due to the lesion to all the other regions present in the disconnected subgraph. In our results, we focus the use of our algorithm on individual patients, rather than large sample averages to make it evident that our algorithm is specifically extracting just those cortical regions and connections between them with a shared large connectivity loss. Moreover, with the results from our simulated lesions it becomes clear that the maximum number of nodes k can change dramatically as a function of small shifts in lesion location, independent of lesion size. This is governed by how many unique connections pass through a given location and how many connections for a given pair intersect it. Once a maximally disconnected subgraph is generated, the impact on an individual patient can be readily visualized and direct clinical correlation becomes feasible. For example, the disconnection subgraphs shown in Figure 5 sit on top of known motor regions: precentral, postcentral, brainstem, pallidum, and thalamus, consistent with the primary clinical deficit in patients 1 and 2: unilateral hemiparesis.

In parallel, disconnection subgraphs from many patients can be used for correlation with clinical signs (as we demonstrate with grip strength measures) or intersected to find common underlying structural abnormalities for a population with similar deficits. For example, the core disconnection of motor regions and corticospinal tract shown in Figure 6 is not

surprising given the selection of patients with hemiparesis. Although $k_{optimal}$ correlates with the relative grip strength of stroke patients while lesion size doesn't, $k_{optimal}$ is not specific to the motor network. It is possible for patients to have a high $k_{optimal}$ without a grip strength deficit. Because the subset of patients used in our study have motor deficits, $k_{optimal}$ correlated with the relative grip strength. Consequently, $k_{optimal}$ should only be used for correlation on patients with similar deficits.

Most disconnection studies do not assume a linear association between the number of affected tracts and functioning, because the number of tracts varies considerably as a function of the region pair size and algorithmic parameters that may differ considerably between different analyses and thus yield highly variable results. Consequently, the number of tracts is not a functionally meaningful metric. Instead, the relative loss of tracts between pairs of regions or relative regional loss or relative tract volume lost are assessed. For such relative estimates, one may expect that higher percentages of connections lost due to intersecting a larger lesion, will results in more sever functional impairments with less remaining intact tracts being able to functionally compensate the white matter damage.

While the impact of discrete lesions on the connectivity of multiple critical white matter pathways on complex behavior has been shown previously, this has largely been accomplished by mapping local predefined sets of white matter tracts with streamlines (Rusconi et al., 2009). Preselection of tracts always introduces a bias and there is potential to miss important disconnections that are outside of this predefined search space that could be treatment targets.

Disconnection can also be quantified without preselecting sets of tracts. However, prior studies that avoided preselection have had marked methodological disadvantages. For

example, Kuceyeski et al., 2013 only quantified the percent disconnection at the region level which doesn't elucidate what additional regions that region is disconnected from. Although Langen et al., 2018, measured the percentage of disconnection at the region-to-region level, they used DTI and tracked through lesion tissue with distorted tensor orientations. Performing streamline tractography on distorted diffusion information is known to accumulate into large errors which accumulate into connectomes and consequently disconnectomes (Greene et al., 2018).

In summary our method provides a fast, accurate, robust and unbiased approach for studying the impact of lesions and location on the entire connectome that does not rely on streamline tractography and avoids tracking through lesioned white matter tissue. All that is required is a well segmented lesion. Moreover, it makes visualization and clinical correlation of the disconnection tenable and feasible. Using the provided methodology on a large dataset of behaviorally well-characterized stroke patients in the future may help to further our functional understanding of specific aspects of the structural connectome. Similarly, our approach may help to identify aspects of connectivity indicative of the potential for recovery on the level of individual patients to individualize therapy and improve outcome in stroke patients in the future. Our software package for performing shortest path tractography, constructing connectomes and disconnectomes, and finding maximally disconnected subgraphs can be found online at http://github.com/clintg6/ShortestPathTools.

Chapter 4

Optimal Fiber Diffusion Model Restoration

Assessing the effects of white matter (WM) lesions on structural connectivity as measured by diffusion MRI (dMRI) is invaluable for understanding structure-function relationships. These WM lesions have many etiologies that ultimately lead to attenuation of the anisotropic signature in dMRI signals. Attenuation can produce inaccurate reconstructions of the underlying model of the fiber population. In this paper, we combine methods from image inpainting and estimation theory to develop a novel approach for restoring the fiber model in small to moderate sized WM lesions. Our approach begins by taking healthy reconstructed WM fiber models at the boundary of the lesion and filling in lesioned voxels with their optimal affine estimate moving iteratively in a fast-marching method style until the fiber models in the lesion are restored. We demonstrate with in-vivo simulations on diffusion tensors (DTs) and fiber orientation distributions (FODs) that our approach offers superior performance over multiple restoration approaches. We restore lesioned fiber models in three stroke patients suffering hemiparesis from damaged corticospinal tracts (CST). We show that our method restores diffusivities, anisotropy and orientation of lesioned DTs as well as the amplitudes and orientations of fiber populations in lesioned FODs enhancing

tractography and enabling more accurate characterization of lesion connectivity and changes in tissue microstructure in patient populations.

4.1 Introduction

Diffusion-weighted magnetic resonance imaging (DW-MRI) techniques have been successfully used to non-invasively explore fiber bundle architectures in the brain. These techniques are sensitive to the diffusion of water molecules enabling the characterization of the orientation of bundles of myelinated axons when the water is restricted to diffusion along the long axis of the axons. However, due to pathological injury processes such as gliosis, demyelination, and necrosis, the structural integrity of the axons is compromised, and water is no longer restricted to diffusing along the long axis. These macro and microstructural changes attenuate the anisotropic signature in dMRI signals (Chiang et al., 2014). Consequently, it remains challenging to accurately characterize the change in tissue microstructure and the connectivity within lesioned white matter areas which are crucial for studying disconnection syndromes.

Clinical researchers typically measure changes in tissue microstructure by comparing the measurements in the lesion ROI with measurements in healthy tissue from the left-right flipped ROI (Song et al., 2015). Using microstructure measurements from the contralesional side as a model for the original properties is not the most accurate approach because the brain is not symmetric and where it is symmetric, e.g. CST, the tissue measurements are not identical and are less similar to restored tissue measurements. With regards to mapping lesion connectivity, one strategy clinical researchers use is to project the patient's lesion into

a normal database of streamlines to approximate the degree of disruption by the lesion to normative (Greene et al., 2019). However, this strategy produces a generic estimate of the patient's lost connectivity, without any characterization of patient specific disrupted connectivity. Other researchers simply track through the lesioned area to map the lesion's connectivity (Langen et al., 2018). However, tracking through lesioned areas is known to affect streamline reconstruction and structural networks (Theaud et al., 2017; Greene et al., 2018).

Another strategy for characterizing lesion connectivity and changes in microstructure is to restore or inpaint the lesioned fiber diffusion model. This has the advantage of more closely preserving the patient's native connectivity structure. Prior work has primarily focused on inpainting multiple sclerosis (MS) and tumor lesions in T1 & T2 weighted images to improve registration accuracy to a template (Sdika et al., 2009; Prados et al., 2016). Recently, a method has been developed to restore fiber orientation distributions (FODs) in MS lesions (Sun et al., 2017). They combine diffusion based inpainting and FOD reconstruction in a single step. But they only assessed their performance on an unrealistic simulated lesion of 9 voxels, so it is unclear how it would perform in-vivo. Moreover, it's only capable of restoring FODs.

Although a method exists for restoring FODs, a solution that can restore multiple fiber diffusion models, is needed for multiple reasons. The ability to restore diffusion tensors would be beneficial since diffusion tensor imaging (DTI) remains the most popular technique used by clinical researchers for characterizing changes in tissue microstructure and connectivity in lesioned WM tissue. Furthermore, many clinical diffusion datasets in wide use can be reconstructed in myriad ways and contain lesions from the myriad

etiologies of WM injury such as white matter hyperintensities in the Rotterdam Study and the Human Connectome Project (HCP) Lifespan study (Hofman et al., 2015; Glasser et al., 2013). Since there is a great need in clinical research to improve prediction outcomes, the ability of researchers to restore the fiber diffusion models of their choice in a lesion would make such an approach more accessible and have the potential to improve these predictions through improved anatomical delineation of lesion disrupted connectivity and measurement of changes in tissue microstructure.

In this paper, we describe a novel approach that combines methods from diffusion-based image inpainting and estimation theory for restoring fiber diffusion models in WM lesions. Our approach begins by taking healthy WM fiber models at the boundary of the lesion and filling in lesioned voxels with their optimal affine estimate moving iteratively in a fast-marching method style until the fiber models in the lesion are restored. By leveraging estimation theory, we can minimize the mean squared error (MSE) of fiber models within the lesion, restoring their original shapes and orientations. We demonstrate with realistic in-vivo simulations on diffusion tensors and fiber orientation distributions that our approach offers superior performance over multiple inpainting approaches. Further we restore diffusion tensors and FODs in lesions in three stroke patients suffering hemiparesis and demonstrate that the shape and orientation of the fiber models and the ability to map the lesion’s connectivity are recovered.

4.2 Methods

4.2.1 Diffusing imaging data

The S500 dataset containing 500 subjects was collected from the Washington University-Minnesota Consortium Human Connectome Project (Glasser et al., 2013). Further analysis was restricted to 210 subjects without familial relation. The diffusion volumes were collected with a spatial resolution 1.25×1.25×1.25 mm, using three shells at b = 1000, 2000, and 3000 s/mm^2 with 90 diffusion directions/shell and 6 additional b0s/shell.

Diffusion volumes were collected for three stroke patients with unilateral motor impairment at Emory University using the HCP Lifespan protocol with a spatial resolution of 1.5×1.5×1.5 mm, using two shells at b = 1500 and 3000 s/mm^2 with 46 diffusion directions per shell and 7 b0s. All datasets were corrected for geometric, eddy current, and motion distortions using the HCP Pipeline scripts.

The diffusion tensors were reconstructed from the diffusion weighted volumes collected with b = 1000 s/mm^2 with weighted least squares in Dipy for the HCP dataset and b = 1500 s/mm^2 for the stroke dataset (Garyfallidis et al., 2014). Fiber orientation distributions we reconstructed using constrained spherical deconvolution (CSD) in MRtrix with b = 3000 s/mm^2 and l_{max} = 8 for both datasets (Tournier et al., 2007; Tournier et al., 2012). The response function was estimated using the recursive Tax algorithm (Tax et al., 2014).

4.2.2. Model estimation

Suppose there is a lesioned diffusion fiber model $\boldsymbol{L}$ lying at the boundary of the lesion and healthy WM tissue. If the model is a diffusion tensor then there are only 6 unique elements of $\boldsymbol{L}$ that need to be estimated i.e. $D_{xx}, D_{yy}, D_{zz}, D_{xy}, D_{xz}, and\ D_{yz}$ because diffusion tensors are positive semi-definite matrices. Similarly, if a more complex spherical deconvolution model is used then at each lesioned voxel the FOD is represented by a real-valued spherical harmonic coefficient vector, F, containing $(l_{max} + 1) \times (l_{max} + 2)/2$ elements that need to be estimated. Consider that $\boldsymbol{L}$ has N observed healthy or restored neighboring models, $H_1, H_2, \ldots, H_N$. Each unknown element, Y_i *e.g.* D_{xx} *or* F_i, is treated as a random variable. The collection of matching neighbor elements forms a random vector $X = [X_1, X_2, \cdots, X_N]$. Then each unknown element Y_i can be estimated from the known neighboring elements of H_i using an optimal affine estimator.

We seek an affine estimator $\hat{Y} = a_0 + \sum_{i=1}^{N} a_i X_i$ such that the MSE e.g. $\varepsilon^2 = E[(Y - \hat{Y})^2]$ is minimized. To minimize this expression, we differentiate it with respect to a_i. Differentiating $E[(Y - a_0 + \sum_{i=1}^{N} a_i X_i)^2]$ with respect to a_0 and setting it to 0 we find that $a_0 = \mu_Y - \sum_{i=1}^{N} a_i \mu_{X_i}$ which it then follows that $\hat{Y} = \mu_Y + \sum_{i=1}^{N} a_i (X - \mu_{X_i})$. Letting $\tilde{Y} = Y - \mu_Y\ and\ \tilde{X} = X - \mu_X$ we can rewrite our MSE criterion as $E[(\tilde{Y} - \sum_{i=1}^{N} a_i \tilde{X}_i)^2]$.

By differentiating this with respect to the coefficients and setting the result to 0 produces: $E[(\tilde{Y} - \sum_{i=1}^{N} a_i \tilde{X}_i)\tilde{X}_j] = 0 \quad j = 1,2,\cdots,N$ which can be rewritten as $E[\tilde{X}_j \tilde{Y}] = \sum_{i=1}^{N} E\left[a_i \tilde{\tilde{X}}_i \tilde{X}_j\right]$. These sets of equations can be expressed in matrix form as $R_{XY} = (R_{XX})a$ where R_{XY} is the cross-correlation and R_{XX} is the auto-correlation matrices

and a are the coefficients. We obtain the optimal coefficients: $a = (R_{XX})^{-1}R_{XY}$. From this solution it is possible to produce the optimal affine estimate of elements of $\boldsymbol{L}$

$$L_i = a_1 L_i^{\widetilde{\boldsymbol{H_1}}} + a_2 L_i^{\widetilde{\boldsymbol{H_2}}} + \cdots + a_N L_i^{\widetilde{\boldsymbol{H_N}}} + \mu_{Y_i}, \text{ where } \widetilde{H_i} = H_i - \mu_{X_i} \quad (1)$$

By taking the affine combination of the neighboring healthy elements. Since *Y* and *X* are approximately Gaussian, the optimal affine estimate excellently approximates the optimal MMSE estimate of *Y*. However, to construct an optimal affine estimator at each voxel a distribution of diffusion fiber models must exist at every voxel in the patient

4.2.3. Distribution of fiber models

To compute the expectations in the optimal affine estimator, it is necessary to have a distribution of fiber models at each voxel for estimating the coefficients that minimize the MSE. A fiber model distribution for every voxel in the patient can be constructed through spatial normalization. Custom diffusion fiber model templates are constructed using DTI-TK and FOD Reorientation & ANTs (Raffelt et al., 2012; Zhang et al., 2007; Avants et al., 2008).

After the templates are constructed, we spatially normalize the patients reconstructed tensors or FODs into its respective custom HCP template. We then combine the estimated deformation fields to the template for the patients and the HCP subjects to warp a subset of tensor or FOD data from the HCP subjects that corresponds to voxels in the patients' lesion and healthy voxels at the boundary.

4.2.4. Model inpainting

We use a diffusion based inpainting algorithm where the lesion region is filled from its border to the center inspired from (Telea, 2004). At each iteration, rather than taking a simple average of the known neighboring tensors, we estimate the unknown model $\boldsymbol{L}$ by taking the affine combination of its healthy neighbors where the coefficients are estimated from the optimal affine estimator in Eq. (1). Note that an optimal affine estimator is estimated for each element of the diffusion model for each voxel in the lesion region.

while the lesion region is not empty:

for all $\boldsymbol{L} \in \partial\Omega$:

for all $y \in \boldsymbol{L}(\boldsymbol{y})$:

$$y = a_1 L_i^{\widetilde{\boldsymbol{H_1}}} + a_2 L_i^{\widetilde{\boldsymbol{H_2}}} + \cdots + a_N L_i^{\widetilde{\boldsymbol{H_N}}} + \mu_{Y_y}$$

$\Omega = \Omega / \partial\Omega$

where $\widetilde{H_i} = H_i - \mu_{X_y}$ & $y \in [L_1, L_2, \cdots, L_N]$, $\boldsymbol{L}$ is the model to inpaint, Ω is the lesion region, $\overline{\Omega}$ its complement (the voxels outside Ω), $\partial\Omega$ its border (voxels of Ω having one of its 6 cube neighbors in $\overline{\Omega}$).

4.3 Results

4.3.1 Simulation in-vivo

We demonstrate the efficacy of our approach by simulating a lesion within a healthy HCP subject that is not part of the model distribution. The lesion was created by adding Rician noise to a cuboidal region consisting of 1035 voxels (129 cm^3) until the SNR = 3. The lesioned voxels are then inpainted with a baseline approach and our optimal approach. For our baseline, we use the same diffusion based inpainting algorithm as used in the optimal estimation where the inpainted model is estimated by simply taking an average of its neighbors (Telea, 2004). The results of inpainting the tensors (top) and FODs (bottom) with both approaches is shown in Figure 1 within the transparent border.

Figure 1C shows the ground truth reconstructions. The baseline approach is shown in Figure 1B and our optimal approach is show in Figure 1D. At first glance, the baseline approach appears to provide a reasonable restoration of the tensors but upon closer inspection many tensors have different anisotropy and orientation (color) relative to the ground truth tensors. For FODs restored using the baseline approach it is immediately clear that they differ in both magnitude and orientation with respect to the ground truth. Our optimal approach more accurately preserves the anisotropy and orientation of the ground truth tensors and the magnitude and orientation of the ground truth FODs.

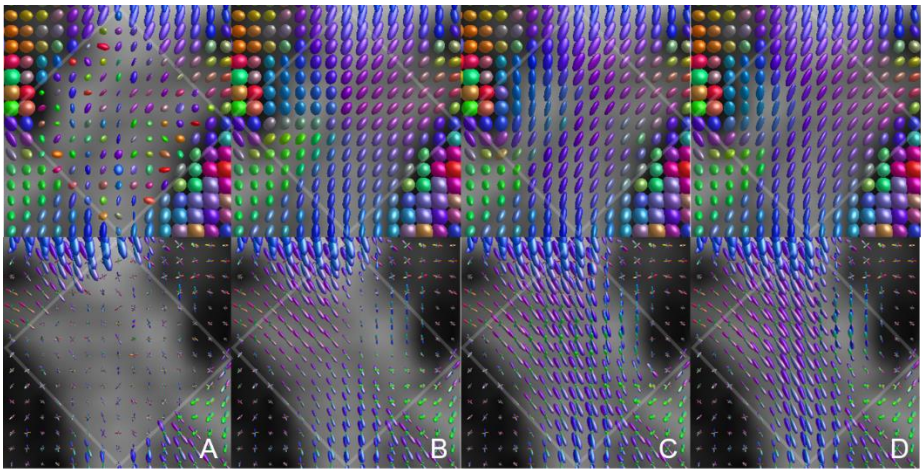

Figure 1: In-vivo simulated fiber model restoration: The lesion region is demarcated by the transparent border. Rician noise is added to the original diffusion signal until SNR = 3 producing the tensors (top) and FODs (bottom) in A. The baseline approach in B appears to provide reasonable approximation of normal tensors but upon closer inspection the restored tensors differ in anisotropy and orientation, while for FODs there are large deviations in magnitude and orientation from the ground truth The ground truth reconstructions are in C. Tensors and FODs restored using our optimal approach are in D. Notice that the tensors and FODs restored using our approach more closely match the ground truth in terms of orientation and shape compared to the baseline.

The mean angular error (MAE) is plotted for the primary fiber direction for FODs (solid) and tensors (dotted) from the HCP template mean normalized into the lesion area (green), restored using the baseline approach (orange), and restored using our optimal approach (blue) with respect to the primary fiber direction from the respective ground truth FOD and tensors for lesion sizes varying from 6 voxels to 1035 voxels on the left in Figure 2. For the smallest lesions, the difference in MAE is negligible for all the approaches and the FODs MAE is less than the tensors MAE. However, as lesion size increases the FOD MAE quickly outpaces the tensor MAE. In general, the template average has the largest MAE while our optimal approach as the smallest as lesion size increase. The MAE for the baseline approach grows more rapidly than our optimal approach for both tensors and FODs and for large lesions the MAE is twice as large. On the right in Figure 2, the average RMSE of elements making up a tensor and FOD are plotted. The template average has the largest average per element RMSE and is mostly constant with increasing lesion size. The baseline approach

again grows more rapidly than our optimal approach. The tensor data has a smaller average per element RMSE compared to FODs for all approaches. Our optimal approach achieves the best performance in terms of error across all lesion sizes.

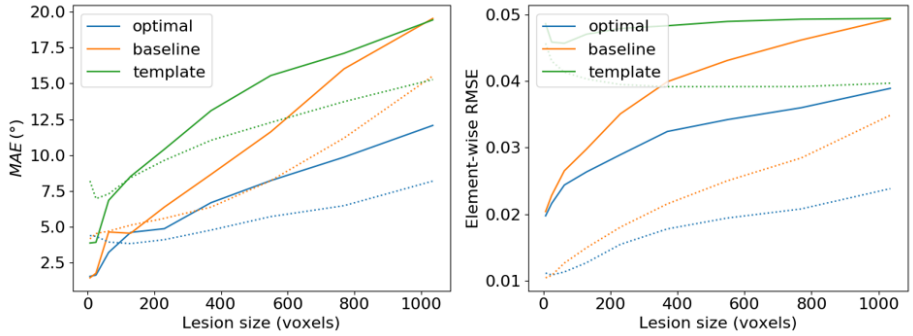

Figure 2: Quantification of error: On the left, the MAE is plotted for varying lesions sizes. The MAE for the smallest lesion sizes is comparable across all approaches and the FODs MAE (solid) is smaller than the tensors MAE (dotted). However, the FODs MAE quickly outpaces the tensor MAE at larger lesion sizes. The template average (green) has the largest MAE while our optimal approach (blue) as the smallest as lesion size increase. The MAE for the baseline approach (orange) grows more rapidly than our optimal approach for both tensors and FODs. Typically, the baseline approach as a MAE twice as large as of our optimal approach. On the right, the average RMSE of elements making up a tensor and FOD are plotted. The template average has the largest average per element RMSE for both fiber models. The baseline approach average per element RMSE grows more rapidly than our optimal approach. The average per element RMSE for tensor data is smaller than for FOD data. Our optimal approach achieves the smallest MAE and RMSE.

On the top left of Figure 3, the root mean squared error (RMSE) in fractional anisotropy (FA) with respect to the ground truth is measured for varying lesion sizes. The RMSE starts high and then slowly decreases until it's constant with increasing lesion size for the template mean. The RMSE of FA values extracted from the flipped ROI in the contralesional area (red) with respect to the original FA values also starts high and then grows slowly with increasing lesion size. For lesion sizes < 200 voxels, the baseline and optimal approach have almost identical trends, but for larger sizes the baseline approach grows much faster than for our optimal approach. At large lesion sizes the baseline approach again has an error almost double our optimal approach. For axial diffusivity (AD) on the top right, the template mean and optimal AD RMSE's both grow moderately with increasing lesion size while the RMSE for the baseline and flipped case grow faster. On the bottom row in Figure 3, the RMSEs for

mean diffusivity (MD) and radial diffusivity (RD) are plotted. The MD and RD RMSE for the flipped case grows the fastest with increasing lesion size while the template mean, the baseline, and optimal approach's RMSE grow slowly. Interestingly, there is not much gain in terms of RMSE for MD and RD between the baseline and our optimal approach. In general, our optimal approach has the smallest RMSE and grows the slowest with increase lesion size while the baseline outperforms the template mean which outperforms the flipped-case for all tissue measures.

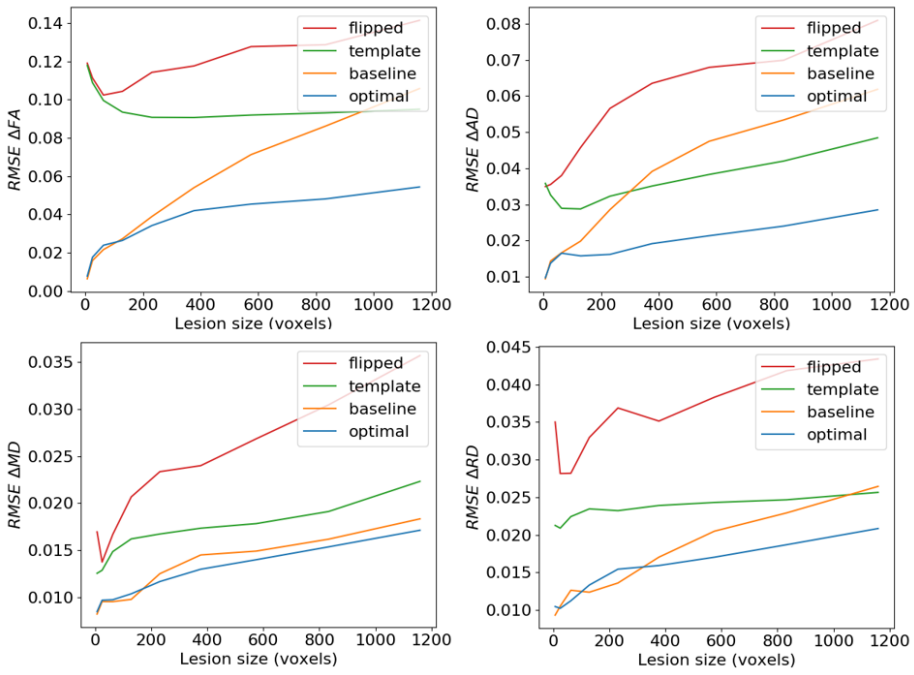

Figure 3: RMSE of tissue microstructure measurements: On the top left, RMSE FA for the baseline (orange) and our optimal approach (blue) show nearly identical trends for lesion sizes < 200 voxels. The baseline RMSE FA increases more rapidly compared to our optimal approach and is nearly twice as large at larger lesion sizes. For the template mean (green) the RMSE gradually decreases until becoming constant as the lesion size increases. The RMSE of FA values extracted from the flipped ROI in the contralesional area (red) with respect to the original FA values grows slowly with increasing lesion size. On the top right the RMSE for axial diffusivity (AD) is plotted. The template mean and optimal AD RMSE's both grow moderately with increasing lesion size while the RMSE for the baseline and flipped case grow faster. On the bottom row, the RMSEs for mean diffusivity (MD) and radial diffusivity (RD) are plotted. The MD and RD RMSE for the flipped case grows the fastest with increasing lesion size while the template mean, the baseline, and optimal approach's RMSE grow slowly. For MD and RD there is not much gain with our optimal approach over the baseline. In general, our optimal approach has the smallest RMSE and grows the slowest with increasing lesion size for all tissue measures.

4.3.2 Lesion restoration

The restoration results using our optimal approach are plotted in Figure 4 for three patients. The lesion region for each patient that undergoes restoration is demarcated in red on the coronal FA slice in column A. The lesioned tensors before and after the restoration are seen in columns B and C in Figure 4. In column B, the tensors in the lesion area have lost their normal color (orientation) and shape (anisotropy). Notice that the restored tensors in column C have both normal appearing shape and color. The lesioned FODs before and after restoration are plotted in columns D and E. In column D, the lesioned FODs have lost their normal orientation and magnitude. The orientation and magnitude of FODs in the lesion are recovered after undergoing restoration using our optimal approach. Moreover, the restored tensors and FODs demonstrate high spatial coherence with the surrounding healthy white matter tensors and FODs.

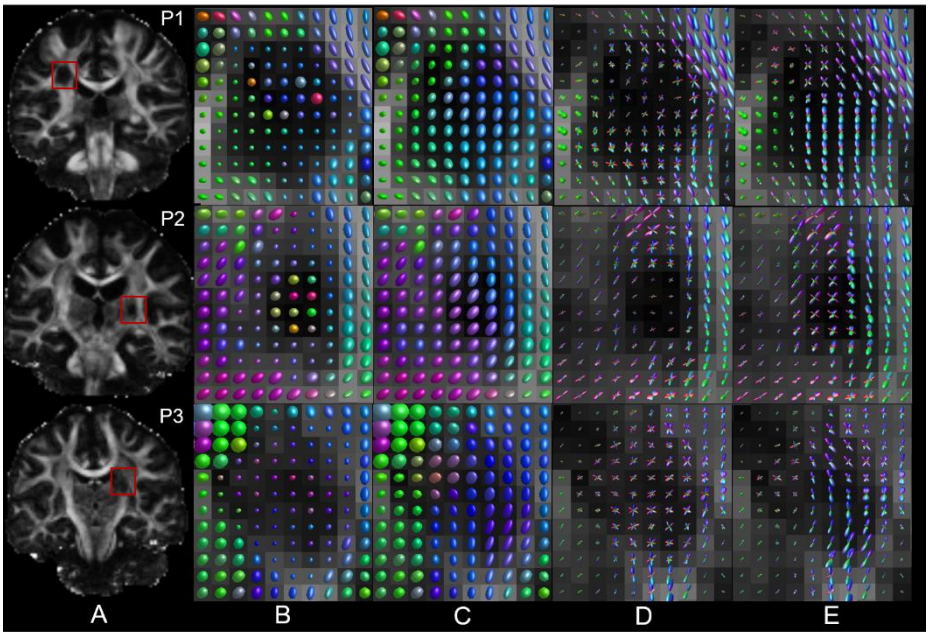

Figure 4: Restoration results for three stroke patients: The lesion regions where tensors undergo restoration is demarcated in red in column A. In column B are the tensors before the restoration and afterwards in column C. The loss of anisotropy (shape) and proper orientation (color) of healthy white matter tissue in the CST are

visible in column B. In column C, our approach restores the orientations and anisotropy of the tensors to a normal appearance. Similarly, the FODs in the lesion area of column D have lost their normal orientation and magnitude. After undergoing restoration using our optimal approach the normal orientation and magnitude of the FODs in the lesion area has been recovered in E. The restored tensors (C) and FODs (E) demonstrate high spatial coherence with their surroundings.

The restoration of scalar tissue microstructure measures AD, MD, and RD are plotted in Figure 5 for patient 1 on the same coronal plane. In the top row are the measures before the restoration and in the bottom row after the restoration. The lesion area is demarcated in red. Notice that after restoration using our optimal approach that the lesion area has been restored to a normal appearance for all the scalar diffusivities.

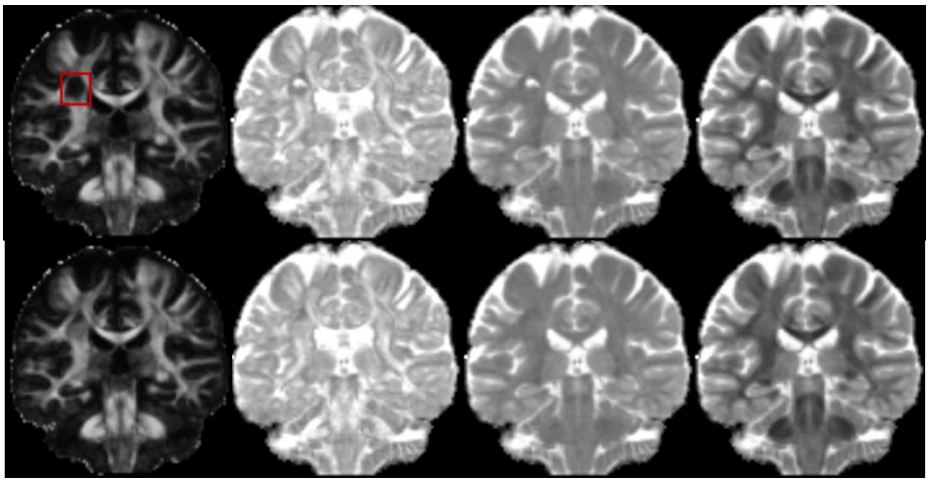

Figure 5: Tissue microstructure measures before (top) and after (bottom) restoration for patient 1: From left to right axial diffusivity, mean diffusivity, and radial diffusivity. The lesion area is demarcated in red. The lesion area has been restored to a normal appearance for all measures.

To demonstrate the improved mapping of lesion connectivity after fiber model restoration, we perform deterministic tractography before and after restoration on FODs in MRtrix with default settings using the SD_STREAM algorithm from a seed image consisting of two voxels below the lesion area with 1000 seeds per voxel [14]. In Figure 6, the tractography results before the restoration (top) and after the restoration (middle) are displayed on top of their respective sagittal FA slice (bottom). In all three patients, once the tracking enters the lesion area it prematurely terminates before the restoration, preventing an accurate mapping of connectivity within the lesion. After the FODs have been restored,

tracking through the lesion area becomes feasible enabling a more accurate mapping of the lesion's connectivity.

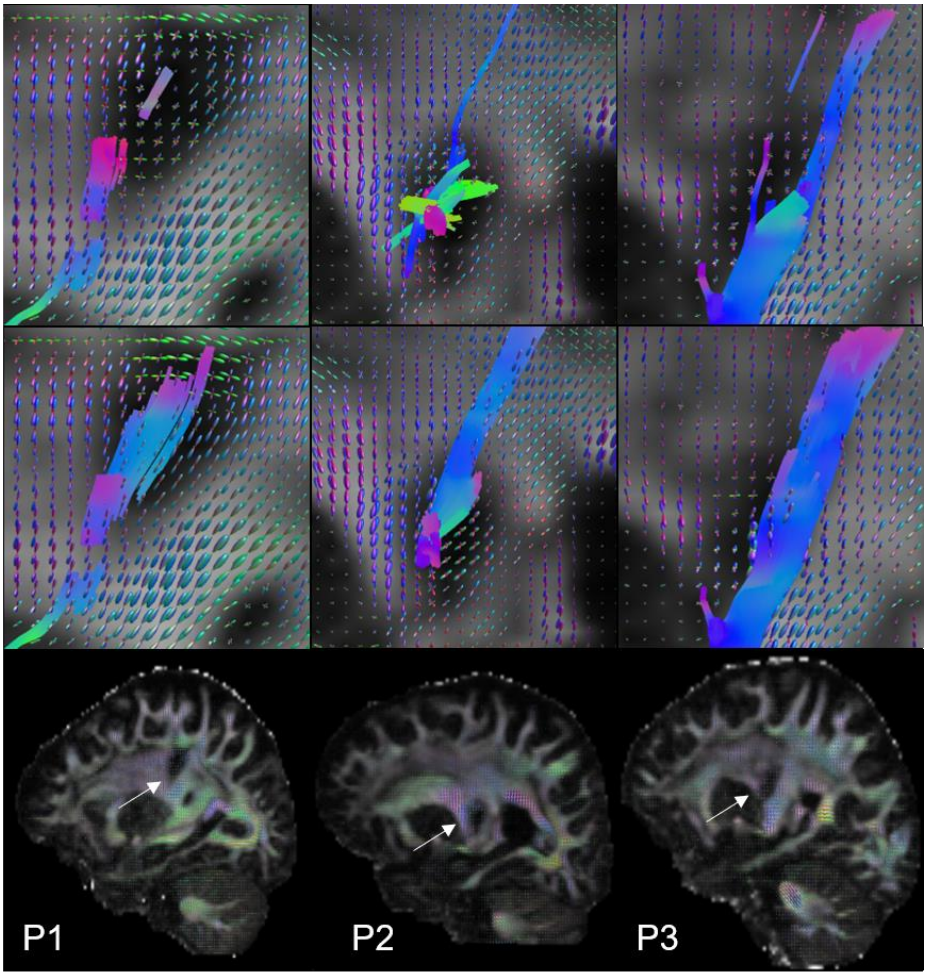

Figure 6: Deterministic tractography results before (top) and after (middle) restoration: Before the restoration, all three patients streamlines prematurely terminate once they enter the lesion area, making it difficult to study the patients' lesion connectivity. After the restoration, tractography can be performed more accurately because the FODs have been restored, enhancing the tracking and mapping of connectivity in the lesion areas. The results are plotted on top of their respective sagittal FA slice (bottom).

4.4 Discussion

Using in-vivo simulations and stroke patient data, we demonstrated the ability of our novel approach for accurately restoring both the orientation and magnitude of FODs and

the orientation, anisotropy, and tissue microstructure measures of diffusion tensors in WM lesions. Our optimal affine estimator approach offers superior performance over a diffusion based inpainting approach that takes the average of neighboring tensors for inpainting a lesioned area as well as the trivial copy and pasting of tensors or FODs from the normalized HCP tensor or FOD template.

Simple neighbor averaging performs well for very small lesions. However, as the lesion sizes increases, it introduces increased blurring that compounds moving inward. The increased blurring is reflected by the large increases in angular error and error in scalar measures such as FA or AD as the lesion sizes increase. Our optimal approach performs well at restoring tensors and FODs across all lesion sizes with only modest increases in angular error and error in scalar measures as the lesion size increases because as the algorithm moves inward, the fiber diffusion models are inpainted with their optimal affine combination of their neighbors such that the MSE is minimized. Consequently, blurring is reduced as the algorithm moves toward the center of the lesion.

Although performance was only measured on simulated cuboidal lesions, our method is applicable to lesions of any shape. Besides lesion size and location, the quality of the restoration depends on the initial healthy fiber diffusion models that are optimally combined to inpaint the first set of models in the lesion area. If the healthy models are corrupted by noise or by proximity to the lesion, it will get propagated into all subsequent inpainted models. Consequently, we recommend overestimating the lesion mask and carefully defining the white matter mask to ensure all models used in the initial stages are in fact healthy. Moreover, despite only demonstrating the restoration of

lesioned diffusion tensors and FODs, orientation distribution functions (ODFs) from QBI could also be restored using our approach by representing them with an orthonormal spherical harmonic basis and using FOD reorientation to build a distribution of ODFs.

Clinicians and researchers could find our approach beneficial for restoring fiber diffusion models in lesioned areas in their clinical diffusion datasets because it not only improves the accuracy of measuring changes in tissue microstructure relative to measurements from the contralesional area but also improves the accuracy of tractography results and the mapping of connectivity from the lesion for improved study of structure-function relationships and outcome prediction. To apply our approach, visit https://github.com/clintg6/OFDMR.

Appendix

A.1 Subsampling validation

We present Diffusion-In Figure 1, Connectivity loss matrices estimated from shortest paths found for the full set of combinations of interface voxel pairs are plotted in the left column for two patients. On the right connectivity loss matrices estimated from shortest paths found for only a subsampled set of combinations of interface voxel pairs are plotted. The matrices in the left and right columns are virtually indistinguishable for both patients.

The Spearman correlation coefficient for both patients between the full and subsample connectivity loss matrices is 0.99.

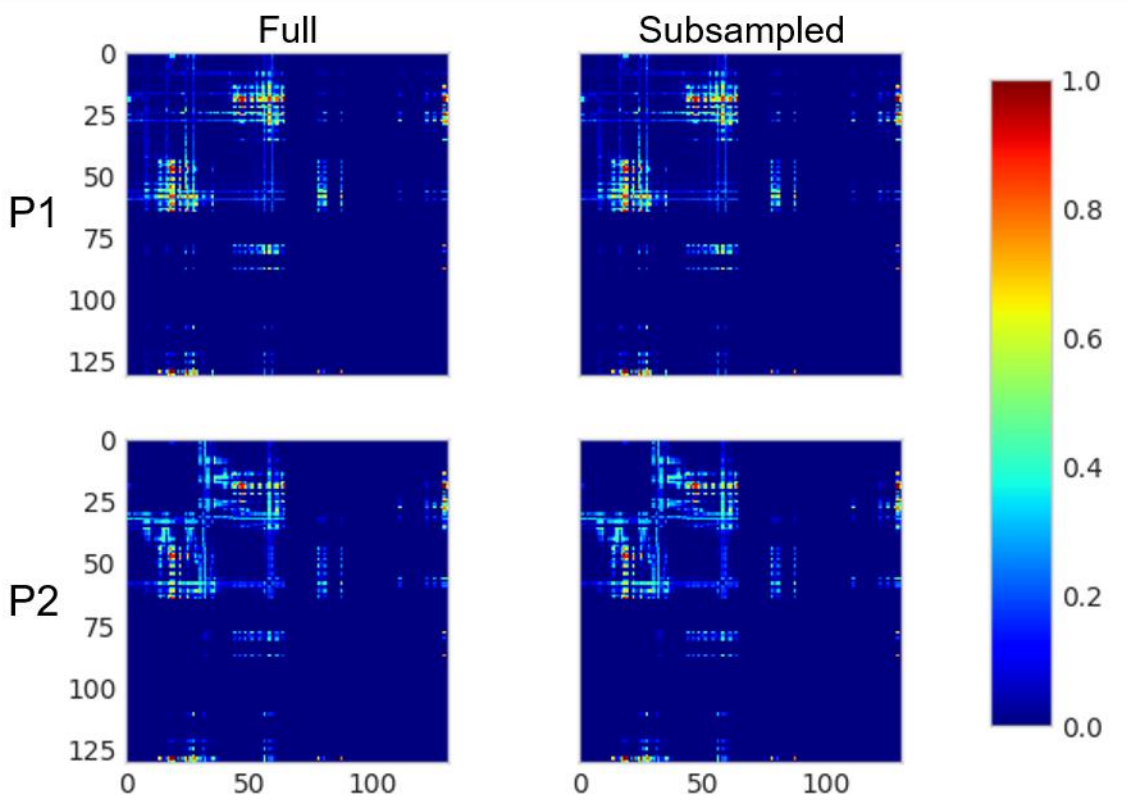

Figure 1: On the left connectivity loss matrices estimated from shortest paths found for the full set of combinations of interface voxel pairs for two patients. On the right are connectivity loss matrices estimated from shortest paths found for only a subsampled set of interface voxel pairs. The matrices in the left and right columns are virtually indistinguishable from each other in the same patient. The Spearman correlation between the full and subsampled connectivity loss matrices for both patients is 0.99.

In Figure 2, the profiles for the change in the weight of the k-heaviest subgraph at each iteration of k are plotted for both patients from full and subsampled constructed connectivity matrices. The full and subsampled profiles in each patient have a concave structure and are again virtually indistinguishable. In both patients, the full and subsampled profiles have a Spearman correlation coefficient of 0.99. Both sets of profiles for both patients peak at the same $k_{optimal}$.

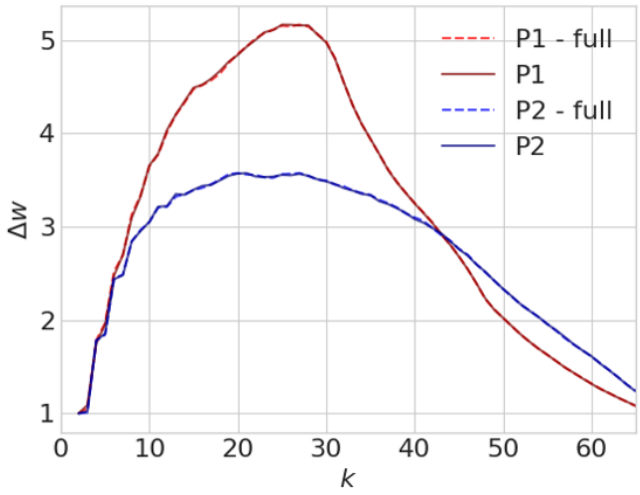

Figure 2: Change in the weight of the k-heaviest subgraph at each iteration of k profiles are plotted for both patients from full and subsampled constructed connectivity matrices. The full and subsampled profiles in each patient have a concave structure and are again virtually indistinguishable from each other. In both patients, the full and subsampled profiles have a Spearman correlation coefficient of 0.99 and peak at the same $k_{optimal}$.

A.2 Greedy algorithm validation

To measure the performance of our greedy algorithm compared to the exact solution, the weight of the subgraph is plotted for each iteration of k up to k = 15 for the greedy and exact solutions from connectivity loss matrices from three patients' stroke lesions in Figure 3 on the left. The solutions agree excellently with a Spearman R-score of 0.99. Patient 3 (red) weights do not reach as large of a weight at k = 15 compared to Patient 4 (green) and Patient 5 (blue). Patient 3's lesion is only 132 voxels compared to the large lesions of Patient 4's at 8498 voxels and Patient 5's at 5624 voxels. The agreement between the solutions is also seen in the middle plot for the change in the weight of the subgraph for each node k added to the subgraph. Again Patient 4's and Patient 5's change in weight curves grow larger for each node added due to larger lesion size compared to Patient 3's. On the right in Figure 3, the dice overlap between the nodes making up the exact heaviest subgraph of k nodes and the greedy heaviest subgraph. At k = 15, Patient's 3 & 4 both have a dice overlap of 1.0 i.e.

perfect agreement between the exact solution and greedy solution. For Patient 5, the dice overlap is 0.87. As k increases, the dice overlap grows. This suggests that there is minor disagreement initially about which node to add but converges as k increases.

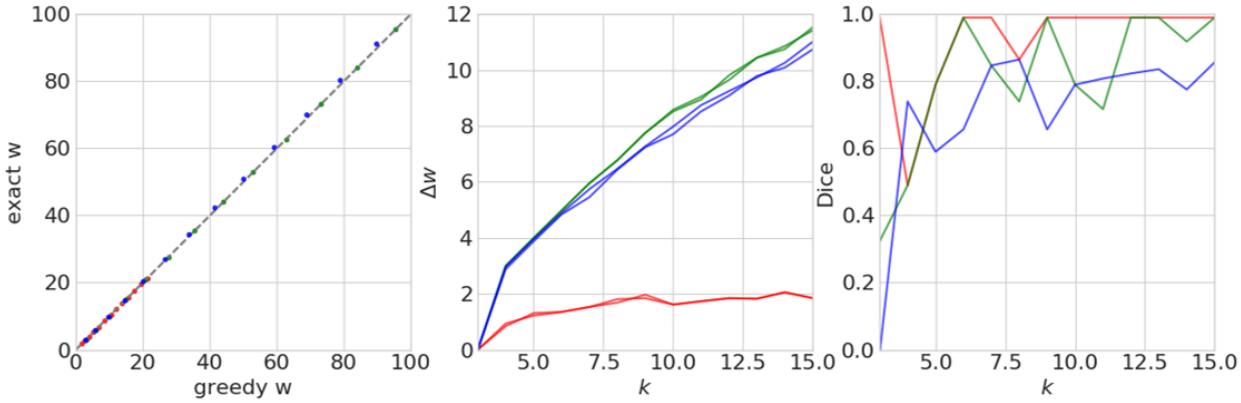

Figure 3: On the left the weight of the subgraph for each iteration of k up to k = 15 is plotted for the greedy solution and the exact solution for three stroke patients. Patient 3 (red) weights do not reach as large of a weight at k = 15 compared to Patient 4 (green) and Patient 5 (blue). Patient 3's lesion is only 132 voxels compared to the large lesions of Patient 4's at 8498 voxels and Patient 5's at 5624 voxels. Unity dashes line is in gray. The change in the total edge weight of the subgraph as it grows in the number of nodes k for our greedy approach and exact solution grows larger for larger lesions Patient's 4 & 5 compared to small lesions like with Patient 3. The dice overlap for the set of nodes from the exact subgraph and our greedy subgraph for each iteration of k is plotted on the right. Initially, the agreement is poor but as k increases the agreement is excellent. The dice overlap for Patient 3 and Patient 4 is 1.0 at k = 15 and 0.87 for Patient 5.

References

1. Dubois, J., Dehaene-Lambertz, G., Kulikova, S., Poupon, C., Hüppi, P. S., & Hertz-Pannier, L. (2014). The early development of brain white matter: a review of imaging studies in fetuses, newborns and infants. *neuroscience*, *276*, 48-71.

2. Passingham, R. E., Stephan, K. E., & Kötter, R. (2002). The anatomical basis of functional localization in the cortex. *Nature Reviews Neuroscience*, *3*(8), 606.

3. Sporns, O., Tononi, G., & Kötter, R. (2005). The human connectome: a structural description of the human brain. *PLoS computational biology*, *1*(4), e42.

4. Fornito, A., & Bullmore, E. T. (2015). Connectomics: a new paradigm for understanding brain disease. *European Neuropsychopharmacology*, *25*(5), 733-748.

5. Behrens, T. E., & Sporns, O. (2012). Human connectomics. *Current opinion in neurobiology*, *22*(1), 144-153.

6. Sotiropoulos, S. N., & Zalesky, A. (2019). Building connectomes using diffusion MRI: why, how and but. *NMR in Biomedicine*, *32*(4), e3752.

7. Lancaster, J. L., Woldorff, M. G., Parsons, L. M., Liotti, M., Freitas, C. S., Rainey, L., ... & Fox, P. T. (2000). Automated Talairach atlas labels for functional brain mapping. *Human brain mapping*, *10*(3), 120-131.

8. Daducci, A., Gerhard, S., Griffa, A., Lemkaddem, A., Cammoun, L., Gigandet, X., ... & Thiran, J. P. (2012). The connectome mapper: an open-source processing pipeline to map connectomes.

9. Thomas Yeo, B. T., Krienen, F. M., Sepulcre, J., Sabuncu, M. R., Lashkari, D., Hollinshead, M., ... & Fischl, B. (2011). The organization of the human cerebral cortex estimated by intrinsic functional connectivity. *Journal of neurophysiology*, *106*(3), 1125-1165.

10. Smith, S. M., Miller, K. L., Salimi-Khorshidi, G., Webster, M., Beckmann, C. F., Nichols, T. E., ... & Woolrich, M. W. (2011). Network modelling methods for FMRI. *Neuroimage*, *54*(2), 875-891.

11. Honey, C. J., Kötter, R., Breakspear, M., & Sporns, O. (2007). Network structure of cerebral cortex shapes functional connectivity on multiple time scales. *Proceedings of the National Academy of Sciences*, *104*(24), 10240-10245.

12. Honey, C. J., Sporns, O., Cammoun, L., Gigandet, X., Thiran, J. P., Meuli, R., & Hagmann, P. (2009). Predicting human resting-state functional connectivity from

structural connectivity. *Proceedings of the National Academy of Sciences*, *106*(6), 2035-2040.

13. Alexander, A. L., Lee, J. E., Lazar, M., & Field, A. S. (2007). Diffusion tensor imaging of the brain. *Neurotherapeutics*, *4*(3), 316-329.

14. Tournier, J. D., Calamante, F., & Connelly, A. (2007). Robust determination of the fibre orientation distribution in diffusion MRI: non-negativity constrained super-resolved spherical deconvolution. *Neuroimage*, *35*(4), 1459-1472.

15. Yeh, F. C., Verstynen, T. D., Wang, Y., Fernández-Miranda, J. C., & Tseng, W. Y. I. (2013). Deterministic diffusion fiber tracking improved by quantitative anisotropy. *PloS one*, *8*(11), e80713.

16. Jones, D. K. (2010). Challenges and limitations of quantifying brain connectivity in vivo with diffusion MRI. *Imaging in Medicine*, *2*(3), 341-355.

17. Descoteaux, M., Deriche, R., Knosche, T. R., & Anwander, A. (2008). Deterministic and probabilistic tractography based on complex fibre orientation distributions. *IEEE transactions on medical imaging*, *28*(2), 269-286.

18. Thomas, C., Frank, Q. Y., Irfanoglu, M. O., Modi, P., Saleem, K. S., Leopold, D. A., & Pierpaoli, C. (2014). Anatomical accuracy of brain connections derived from diffusion MRI tractography is inherently limited. *Proceedings of the National Academy of Sciences*, *111*(46), 16574-16579.

19. Buchanan, C. R., Pernet, C. R., Gorgolewski, K. J., Storkey, A. J., & Bastin, M. E. (2014). Test–retest reliability of structural brain networks from diffusion MRI. *Neuroimage*, *86*, 231-243.

20. Maier-Hein KH, Neher PF, Houde JC, Cote MA, Garyfallidis E, Zhong J, Chamberland M, Yeh FC, Lin YC, Ji Q, Reddick WE, Glass JO, Chen DQ, Feng Y, Gao C, Wu Y, Ma J, Renjie H, Li Q, Westin CF, Deslauriers-Gauthier S, Gonzalez JOO, Paquette M, St-Jean S, Girard G, Rheault F, Sidhu J, Tax CMW, Guo F, Mesri HY, David S, Froeling M, Heemskerk AM, Leemans A, Bore A, Pinsard B, Bedetti C, Desrosiers M, Brambati S, Doyon J, Sarica A, Vasta R, Cerasa A, Quattrone A, Yeatman J, Khan AR, Hodges W, Alexander S, Romascano D, Barakovic M, Auria A, Esteban O, Lemkaddem A, Thiran JP, Cetingul HE, Odry BL, Mailhe B, Nadar MS, Pizzagalli F, Prasad G, Villalon-Reina JE, Galvis J, Thompson PM, Requejo FS, Laguna PL, Lacerda LM, Barrett R, Dell'Acqua F, Catani M, Petit L, Caruyer E, Daducci A, Dyrby TB, Holland-Letz T, Hilgetag CC, Stieltjes B, Descoteaux M. 2017. The challenge of mapping the human connectome based on diffusion tractography. Nat Commun. 8: 1349.

21. Schober, M., Kasenburg, N., Feragen, A., Hennig, P., & Hauberg, S. (2014, September). Probabilistic shortest path tractography in DTI using Gaussian Process ODE solvers. In *International Conference on Medical Image Computing and Computer-Assisted Intervention* (pp. 265-272). Springer, Cham.

22. Girard, G., Whittingstall, K., Deriche, R., & Descoteaux, M. (2014). Towards quantitative connectivity analysis: reducing tractography biases. *Neuroimage*, *98*, 266-278.

23. Scoville, W. B., & Milner, B. (1957). Loss of recent memory after bilateral hippocampal lesions. *Journal of neurology, neurosurgery, and psychiatry*, *20*(1), 11.

24. Fox, M. D. (2018). Mapping symptoms to brain networks with the human connectome. *New England Journal of Medicine*, *379*(23), 2237-2245.

25. Damasio, H., Grabowski, T., Frank, R., Galaburda, A. M., & Damasio, A. R. (1994). The return of Phineas Gage: clues about the brain from the skull of a famous patient. *Science*, *264*(5162), 1102-1105.

26. Lim, C., & Alexander, M. P. (2009). Stroke and episodic memory disorders. *Neuropsychologia*, *47*(14), 3045-3058.

27. Baldassarre A, Ramsey L, Rengachary J, Zinn K, Siegel JS, Metcalf NV, Strube MJ, Snyder AZ, Corbetta M, Shulman GL. 2016. Dissociated functional connectivity profiles for motor and attention deficits in acute right-hemisphere stroke. Brain. 139: 2024-38.

28. Geschwind N, Kaplan F. 1962. A human cerebral disconnection syndrome. Neurology. 12: 675-85.

29. Warren, D. E., Power, J. D., Bruss, J., Denburg, N. L., Waldron, E. J., Sun, H., ... & Tranel, D. (2014). Network measures predict neuropsychological outcome after brain injury. *Proceedings of the National Academy of Sciences*, *111*(39), 14247-14252.

30. Logothetis, N. K., & Wandell, B. A. (2004). Interpreting the BOLD signal. *Annu. Rev. Physiol.*, *66*, 735-769.

31. Logothetis, N. K., Pauls, J., Augath, M., Trinath, T., & Oeltermann, A. (2001). Neurophysiological investigation of the basis of the fMRI signal. *Nature*, *412*(6843), 150.

32. Stam, C. J., Van Straaten, E. C. W., Van Dellen, E., Tewarie, P., Gong, G., Hillebrand, A., ... & Van Mieghem, P. (2016). The relation between structural and functional connectivity patterns in complex brain networks. International Journal of Psychophysiology, 103, 149-160.

33. Cieslak, M., & Grafton, S. T. (2014). Local termination pattern analysis: A tool for comparing white matter morphology. Brain imaging and behavior, 8(2), 292-299.

34. Van Essen, D. C., Smith, S. M., Barch, D. M., Behrens, T. E., Yacoub, E., Ugurbil, K., & WU-Minn HCP Consortium. (2013). The WU-Minn human connectome project: an overview. Neuroimage, 80, 62-79.

35. Glasser, M. F., Sotiropoulos, S. N., Wilson, J. A., Coalson, T. S., Fischl, B., Andersson, J. L., ... & WU-Minn HCP Consortium. (2013). The minimal preprocessing pipelines for the Human Connectome Project. Neuroimage, 80, 105-124.

36. Caruyer, E., Lenglet, C., Sapiro, G., & Deriche, R. (2013). Design of multishell sampling schemes with uniform coverage in diffusion MRI. Magnetic Resonance in Medicine, 69(6), 1534-1540.

37. Yeh, F. C., Wedeen, V. J., & Tseng, W. Y. I. (2010). Generalized-sampling imaging. Medical Imaging, IEEE Transactions on, 29(9), 1626-1635.

38. Yeh, F. C., & Tseng, W. Y. I. (2011). NTU-90: a high angular resolution brain atlas constructed by q-space diffeomorphic reconstruction. *Neuroimage*, *58*(1), 91-99.

39. Fischl, B., & Dale, A. M. (2000). Measuring the thickness of the human cerebral cortex from magnetic resonance images. Proceedings of the National Academy of Sciences, 97(20), 11050-11055.

40. Hagmann, P., Cammoun, L., Gigandet, X., Meuli, R., Honey, C. J., Wedeen, V. J., & Sporns, O. (2008). Mapping the structural core of human cerebral cortex. PLoS Biol, 6(7), e159.

41. Avants, B. B., Yushkevich, P., Pluta, J., Minkoff, D., Korczykowski, M., Detre, J., & Gee, J. C. (2010). The optimal template effect in hippocampus studies of diseased populations. Neuroimage, 49(3), 2457-2466.

42. Avants, B. B., Tustison, N. J., Song, G., Cook, P. A., Klein, A., & Gee, J. C. (2011). A reproducible evaluation of ANTs similarity metric performance in brain image registration. Neuroimage, 54(3), 2033-2044.

43. Christiaens, D., Dhollander, T., Maes, F., Sunaert, S., & Suetens, P. (2012). The Effect of Reorientation of the Fibre Orientation Distribution on Fibre Tracking. Proceedings CDMRI 2012, 33-44.

44. Klein, A., Andersson, J., Ardekani, B. A., Ashburner, J., Avants, B., Chiang, M. C., ... & Song, J. H. (2009). Evaluation of 14 nonlinear deformation algorithms applied to human brain MRI registration. *Neuroimage*, *46*(3), 786-802.

45. Alexander, D. C., Pierpaoli, C., Basser, P. J., & Gee, J. C. (2001). Spatial transformations of diffusion tensor magnetic resonance images. *Medical Imaging, IEEE Transactions on*, *20*(11), 1131-1139.

46. Stejskal, E. O., & Tanner, J. E. (1965). Spin diffusion measurements: spin echoes in the presence of a time-dependent field gradient. *The journal of chemical physics*, *42*(1), 288-292.

47. Tuch, D. S. (2004). Q-ball imaging. *Magnetic Resonance in Medicine*, *52*(6), 1358-1372.

48. Raffelt, D., Tournier, J., Crozier, S., Connelly, A., & Salvado, O. (2012). Reorientation of fiber orientation distributions using apodized point spread functions. *Magnetic Resonance in Medicine*, *67*(3), 844-855.

49. Jeurissen, B., Leemans, A., Tournier, J. D., Jones, D. K., & Sijbers, J. (2013). Investigating the prevalence of complex fiber configurations in white matter tissue with diffusion magnetic resonance imaging. *Human brain mapping*, *34*(11), 2747-2766.

50. Jeurissen, B., Tournier, J. D., Dhollander, T., Connelly, A., & Sijbers, J. (2014). Multi-tissue constrained spherical deconvolution for improved analysis of multi-shell diffusion MRI data. *Neuroimage*, *103*, 411-426.

51. Tournier, J., Calamante, F., & Connelly, A. (2012). MRtrix: diffusion tractography in crossing fiber regions. *International Journal of Imaging Systems and Technology*, *22*(1), 53-66.

52. Bassett, D. S., Brown, J. A., Deshpande, V., Carlson, J. M., & Grafton, S. T. (2011). Conserved and variable architecture of human white matter connectivity. *Neuroimage*, *54*(2), 1262-1279.

53. Tournier, J. D., Calamante, F., Gadian, D. G., & Connelly, A. (2004). Direct estimation of the fiber orientation density function from diffusion-weighted MRI data using spherical deconvolution. *NeuroImage*, *23*(3), 1176-1185.

54. Hong, X., Arlinghaus, L. R., & Anderson, A. W. (2009). Spatial normalization of the fiber orientation distribution based on high angular resolution diffusion imaging data. *Magnetic resonance in medicine*, *61*(6), 1520-1527.

55. Côté, M. A., Girard, G., Boré, A., Garyfallidis, E., Houde, J. C., & Descoteaux, M. (2013). Tractometer: Towards validation of tractography pipelines. *Medical image analysis*, *17*(7), 844-857.

56. Rubinov, M., Kötter, R., Hagmann, P., & Sporns, O. (2009). Brain connectivity toolbox: a collection of complex network measurements and brain connectivity datasets. *NeuroImage*, *47*, S169.

57. Sepkoski Jr, J. J. (1974). Quantified coefficients of association and measurement of similarity. *Journal of the International Association for Mathematical Geology*, *6*(2), 135-152.

58. Charikar, M. S. (2002, May). Similarity estimation techniques from rounding algorithms. In *Proceedings of the thiry-fourth annual ACM symposium on Theory of computing* (pp. 380-388). ACM.

59. Girard, G., Whittingstall, K., Deriche, R., & Descoteaux, M. (2014). Towards quantitative connectivity analysis: reducing tractography biases. *Neuroimage*, *98*, 266-278.

60. Jones, D. K., Knösche, T. R., & Turner, R. (2013). White matter integrity, fiber count, and other fallacies: the do's and don'ts of diffusion MRI. *Neuroimage*, *73*, 239-254.

61. Zhang, H., Yushkevich, P. A., Alexander, D. C., & Gee, J. C. (2006). Deformable registration of diffusion tensor MR images with explicit orientation optimization. *Medical image analysis*, *10*(5), 764-785.

62. Gazzaniga, M. S. (1989). Organization of the human brain. *Science*, *245*(4921), 947-952.

63. Hua, K., Zhang, J., Wakana, S., Jiang, H., Li, X., Reich, D. S., ... & Mori, S. (2008). Tract probability maps in stereotaxic spaces: analyses of white matter anatomy and tract-specific quantification. *Neuroimage*, *39*(1), 336-347.

64. Thottakara, P., Lazar, M., Johnson, S. C., & Alexander, A. L. (2006). Application of Brodmann's area templates for ROI selection in white matter tractography studies. *Neuroimage*, *29*(3), 868-878.

65. Jarbo, K., & Verstynen, T. D. (2015). Converging structural and functional connectivity of orbitofrontal, dorsolateral prefrontal, and posterior parietal cortex in the human striatum. *The Journal of neuroscience*, *35*(9), 3865-3878.

66. Gu, S., Pasqualetti, F., Cieslak, M., Telesford, Q. K., Alfred, B. Y., Kahn, A. E., ... & Bassett, D. S. (2015). Controllability of structural brain networks. *Nature communications*, *6*.

67. Cieslak, M., Ingham, R. J., Ingham, J. C., & Grafton, S. T. (2015). Anomalous white matter morphology in adults who stutter. *Journal of Speech, Language, and Hearing Research*, *58*(2), 268-277.

68. Muraskin, J., Dodhia, S., Lieberman, G., Garcia, J. O., Verstynen, T., Vettel, J. M., ... & Sajda, P. (2016). Brain dynamics of post-task resting state are influenced by expertise: Insights from baseball players. *Human Brain Mapping*.

69. Donos, C., Mălîia, M. D., Mîndruţă, I., Popa, I., Ene, M., Bălănescu, B., ... & Barborica, A. (2016). A connectomics approach combining structural and effective connectivity assessed by intracranial electrical stimulation.*NeuroImage, 132*, 344-358.

70. Molesworth, T., Sheu, L. K., Cohen, S., Gianaros, P. J., & Verstynen, T. D. (2015). Social network diversity and white matter microstructural integrity in humans. *Social cognitive and affective neuroscience*, nsv001.

71. Adluru, N., Destiche, D. J., Tromp, D. P., Davidson, R. J., Zhang, H., & Alexander, A. L. (2016). Evaluating consistency of deterministic streamline tractography in non-linearly warped DTI data. *arXiv preprint arXiv:1602.02117*.

72. Glasser, M. F., Coalson, T. S., Robinson, E. C., Hacker, C. D., Harwell, J., Yacoub, E., . . . Van Essen, D. C. (2016). A multi-modal parcellation of human cerebral cortex. *Nature, 536*(7615), 171-178.

73. Jenabi, M., Peck, K. K., Young, R. J., Brennan, N., & Holodny, A. I. (2014). Probabilistic fiber tracking of the language and motor white matter pathways of the supplementary motor area (SMA) in patients with brain tumors. *Journal of Neuroradiology. Journal de Neuroradiologie, 41*(5), 342-349. doi:10.1016/j.neurad.2013.12.001

74. Golby, A. J., Kindlmann, G., Norton, I., Yarmarkovich, A., Pieper, S., & Kikinis, R. (2011). Interactive diffusion tensor tractography visualization for neurosurgical planning. *Neurosurgery, 68*(2), 496-505. doi:10.1227/NEU.0b013e3182061ebb

75. Chang, S.-E., & Zhu, D. C. (2013). Neural network connectivity differences in children who stutter. *Brain, 136*(Pt 12), 3709-3726. doi:10.1093/brain/awt275

76. Van Essen, D. C., Ugurbil, K., Auerbach, E., Barch, D., Behrens, T. E. J., Bucholz, R., . . . Consortium,W.-M. H. (2012). The Human Connectome Project: a data acquisition perspective. *Neuroimage, 62*(4), 2222-2231. doi:10.1016/j.neuroimage.2012.02.018

77. Van Essen, D. C., Smith, J., Glasser, M. F., Elam, J., Donahue, C. J., Dierker, D. L., ... & Harwell, J. (2016). The Brain Analysis Library of Spatial maps and Atlases (BALSA) database. NeuroImage.

78. de Schotten, M. T., Urbanski, M., Batrancourt, B., Levy, R., Dubois, B., Cerliani, L., & Volle, E. (2016). Rostro-caudal architecture of the frontal lobes in humans. *Cerebral Cortex*.

79. Bourke, P. (1999). Interpolation methods. *Retrieved July, 20*, 2011.

80. Kim, J., Avants, B., Patel, S., Whyte, J., Coslett, B. H., Pluta, J., ... & Gee, J. C. (2008). Structural consequences of diffuse traumatic brain injury: a large deformation tensor-based morphometry study. *Neuroimage, 39*(3), 1014-1026.

81. Lazar, M. (2010). Mapping brain anatomical connectivity using white matter tractography. *NMR in Biomedicine*, *23*(7), 821-835.

82. Owen, J. P., Chang, Y. S., & Mukherjee, P. (2015). Edge density imaging: mapping the anatomic embedding of the structural connectome within the white matter of the human brain. *Neuroimage*, *109*, 402-417.

83. Colon-Perez, L. M., Spindler, C., Goicochea, S., Triplett, W., Parekh, M., Montie, E., ... & Mareci, T. H. (2015). Dimensionless, scale invariant, edge weight metric for the study of complex structural networks. *PLOS one*, *10*(7), e0131493.

84. Dhollander, T., Emsell, L., Van Hecke, W., Maes, F., Sunaert, S., & Suetens, P. (2014). Track orientation density imaging (TODI) and track orientation distribution (TOD) based tractography. *NeuroImage*, *94*, 312-336.

85. Damasio H, Damasio AR. 1989. *Lesion analysis in neuropsychology*. New York: Oxford Univ. Press.

86. Binkofski F, Seitz RJ, Hackländer T, Pawelec D, Mau J, Freund HJ. 2001. Recovery of motor functions following hemiparetic stroke: a clinical and magnetic resonance-morphometric study. Cerebrovasc Dis. 11: 273-81.

87. Wei K, Cieslak M, Greene C, Grafton ST, Carlson JM. 2018. Sensitivity analysis of human brain structural network construction. Netw Neurosci. 1: 446-67.

88. Carter, Alex R., Gordon L. Shulman, and Maurizio Corbetta. "Why use a connectivity-based approach to study stroke and recovery of function?." *Neuroimage* 62.4 (2012): 2271-2280.

89. Lim, Jae-Sung, and Dong-Wha Kang. "Stroke connectome and its implications for cognitive and behavioral sequela of stroke." *Journal of stroke* 17.3 (2015): 256.

90. Yourganov, Grigori, et al. "Multivariate connectome-based symptom mapping in post-stroke patients: Networks supporting language and speech." *Journal of Neuroscience* 36.25 (2016): 6668-6679.

91. Gleichgerrcht, Ezequiel, et al. "Connectome-based lesion-symptom mapping (CLSM): A novel approach to map neurological function." *NeuroImage: Clinical* 16 (2017): 461-467.

92. Zhu, L. L., Lindenberg, R., Alexander, M. P., & Schlaug, G. (2010). Lesion load of the corticospinal tract predicts motor impairment in chronic stroke. *Stroke*, *41*(5), 910-915.

93. Hope, Thomas MH, et al. "Distinguishing the effect of lesion load from tract disconnection in the arcuate and uncinate fasciculi." *Neuroimage* 125 (2016): 1169-1173.

94. Kuceyeski, Amy, et al. "The Network Modification (NeMo) Tool: elucidating the effect of white matter integrity changes on cortical and subcortical structural connectivity." *Brain connectivity* 3.5 (2013): 451-463.

95. de Schotten, M. T., Bizzi, A., Dell'Acqua, F., Allin, M., Walshe, M., Murray, R., ... & Catani, M. (2011). Atlasing location, asymmetry and inter-subject variability of white matter tracts in the human brain with MR diffusion tractography. *Neuroimage*, *54*(1), 49-59.

96. Langen, C. D., Cremers, L. G., de Groot, M., White, T., Ikram, M. A., Niessen, W. J., & Vernooij, M. W. (2018). Disconnection due to white matter hyperintensities is associated with lower cognitive scores. *NeuroImage*, *183*, 745-756.

97. Maillard, P., Fletcher, E., Harvey, D., Carmichael, O., Reed, B., Mungas, D., & DeCarli, C. (2011). White matter hyperintensity penumbra. *Stroke*, *42*(7), 1917-1922.

98. De Groot, M., Verhaaren, B. F., De Boer, R., Klein, S., Hofman, A., van der Lugt, A., ... & Vernooij, M. W. (2013). Changes in normal-appearing white matter precede development of white matter lesions. *Stroke*, *44*(4), 1037-1042.

99. Theaud, G., Dilharreguy, B., Catheline, G., & Descotaux, M. (2017). Impact of white-matter hyperintensities on tractography. In *25th Annual Meeting of the International Society for Magnetic Resonance in Medicine (ISMRM). Honolulu: International Society for Magnetic Resonance in Medicine*.

100. Greene, C., Cieslak, M., & Grafton, S. T. (2018). Effect of different spatial normalization approaches on tractography and structural brain networks. *Network Neuroscience*, *2*(3), 362-380.

101. Li, Longchuan, et al. "The effects of connection reconstruction method on the interregional connectivity of brain networks via diffusion tractography." *Human brain mapping* 33.8 (2012): 1894-1913.

102. Sinke, Michel RT, et al. "Diffusion MRI-based cortical connectome reconstruction: dependency on tractography procedures and neuroanatomical characteristics." *Brain Structure and Function* (2018): 1-17.

103. Cieslak, M., Brennan, T., Meiring, W., Volz, L. J., Greene, C., Asturias, A., Grafton, S. T. (2017). Analytic tractography: A closed-form solution for estimating local white matter connectivity with diffusion MRI. *NeuroImage*.

104. Ravi, Sekharipuram S., Daniel J. Rosenkrantz, and Giri Kumar Tayi. "Heuristic and special case algorithms for dispersion problems." *Operations Research* 42.2 (1994): 299-310.

105. Letsios, M., Balalau, O. D., Danisch, M., Orsini, E., & Sozio, M. (2016, December). Finding heaviest k-subgraphs and events in social media. In *Data Mining Workshops (ICDMW), 2016 IEEE 16th International Conference on* (pp. 113-120). IEEE.

106. Brecheisen, R., Platel, B., ter Haar Romeny, B. M., & Vilanova, A. (2013). Illustrative uncertainty visualization of DTI fiber pathways. *The Visual Computer*, *29*(4), 297-309.

107. Dice, Lee R. "Measures of the amount of ecologic association between species." *Ecology* 26.3 (1945): 297-302.

108. Abraham, Alexandre, et al. "Machine learning for neuroimaging with scikit-learn." *Frontiers in neuroinformatics* 8 (2014): 14.

109. Joutsa, J., Shih, L. C., Horn, A., Reich, M. M., Wu, O., Rost, N. S., & Fox, M. D. (2018). Identifying therapeutic targets from spontaneous beneficial brain lesions. *Annals of neurology*, *84*(1), 153-157.

110. Smith, R. E., Tournier, J. D., Calamante, F., & Connelly, A. (2015). SIFT2: Enabling dense quantitative assessment of brain white matter connectivity using streamlines tractography. *Neuroimage*, *119*, 338-351.

111. Daducci, A., Dal Palù, A., Lemkaddem, A., & Thiran, J. P. (2015). COMMIT: convex optimization modeling for microstructure informed tractography. *IEEE transactions on medical imaging*, *34*(1), 246-257.

112. Pestilli, F., Yeatman, J. D., Rokem, A., Kay, K. N., & Wandell, B. A. (2014). Evaluation and statistical inference for human connectomes. *Nature methods*, *11*(10), 1058.

113. Rusconi E, Pinel P, Eger E, Lebihan D, Thirion B, Dehaene S, Kleinschmidt A. 2009. A disconnection account of Gerstmann syndrome: functional neuroanatomy evidence. Ann Neurol. 66: 654-62.

114. Chiang, C. W., Wang, Y., Sun, P., Lin, T. H., Trinkaus, K., Cross, A. H., & Song, S. K. (2014). Quantifying white matter tract diffusion parameters in the presence of increased extra-fiber cellularity and vasogenic edema. Neuroimage, 101, 310-319.

115. Greene, C. A., Cieslak, M., Volz, L., Hensel, L., Grefkes, C., Rose, K., Grafton, ST. (2019). Finding maximally disconnected subnetworks with shortest path tractography. Neuroimage Clinical, Under review.

116. Sdika, M., & Pelletier, D. (2009). Nonrigid registration of multiple sclerosis brain images using lesion inpainting for morphometry or lesion mapping. Human brain mapping, 30(4), 1060-1067.

117. Prados, F., Cardoso, M. J., Cawley, N., Kanber, B., Ciccarelli, O., Wheeler-Kingshott, C. A. G., & Ourselin, S. (2016, October). Fully Automated Patch-Based Image Restoration: Application to Pathology Inpainting. In International Workshop on Brainlesion: Glioma, Multiple Sclerosis, Stroke and Traumatic Brain Injuries (pp. 3-15). Springer, Cham.

118. Sun, W., Amezcua, L., & Shi, Y. (2017, September). FOD Restoration for Enhanced Mapping of White Matter Lesion Connectivity. In International Conference on Medical Image Computing and Computer-Assisted Intervention (pp. 584-592). Springer, Cham.

119. Hofman, A., Brusselle, G. G., Murad, S. D., van Duijn, C. M., Franco, O. H., Goedegebure, A., ... & Stricker, B. H. C. (2015). The Rotterdam Study: 2016 objectives and design update. European journal of epidemiology, 30(8), 661-708.

120. Garyfallidis, E., Brett, M., Amirbekian, B., Rokem, A., Van Der Walt, S., Descoteaux, M., & Nimmo-Smith, I. (2014). Dipy, a library for the analysis of diffusion MRI data. Frontiers in neuroinformatics, 8, 8.Gleichgerrcht, Ezequiel, et al. "Connectome-based lesion-symptom mapping (CLSM): A novel approach to map neurological function." NeuroImage: Clinical 16 (2017): 461-467.

121. Zhang, H., Yushkevich, P. A., Rueckert, D., & Gee, J. C. (2007, October). Unbiased white matter atlas construction using diffusion tensor images. In International Conference on Medical Image Computing and Computer-Assisted Intervention (pp. 211-218). Springer, Berlin, Heidelberg.

122. Telea, A. (2004). An image inpainting technique based on the fast marching method. Journal of graphics tools, 9(1), 23-34.

123. Tax, C. M., Jeurissen, B., Vos, S. B., Viergever, M. A., & Leemans, A. (2014). Recursive calibration of the fiber response function for spherical deconvolution of diffusion MRI data. *Neuroimage*, *86*, 67-80.